

UNIVERSITÀ DEGLI STUDI DI PADOVA

Dipartimento di Fisica e Astronomia “Galileo Galilei”

Corso di Laurea Magistrale in Fisica

Tesi di Laurea

Titolo

Relatore

Prof. Emilio Martines

Laureando

Davide Mancini

Correlatore

Dr. Gianluca De Masi

Anno Accademico 2018/2019

Contents

1	Introduction	5
1.1	Plasma medicine	5
1.2	Cold Atmospheric Plasma	6
1.2.1	Plasma generation: RF and DBD	7
2	Plasma source description and electric characterization	13
2.1	General source description	13
2.2	Electric scheme	14
2.3	Output characterization	15
2.3.1	Measurements without gas	16
2.3.2	Measurements with gas	17
2.3.3	Effective current	22
2.3.4	Plasma impedance	22
3	Shape and dynamics	25
3.1	Experimental setup	25
3.1.1	Source and optical setup	28
3.1.2	Source, power lines and electric signals	28
3.1.3	Trigger synchronization	29
3.1.4	Different setups	31
3.1.5	Frame analysis and calibration	31
3.2	Helium flow	32
3.2.1	Plasma bullet description	32
3.2.2	Voltage influence	37
3.2.3	Flow influence	37
3.2.4	Insulating target	39
3.2.5	Conductive target	42
3.3	Neon flow	48
3.3.1	Free bullet	48
3.3.2	Insulating target	50
3.3.3	Conductive target	50
3.4	Argon flow	54
3.4.1	Dynamic example	54
3.4.2	Absence of target	57
3.4.3	Influence of target	57
3.5	Hints on bullet propagation model	57
3.5.1	Ion waves or electron drift	61
3.5.2	Mobility and velocity	64
4	Spectral Analysis	67
4.1	Radiation emission	67
4.2	Line recognition	68
4.2.1	Emission measurements	68

4.3	Relative intensities	72
4.3.1	Pulse settings	72
4.3.2	Line of Sight	72
4.3.3	Gas composition	74
4.4	Estimation of plasma temperatures	74
4.4.1	Rotational temperature for OH and for N ₂	77
4.4.2	Vibrational temperature for N ₂	78
5	Temperature profile	81
5.1	Experimental setup	81
5.2	Temperature profile	82
5.3	Power estimation	83

Chapter 1

Introduction

Plasma medicine is an emerging field that is broadening its applications from uses on medical equipments (sterilization, decontamination) to uses on living tissues ([1]). One of the research groups working in Consorzio RFX laboratories, in Padova, developed a source for the production of Cold Atmospheric Plasma (CAP) to be used for medical treatment on biological tissues: Plasma Coagulation Controller (PCC) ([2]). The source is a DBD reactor, where a dielectric is used to produce plasma with low charge density. It is developed to specialize in non thermal blood coagulation, i.e. acceleration of blood clot formation thanks to plasma direct application.

CAPs are of particular interest in plasma medicine for two characteristics:

- **Cold plasma** : given non thermal equilibrium and ion low temperature, this plasma can be applied on surfaces without a dangerous increase in target temperature. In plasma medicine CAPs allow treatment on living tissues, where target temperature must stay below a safe value.
- **Reactive Species** : if we produce plasma at atmospheric pressure, we can easily mix the gas used for plasma discharge with air. The peculiarity of a plasma in air is the presence of reactive species, ions, produced by ionization and recombination of nitrogen, oxygen, water and other atoms or molecules. There are several biological processes where activation and reactions speed is thought to be related to concentration of Reactive Oxydant Species (ROS) and Reactive Nitrogen Species (RNS) ([3], [4]).

In this chapter there is the presentation of some results obtained with PCC and a general description of the production of CAP, describing the sources developed at Consorzio RFX.

1.1 Plasma medicine

The most studied therapeutic effects of plasma application are:

- sterilization and decontamination ([5], [6]);
- blood coagulation ([7]);
- wound disinfection and healing ([8]);
- cancer cell treatment ([9]).

How plasma interacts with living tissues and produces those effects is not fully understood. Reactive species, along with UV radiation and electromagnetic field, are considered fundamental participants of the mechanism.

Previous works studied PCC induced bactericidal effects and non thermal blood coagulation, in the following their results will be described briefly.

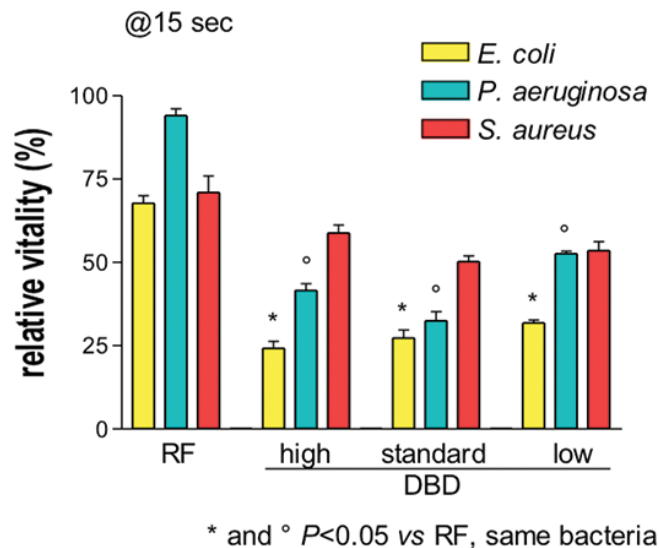


Figure 1.1: Relative vitality on different bacteria colonies after plasma treatment of 15 s with different sources. On the left there is treatment with an RF plasma source; on the right there is treatment with the DBD plasma source studied in this work, PCC, for three different combinations of parameters for the discharge (low, standard and high).

Bactericidal effects There are numerous studies on the effects of CAPs on bacteria ([10], [11]), however mechanisms leading to inactivation of bacteria are not known in their entirety. It is thought that plasma application has an effect when reactive species, UV photons and charged particles come into direct contact with cell's membrane and structures [1].

In figure 1.1 is presented the reduction of bacteria vitality due to application of plasma produced with our sources. From the figure it's possible to see results of the experiment on three different bacteria species, for an RF source and for the DBD source, PCC, with three different experimental setups. PCC seems to have more effect on the reduction of bacteria, for all analyzed species.

Blood coagulation Cauterization devices that produce quasi-thermal blood coagulation with high-temperature plasma have been used for a long time in wound treatment and surgery. Only recently studies shown that with cold plasma application is possible to induce natural blood coagulation, without temperature increase ([7], [12]). Treatments with CAPs activate the coagulation cascade shown in figure 1.2, a chain of reactions that involves many factors. The exact mechanisms that accelerates clot formation have yet to be understood, as of today studies show that plasma induces the production of fibrin that catalyses blood coagulation factors ([1]).

Treatment with PCC is done applying plasma on blood samples, as shown in figure 1.3 (a). The study involves the use of different plasma application times and different discharge parameters. The effect of plasma application is evaluated from samples as those in figure 1.3 (b), where the blood is removed and the area of the remaining coagulated blood is measured, leading to results in figure 1.3 (c). Results show always an increase on blood coagulation when treated with plasma.

1.2 Cold Atmospheric Plasma

Cold atmospheric plasma is plasma at atmospheric pressure where there is not thermodynamical equilibrium between electron and ions, electron temperature is higher than ion temperature ([13]). In those conditions plasma dynamics can be described as the collective motion of two interpenetrating fluids, where the thermal motion of ions can be ignored ([14]). There are several studies on CAP plasma characteristics ([15], [16], [17]) common values are electron temperatures between $T_e = 1 - 10 \text{ eV}$ and electron densities between $n_e = 10^{17} - 10^{22} \text{ m}^{-3}$, inside the box outlined in figure 1.4.

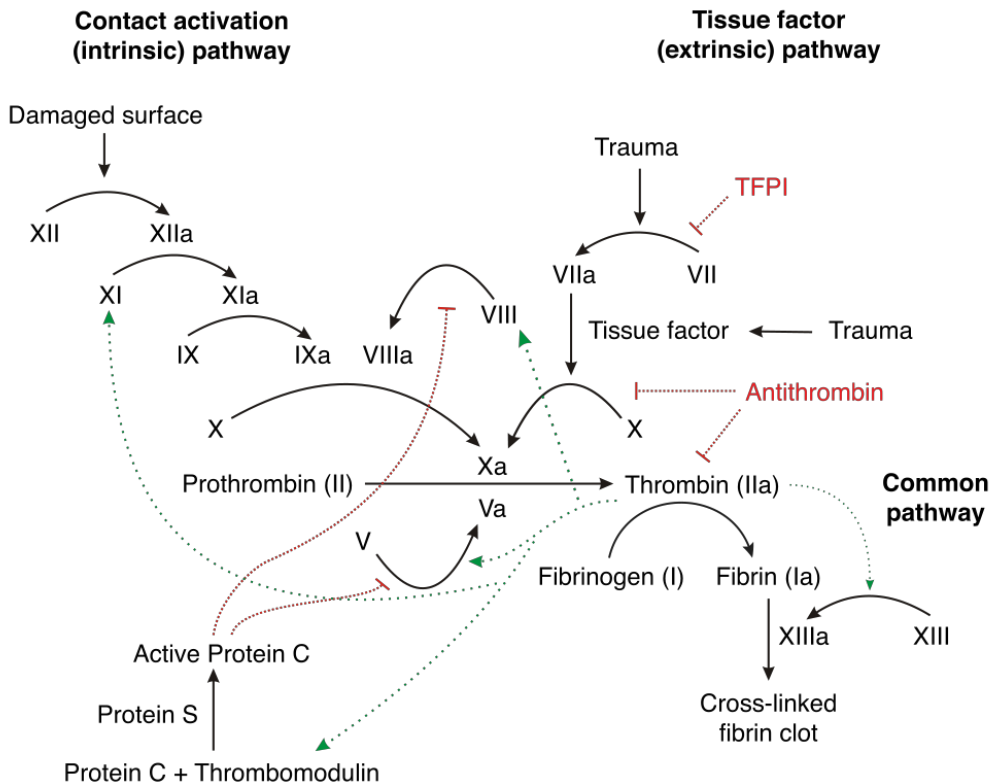


Figure 1.2: Reaction chain that leads to blood coagulation. The analysis of blood samples treated with plasma, allows to find where and how plasma intervenes in this scheme.

1.2.1 Plasma generation: RF and DBD

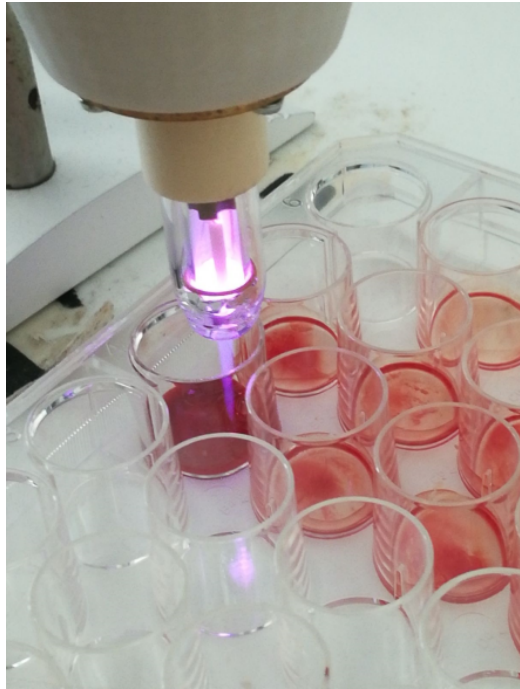
Electron density in CAPs is a small fraction of the neutral number density of an ideal gas $n_n = 2.50 \times 10^{25} \text{ m}^{-3}$ and higher than the number of electro-ion pairs naturally present in air at atmospheric pressure. Those pairs are generated by radioactive substances and cosmic rays, that have a total ionization rate of $10^7 \text{ m}^{-3}\text{s}^{-1}$ ([18]).

The application of a steady electric field to a gas accelerates free electrons that collide with atoms and molecules resulting in excitation or ionization reactions. If the electric field has enough intensity it extracts electrons from atoms and molecules ionizing them. Those reactions form ion-electron pairs that are accelerated producing other pairs, inducing chain reactions that could sustain plasma discharge. If and how this process starts is influenced by:

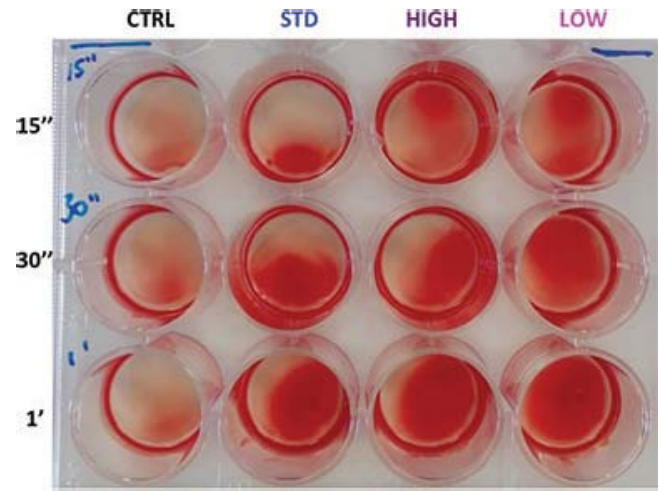
- gas species, on their ionization potential and cross section for different reactions
- characteristics length of the system, that influences charged particle's acceleration
- gas pressure, that is proportional to reaction rates

Generally electrons acquire more energy from the electric field due to the lower mass and higher mobility, so electronic temperature increases more rapidly than ion temperature. If we apply a steady DC electric fields, electrons and ions reach thermal equilibrium through collisions, generating thermal plasma at high temperatures. To avoid thermalization and produce cold plasma at high densities, it is possible to give energy only to electrons with AC electric fields at high frequency or with pulsed electric fields ([19]).

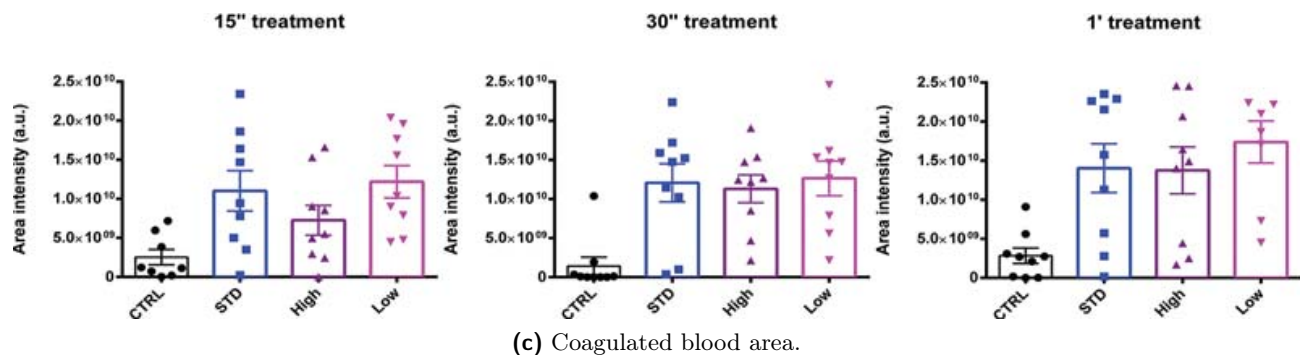
Two examples of sources that produce plasma for medical application are the ones built at RFX: the RF source based on a radio transmitter ([5]) and the DBD source, studied in this work ([2]).



(a) Picture of plasma application.



(b) Coagulated blood samples.



(c) Coagulated blood area.

Figure 1.3: Pictures and results of the blood coagulation study with PCC. Blood samples are treated with three different parameters of the DBD discharge, for three different application times. In (c) is possible to see the increase of coagulated blood area for samples treated by plasma, if compared to the control sample.

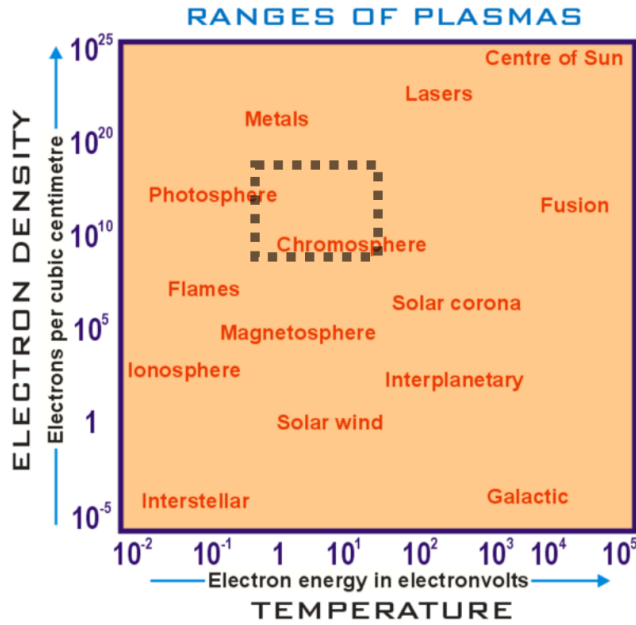


Figure 1.4: Plasma classification in function of electron density and electron temperature. Inside the square there are typical parameters for CAPs.

RF source The RF source developed in RFX works applying an AC electric field between two electrodes. It is composed by two coaxial tubes as shown in figure 1.5: the internal one is connected to a radio transmitter in series with a matching network and with an electrode formed by a wire grid; the external one ends with a second electrode fixed at ground potential. The radio transmitter works with fixed power (5 W) and is set to a specific frequency that is the resonance frequency for the LC series circuit formed by the inductance in the matching network and the parasitic capacitance of the device. When neutral gas flows inside the inner tube, the electric field between the electrodes ionizes it, producing cold plasma in air. The source is built with an inductance of $100 \mu\text{H}$, capacitance is estimated as 10 pF , resulting in a resonance for a frequency around 4.8 MHz, reaching voltage peak to peak values up to 900 V on the electrode. Regulation on the gas flow allows to start the discharge more easily and to reach lower peak voltage values. This source produces plasma directly in air, so it ionizes a mixture of neutral gas and air, giving birth to plasma rich in reactive species coming from oxygen and nitrogen molecules. The presence of reactive species allows to use this source for non-thermal sterilization of living tissues: plasma produced by it has bactericidal effects and does not damage human cells ([20]).

DBD source The source developed in this work is based on the Dielectric Barrier Discharge (DBD): it applies an electric field on the gas with one electrode or a pair of electrodes, where a dielectric covers at least one of them, as in figure 1.6. The dielectric works as an insulator and doesn't allow DC current to flow in the gap, so gas between the electrodes can be ionized without large current densities flowing through the resulting plasma ([21]). The discharge can be modeled as in the circuit in figure 1.6 (b) ([22]), C_1 is capacitance of dielectric, C_2 of air and R_p and C_p are plasma resistance and capacitance (in other studies we can find more refined models ([23])). Typical values for discharge parameters are AC voltage frequency or pulse rates $f \geq 1 \text{ kHz}$, voltage peak values from $V_p = 1 - 20 \text{ kV}$, and current peak intensities on a conductive target $I < 100 \text{ mA}$.

DBD plasma reactors changed in the last decades following the development of pulse power technology: from the classic sinusoidal voltage now is common to apply pulsed voltage. Plasma generated with sub-microseconds voltage pulses allows to avoid local discharges overheat and increases discharge production of reactive species inside the plasma ([24]). Those progresses in DBD plasma technology led to the development of sources for biomedical plasma applications. Those plasma sources, including PCC, have to produce plasma rich in reactive species, while meeting stringent requirements such as low

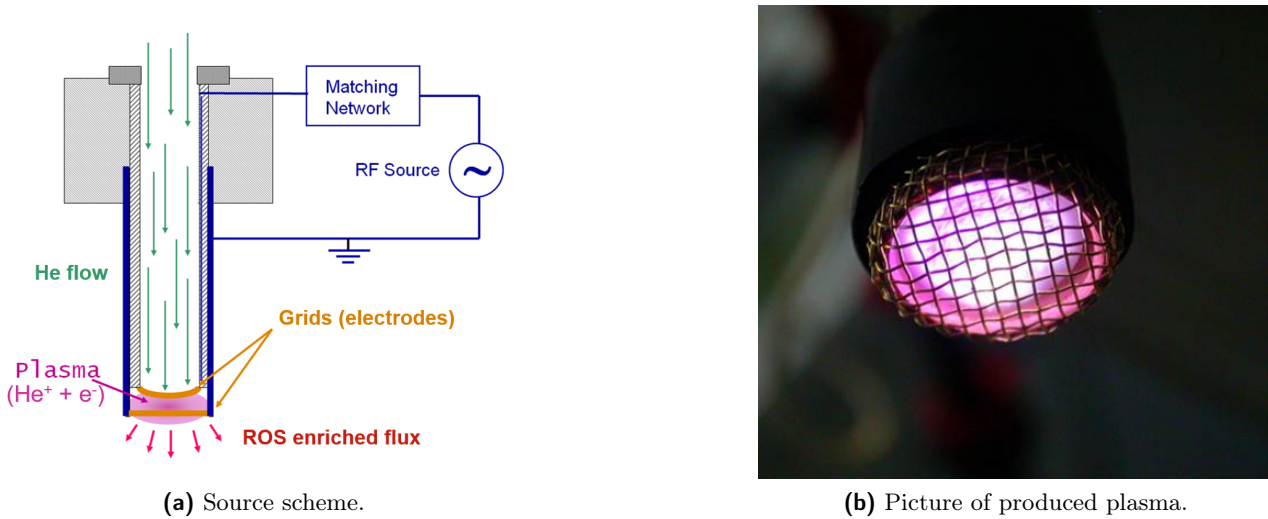


Figure 1.5: Plasma RF source developed in RFX.

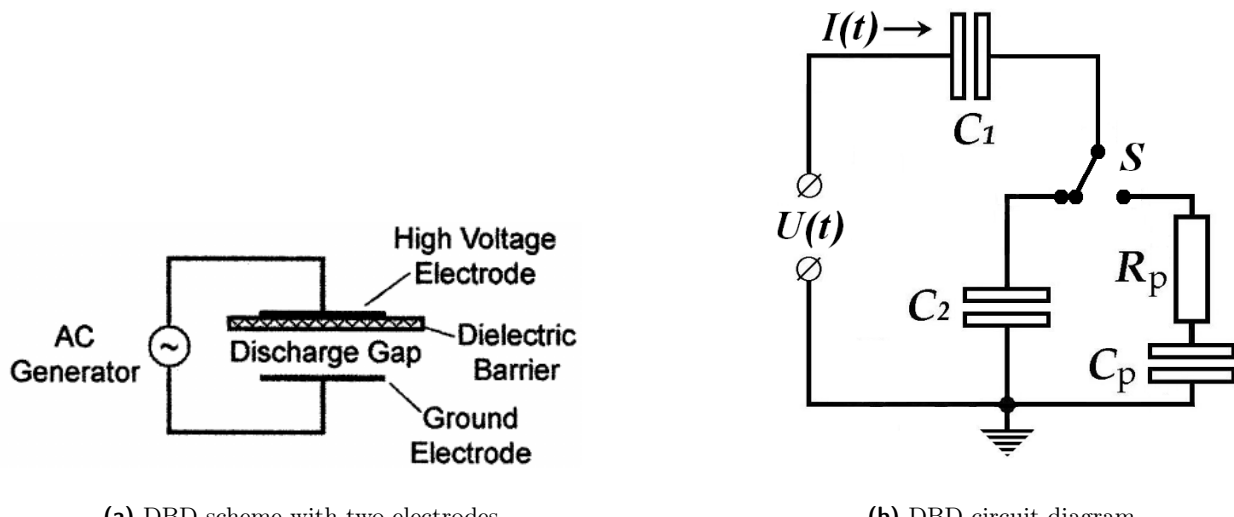


Figure 1.6: Representation of the concept behind DBD plasma production: on the left an experimental setup composed by two electrodes, one dielectric and a voltage AC generator; on the right a circuit diagram of the setup for DBD discharge. In the circuit, C_1 is the dielectric capacitance, C_2 the air capacitance, C_p and R_p are plasma capacitance and resistance.

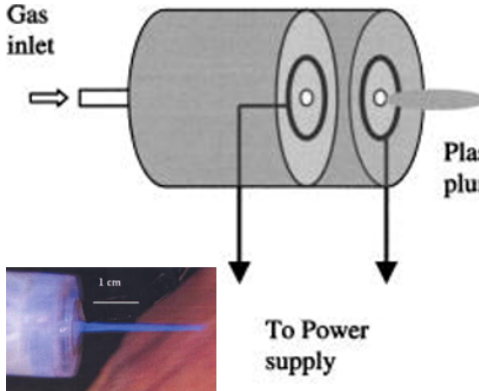
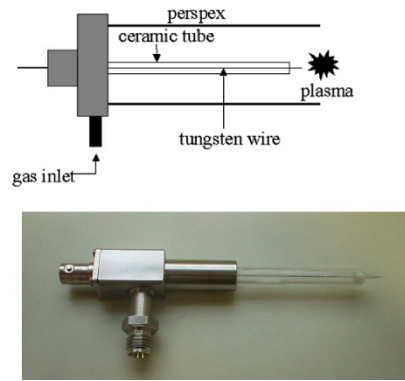
(a) *Plasma pencil* ([25]).(b) *Plasma needle* ([26]).

Figure 1.7: Two examples of DBD plasma sources for medical applications. In both sources we have one electrode that applies an electric field to neutral gas, ionizing it. Plasma is then expelled in air at atmospheric pressure.

temperature (at or near room temperature), no risk of arcing, operation at atmospheric pressure, preferably hand-held operation, low concentration of ozone generation, etc.

The design used in many works is in figure 1.7 ([25], [26]): a cylindrical electrode is covered in dielectric material and inserted in a tube with neutral gas flowing in it. The gas, typically helium or argon, allows to start plasma discharge, then plasma is expelled in air where it produces reactive species needed for medical treatment. PCC developed and studied in this thesis will be described in details in chapter 2, along with its electrical characterization.

An interesting phenomenon of sources with this design is plasma formation and propagation. High speed camera measurements of the process show that plasma is not produced in a uniform steady column, but every pulse of the electric field gives birth to localized plasma emission. Once produced, the collection of ionized particles moves away from the electrode and propagates in air, with velocities from 10 to over 150 km/s. Those localized plasma emissions are called “bullet” and only recently is possible to find models that describe them [27]. In this thesis this phenomenon is observed and studied in details in chapter 3, with different voltage pulse parameters, target position and gas composition.

As said before, the purpose of non thermal plasma application for medical uses is the deposition of reactive species on biological tissues. The presence and characteristics of reactive species can be studied by emission spectrometry, with intensity and temperature estimation. Chapter 4 is dedicated to the study of plasma radiation emission around visible wavelengths.

The other fundamental feature of plasma produced by our source is that it can be applied on human skin without danger. Temperature measurements on the target of plasma application can lead to an estimation of plasma power deposition. In chapter 5 are presented thermocamera measurements and power estimation.

Chapter 2

Plasma source description and electric characterization

Plasma Coagulation Controller (PCC) developed at RFX is a DBD cold plasma source that produces plasma at atmospheric pressure. The entire design is developed to guarantee the flexibility necessary to easy application on target. In this chapter we describe the source functioning scheme and characterize it.

2.1 General source description

PCC functions applying a fast high voltage pulse (from 2 to 10 kV) to a cylindrical electrode covered by pyrex glass that works as the dielectric used to produce plasma in DBD conditions ([2]). The electrode is positioned along the axis of a nozzle where we insert neutral gas, a pure noble gas sometimes mixed with other gasses, that allows to start the discharge. It is possible to put a second electrode formed by a conducting ring around the nozzle, that we can set to ground voltage or other voltage values, to modify the electric field if necessary.

When we start the voltage pulse, the electrode generates an electric field that ionizes the gas producing plasma with low free charge density thanks to the glass dielectric. Plasma forms a column of glowing gas, the plasma plume, that goes out from the nozzle exit and travels in the air outside, until it reaches a certain lenght or a target, as in figure 2.1. The plume is formed by cold plasma, it can be touched without a relevant increase of temperature on the skin or any other danger.

PCC development goes through different designs (an example of the first one in [28]), for this study we use two different prototypes for the head, **A** and **B**, with same concepts and little differences.

In both models we have the high voltage controller separated from the head where plasma is produced, the first one controls the trigger for the voltage pulse, the second one is where we produce plasma. The controller contains power cables and circuits and an Arduino Leonardo that controls pulse repetition rate and amplitude, as explained later. The head is a cylinder 30 cm long with diameter of 8 cm, where are mounted three coils with three *N87* ferrite cores of dimensions $32 \times 16 \times 9$ mm and inductance $2.3 \mu\text{H}$ ([29]). The spire ratio between primary and secondary circuit on the resulting coil is of 1/30. On one end of the head there is the driver circuit that receives an optical signal from the controller, that is the trigger signal for voltage pulse; on the other end there is the electrode. The driver circuit is connected with the primary circuit of the coil, the electrode to the secondary circuit. When the controller sends the trigger, there is a voltage variation on primary circuit that produces the voltage pulse on the electrode. Controller and head are connected only with power cables for driver circuit and an optical fiber that sends the trigger for the voltage pulse.

Gas is inserted trough a separated channel that goes from one end of the source to the other end

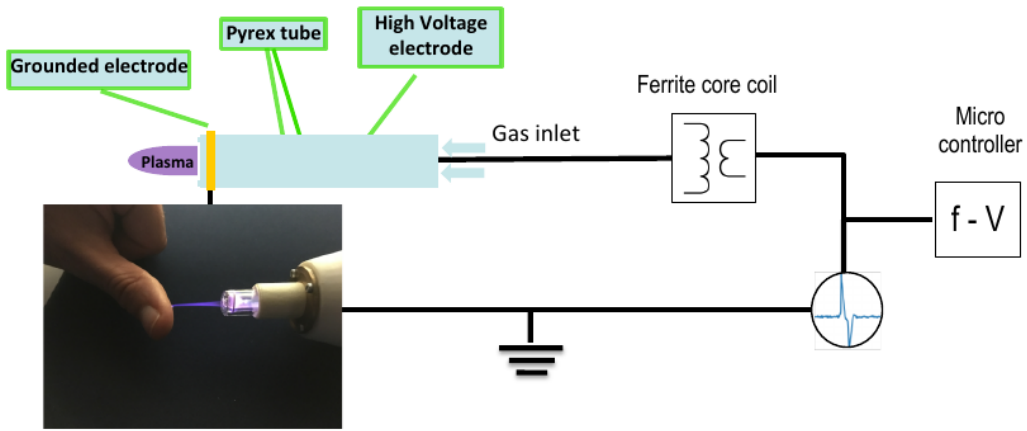


Figure 2.1: Scheme of the source. The micro-controller on the right sends a trigger signal to produce variable voltage on the coil mounted in the head, that produces an high voltage pulse on the electrode. The electric field ionizes the neutral gas and produces the plasma plume in the picture. The grounded ring around the nozzle is removable.

near the electrode. The nozzle at the end of the head can be selected between different materials and shapes. For this study we utilize a plastic nozzle that expels plasma through a cylinder with diameter of 1 mm and a cylindrical glass nozzle that shrinks at the end, until a diameter of 5 mm.

Prototype **A** is the first version used during this work, prototype **B** is the latest one. Generally the second one is developed with higher ionization efficiency, principal differences are:

- they have different geometries for the coils inside the head, so prototype **B** can produce higher voltage peak values;
- prototype **A** has positive voltage pulse polarity while prototype **B** has negative voltage pulse polarity;
- prototype **A** presents a problem of neutral gas diffusion in the area where there are the coils, in prototype **B** the two areas are not in communication (except for the electric connection of the electrode).

2.2 Electric scheme

In this chapter we discuss development of PCC eletric scheme and its characterization. To produce plasma as DBD, in air, with helium or argon as ignition gasses, it is necessary to apply high voltage difference in short distances, resulting in high electric field. It is common to produce electric fields with fast voltage pulses for various uses, including jet or DBD plasma production ([30], [31], [32])), the scheme that we use outputs a voltage pulse with an amplitude from 1 kV to 10 kV and pulses frequencies from 5 kHz to 60 kHz.

One representation of the electric scheme is in figure 2.2. As we explained before, the circuit divides in two parts: the controller, with power task and voltage pulse settings, and the head, where we ionize the gas and create plasma.

Line divides in:

- **Power line** : the controller is connected to a 220 V AC (50 Hz) power line. This signal goes in a transformer that reduces voltage value and to a diode bridge that rectifies the signal, resulting in an output of 22 V DC. This voltage powers the Driver Circuit on the head.

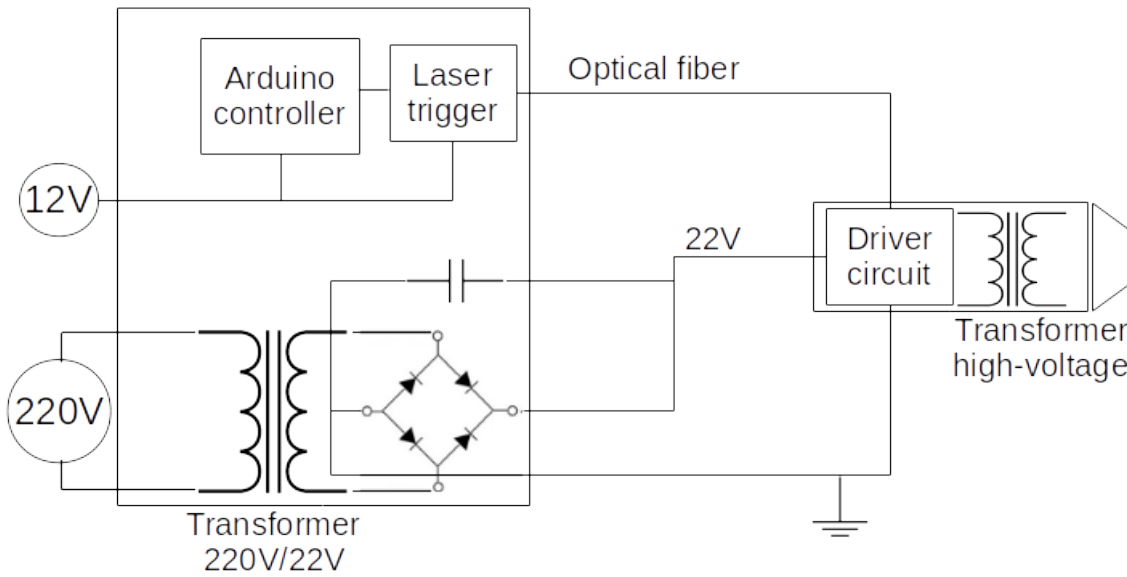


Figure 2.2: Electric scheme of the source. On the left there is the controller, on the right there is the head.

- **Arduino and trigger :** Arduino and a laser are connected to a power line at 12 V. One of the Arduino analogical outputs sends a PWM wave to the laser trigger, that transmits an optical signal with the same duration and pulse repetition rate of the PWM through an optical fiber. The fiber ends on a photodiode installed on the driver circuit that works as a switch to trigger the voltage pulse. With this setup pulse repetition rate and pulse amplitude are set by Arduino and the high voltage signal that circulate on the head is entirely decoupled from the controller, avoiding problems of signal reflection on the power line or the Arduino.
- **Head :** on the driver circuit there are the photodiode, a capacitor and a MOSFET that works as a switch for conductive and charging phases of the circuit. When the photodiode measure the laser signal voltage goes from power value to 0 and the capacitor starts charging. When the trigger signal ends, the voltage goes back to power value and the variation leads to a peak of thousands V on the output of the secondary circuit, connected to the electrode. Pulse repetition rate, f , is set precisely by the Arduino, PWM duration is set giving the opening time of the MOSFET, i.e. the duration of the charging time of the capacitor.

We present an example of voltage values on relevant components in figure 2.3, obtained with a simplified scheme with Spice. Once the PWM trigger starts, voltage on the primary goes from power value to 0, after $6\ \mu s$ the PWM signal ends, and the output of the secondary circuit shows a peak of $-5000\ V$ and width of $1.2\ \mu s$. A longer PWM implies a longer charging time and an higher voltage. Ultimately, amplitude of the pulse is proportional to the width of the PWM signal and we can calibrate source peak output V_p in function of it Δt for every pulse repetition rate f . It is necessary to note that when we end the charging phase, at the end of the PWM signal, we have a voltage peak also on primary circuit with amplitude of $150\ V$ and several oscillations of the same amplitude on the secondary. Those could influence the output behavior if we set pulse repetition rates too high, i.e. for values that would result in signal periods comparable to Δt .

We will study and compare output parameters for the two prototypes.

2.3 Output characterization

The electric field generated by the electrode define plasma creation and discharge features. We want to study the dependency of plasma behavior from voltage peak value and from pulse repetition rate, f . In addition, medical application of plasma requires low current intensity on target, in this study

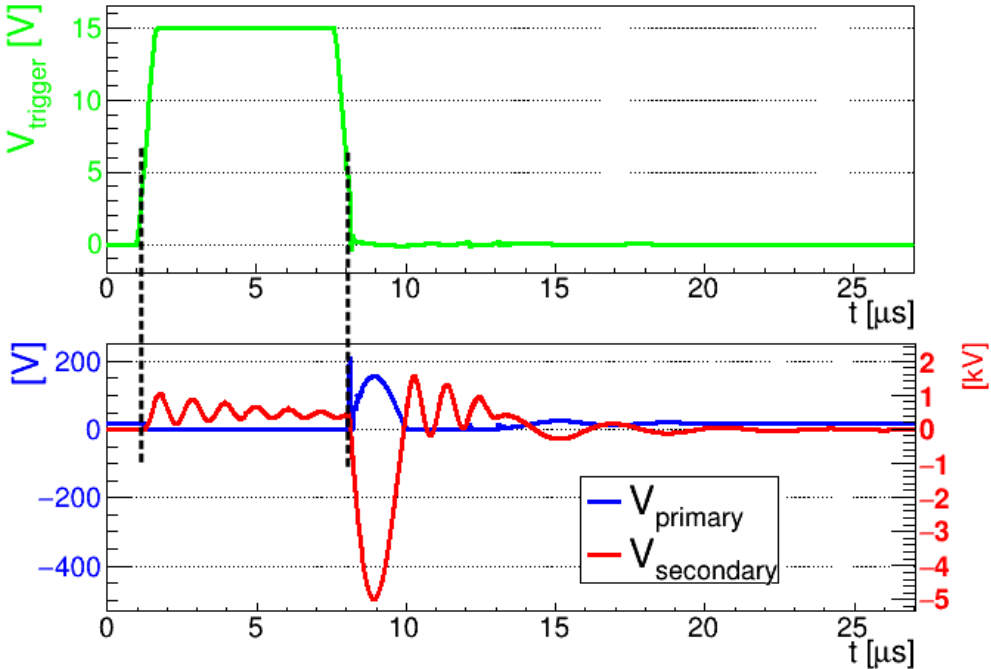


Figure 2.3: Scheme of signal propagation. Top in green there is the PWM trigger signal; bottom in blue there is the voltage of primary circuit with values in volts, in red the voltage of secondary circuit with values in kilovolts.

it's measured current intensity flowing on a copper sheet targeted by the plasma plume at a certain distance. Ultimately the different parameters for the measures are: Δt , opening time of the MOSFET in the circuit that is proportional to voltage peak value, and f , pulse repetition rate.

We measure voltage signals with a voltage probe (*hv probe*) built for high voltage measurements *Tektronix P6015A*, with an attenuation factor $\times 1000$. The voltage output from secondary circuit is taken right before the connection between secondary circuit and electrode. Current signal are measured with *Tektronix CT2* current probe for current measurements. This probe have an output of 1 mV for a current of 1 mA. We observe both signals with a *Yokogawa DL9040* oscilloscope, that is capable to store the total waveform that we measure.

We first take measurements without gas flow to characterize output voltage of the circuit, after we set an helium flow of 2 L/min, to measure the output in presence of plasma. For both conditions we measure outputs changing Δt for different repetition rate f . We measure also the mean current intensity over a time period, i.e. an effective current intensity I_{eff} , to evaluate plasma application's effects over a longer time period.

Every lenght measure is done with a decimal caliper, that gives a measurement uncertainty of 0.1 mm.

2.3.1 Measurements without gas

We set a repetition rate f and measure voltage signal for different values of the opening time Δt in the operational range. To assure that a voltage pulse ends before another starts, this range is different for different f : if we have more pulses in a given time and take into consideration pulse oscillations, the range of possible Δt is smaller for higher rates. A typical voltage waveform is in figure 2.4 (a). We want to verify proportionality between amplitude of the peak, V_p , and Δt , for different f . The signals are analyzed with a low-pass filter where we evaluate their Fourier Power Spectrum (using ROOT C++ libraries [33]) and reconstruct the signal without higher frequencies, to exclude noise fluctuations. The reconstructed peak is an asymmetric function in time as in figure 2.4 (b) that we fit with a Landau function [34] and obtain peak value and position. The error on the measure is evaluated

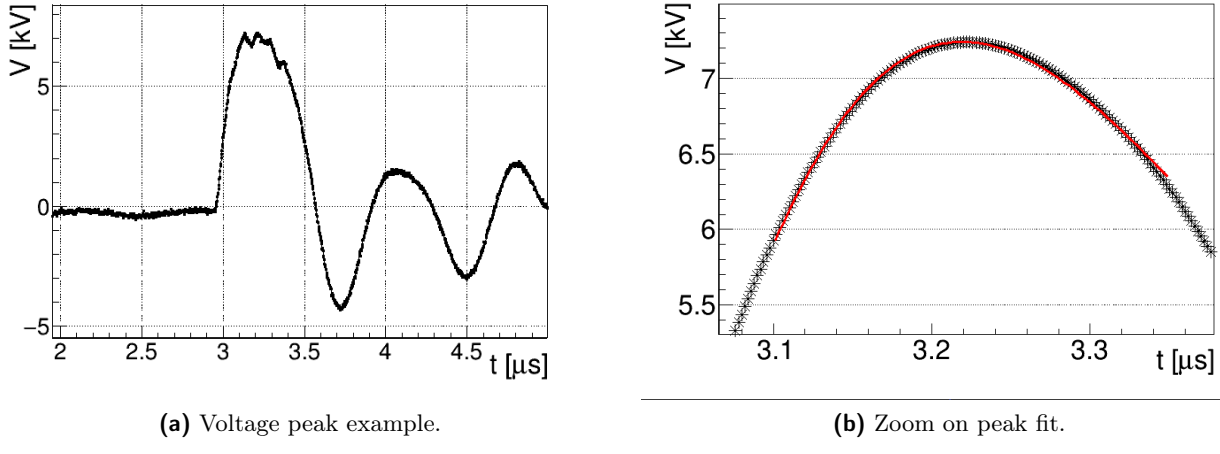


Figure 2.4: Example of voltage measurements with prototype **B** for $f = 5$ kHz and $\Delta t = 4 \mu$ s (a) and its fit to estimate peak value and time (b).

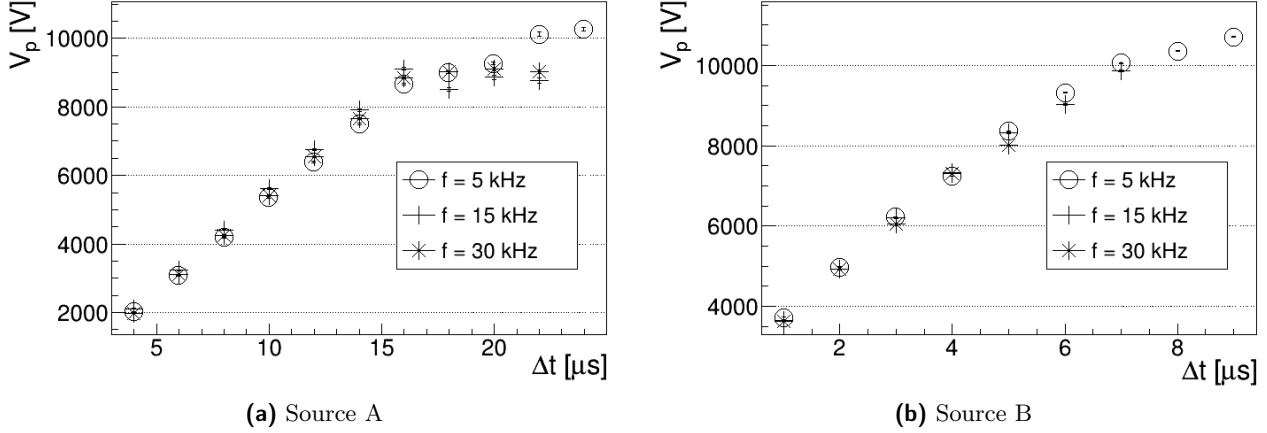


Figure 2.5: Absolute voltage peak values of secondary circuit output in function of Δt at different f , for both prototypes. As we can see voltage peaks show linear behavior for $\Delta t \leq 15 \mu$ s.

adding contributes from the low-pass filter.

Results are shown in figure 2.5 for prototype **A** and **B**. For **A** we can see a linear behavior for $4 \leq \Delta t \leq 16 \mu$ s, with peak values from 2.02 ± 0.01 to 9.25 ± 0.05 kV; for larger Δt the relation is not linear. The upper limit on Δt is given by the need of a minimum time interval between two pulses. Also for **B** we can see a linear behavior, but with higher values: for $1 \leq \Delta t \leq 8 \mu$ s voltage peak goes from 3.66 ± 0.06 to 11.76 ± 0.22 kV. With this source the upper limit for Δt is chosen considering the maximum voltage value sustainable by the dielectric. To avoid the risk of dielectric breakdown we set the maximum opening time for prototype **B** at $\Delta t = 8 \mu$ s.

Voltage output doesn't show significative differences changing repetition rate. To confirm this observation we fit data with a linear function in the range $0 - 16 \mu$ s for **A** and range $0 - 8 \mu$ s for **B**. Parameters resulting from the fit are compared as in figure 2.6. Values are displaced with random distances from the mean value, so it can be concluded that the behavior is not defined by the repetition rate.

2.3.2 Measurements with gas

We introduce helium, with a flow of 2 L/min, at the end of the head near the electrode, producing plasma in DBD conditions. We want to study how voltage value changes with plasma introduction and the intensity of current carried by plasma on a conductive target. To assure safety of plasma

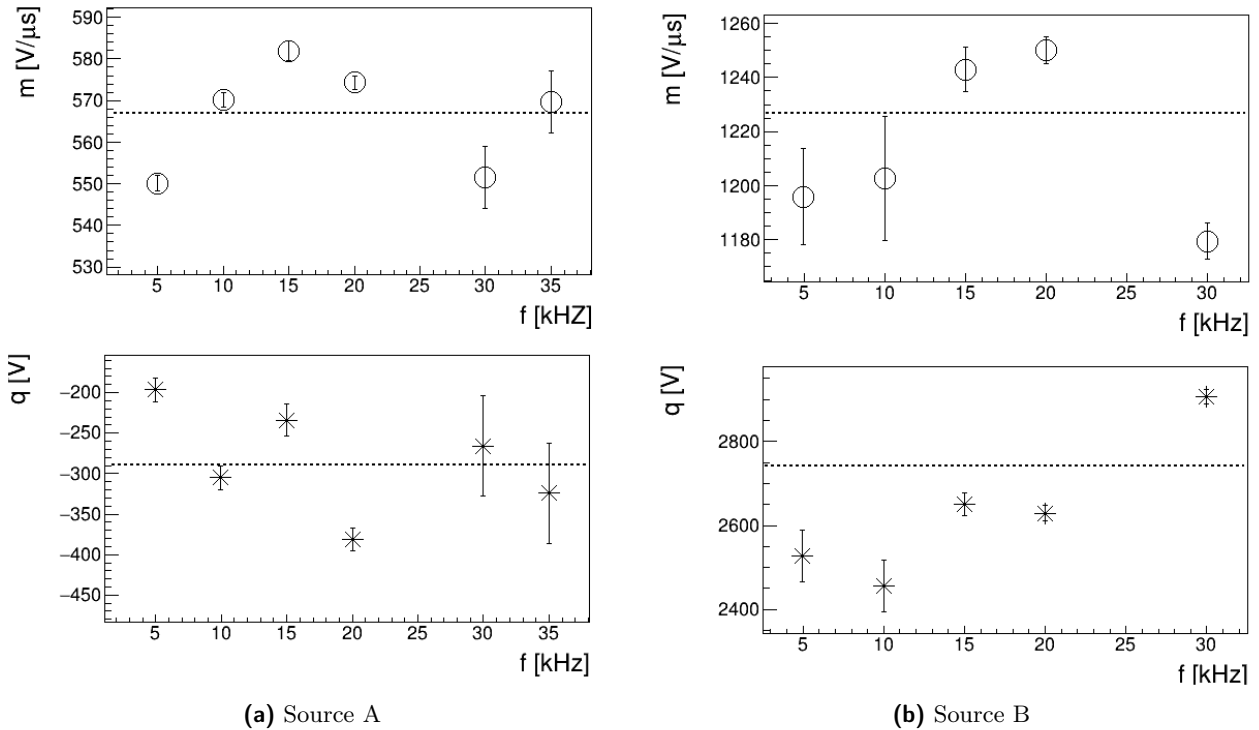


Figure 2.6: We fit voltage peak in function of Δt with a linear function $V_{peak} = m\Delta t + q$, in figure we present fit parameters at different repetition rates for both sources. Dashed line is the average value of the parameter. There isn't a specific behavior in parameters, so we conclude that output voltage doesn't depend on pulse repetition rate.

application we want to avoid large current intensities with possibility of arc formation. Studies of conditions for DBD discharges and arc transitions ([35], [36], [37]) suggests that for fast pulses it's safe to have current intensity < 10 mA.

Current intensity is measured with a copper sheet of dimensions $10\text{ mm} \times 10\text{ mm} \times 1\text{ mm}$. The plasma plume impacts on the sheet that is connected to the current robe that converts the signal in a voltage measurements that we can read on the oscilloscope. We are measuring low current intensities so we have to pay attention to cables shielding, decreasing noise. The relation between current intensity and target distance is studied in [28]. In this work we choose a distance between target and electrode around typical values for treatments: 10 mm for prototype **A** and 15 mm for prototype **B**.

In figure 2.7 we present a measure for $\Delta t = 8\text{ }\mu\text{s}$ and $f = 5\text{ kHz}$ with prototype **B**. For both sources there is a current peak in correspondence of voltage pulse, that increases with voltage. However for prototype **B** there are measurements where the peak is so low that it is covered by noise.

Data analysis is the same described before, for both voltage and current values. Results are shown in figures 2.8 and 2.9, measurements where the current peak is not distinguishable from noise are excluded from plots.

Voltage peaks are lower than values without gas. It is an expected behavior if we consider the plume as an additional resistive load at the end of the circuit ([38]). Also for this measures we observe a linear dependency between voltage and Δt for $V_p \leq 10\text{ kV}$, we can again compare linearity for different f . Current intensities increase as voltage and are higher for prototype **A**, as expected given different distances electrode-target. Analysis of linearity also for those measures can show if there is a different behavior changing pulse repetition rate. Figures 2.10 and 2.11 shows results of the linearity study for different pulse rates.

For voltage fit we find parameters scattered around their average value for both sources, confirming the hypothesis that voltage growth is independent from pulse repetition rates. For prototype **A** we find

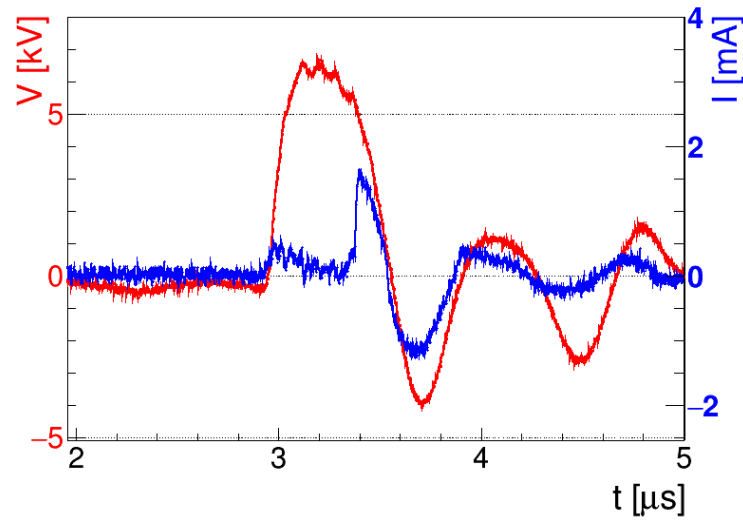


Figure 2.7: Example measurements with prototype **B** for $f = 5$ kHz and $\Delta t = 3$ μ s

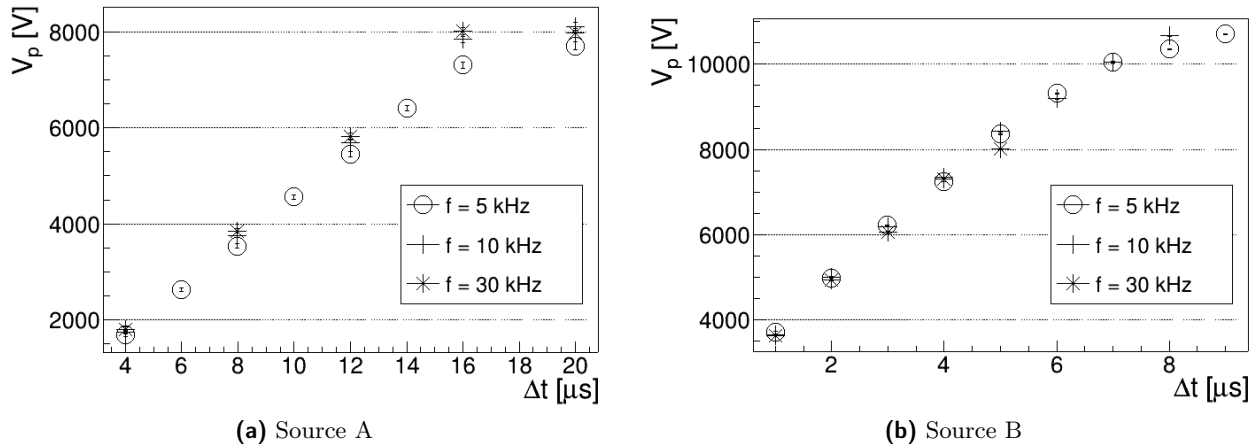


Figure 2.8: Absolute voltage peak values of secondary circuit in function of Δt at different f , with an helium flux of 2 L/min, for both sources.

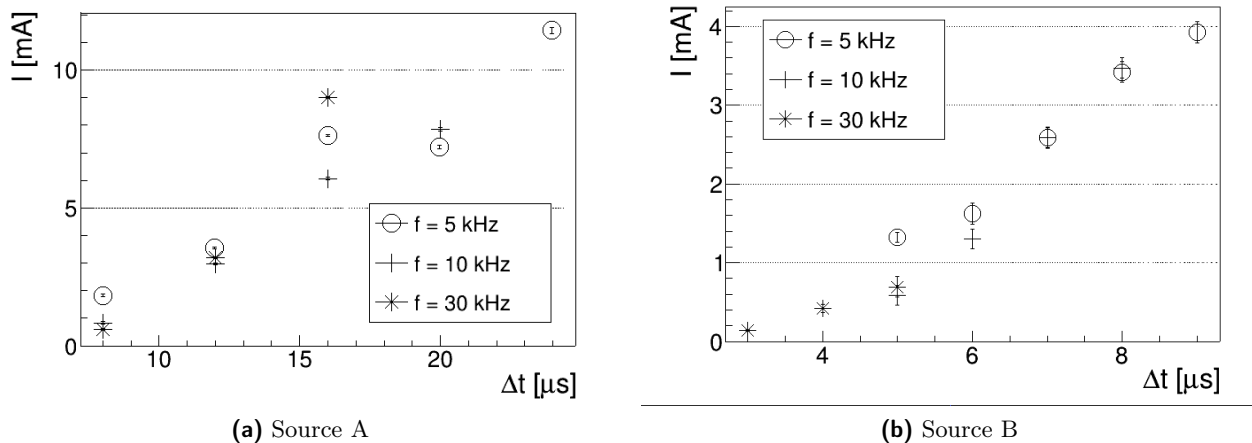


Figure 2.9: Absolute current peak values measured with helium flux of 2 L/min, on a copper target, in function of Δt at different f , for both sources.

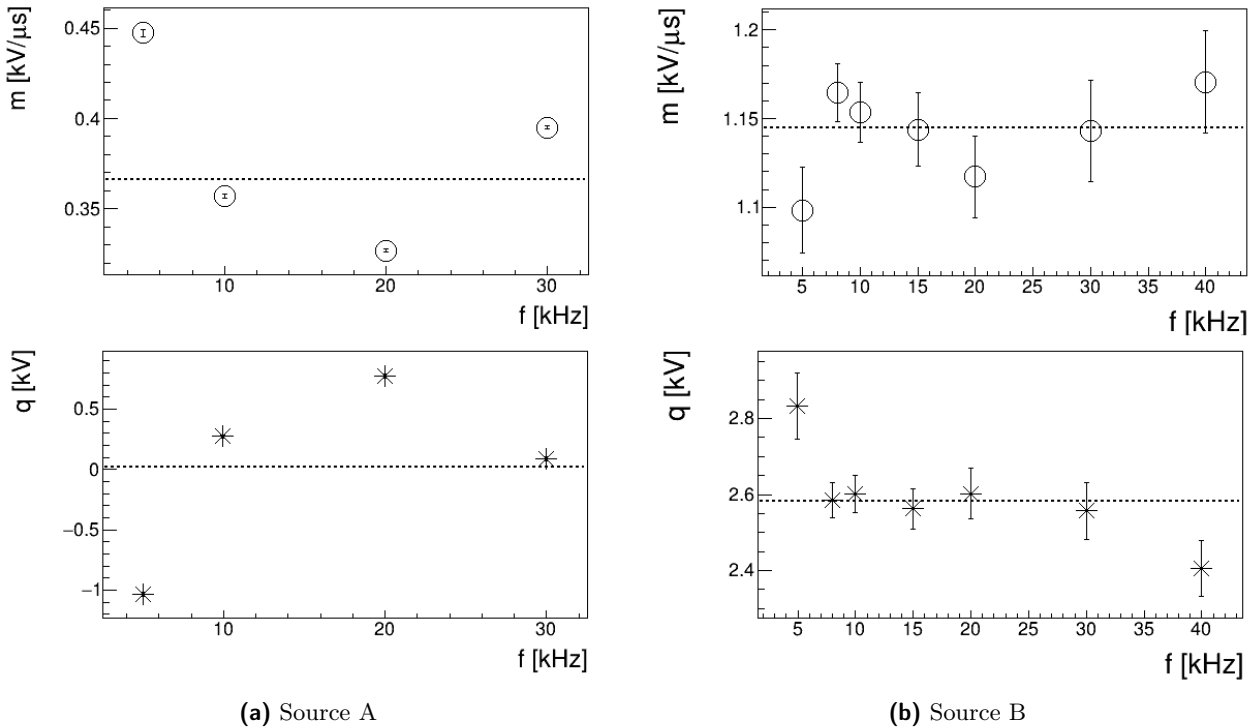


Figure 2.10: We fit again voltage peak in function of Δt with a linear function $V_{peak} = m\Delta t + q$, in figure (a) and (b) there are fit parameters at different repetition rates for both sources. Dashed line is the average value of the parameter. Also when there is plasma we don't find specific behavior in parameters, so we conclude that output voltage doesn't depend on pulse repetition rate.

the voltage average increase $m_V = 0.366 \pm 0.001 \text{ kV}/\mu\text{s}$, for prototype **B** $m_V = 1.145 \pm 0.008 \text{ kV}/\mu\text{s}$, higher, as explained before.

Current values shows a different behavior: in prototype **A** we find a increasing parameters with increasing frequencies, in prototype **B** data are more scattered and we couldn't extrapolate a behavior. Despite this behavior the slope is in the same range of values for both prototypes, with a maximum for **A** of $m_I = 1.10 \pm 0.01 \text{ mA}/\mu\text{s}$ and for **B** of $m_I = 1.04 \pm 0.17 \text{ mA}/\mu\text{s}$.

The parameter trend in prototype **A** could suggest a variation of reaction parameters happening inside the plasma. If we have more ionization reactions with higher repetition rate, we would have higher charge densities and measure more current intensity. Due to low signal to noise ratio in measures for prototype **B**, it is not possible to esclude a relation between current slope and repetition rate for this source, however it is established a maximum limit value to take into consideration when using the device.

Time intervals From voltage and current waveforms we can also extrapolate informations on time width of those signals. They can be defined as the FWHM of measured peaks, evaluated as the time when we measure half of tension or current maximum value. As the characterization of the sources shows an almost equal behavior, this study is made only for the latest version of it prototype **B**, that's the only one used in the following chapters. Results are shown in figure 3.6. For every repetition rate there is a quadratic behavior of voltage widths with a minimum for a $\Delta t = 5 \mu\text{s}$. It is possible to give an estimation of pulse width with a mean value between this minimum and maximum values obtained for $\Delta t = 1 \mu\text{s}$, it is $T_V = 963 \pm 15 \text{ ns}$. For currents, widths have great uncertainty where the peak is low, but it is possible to evaluate a mean value for $\Delta t \geq 6 \mu\text{s}$, and it is $T_I = 968 \pm 28 \text{ ns}$. Values from the two measurements are compatible and they are a good estimation of pulse time duration.

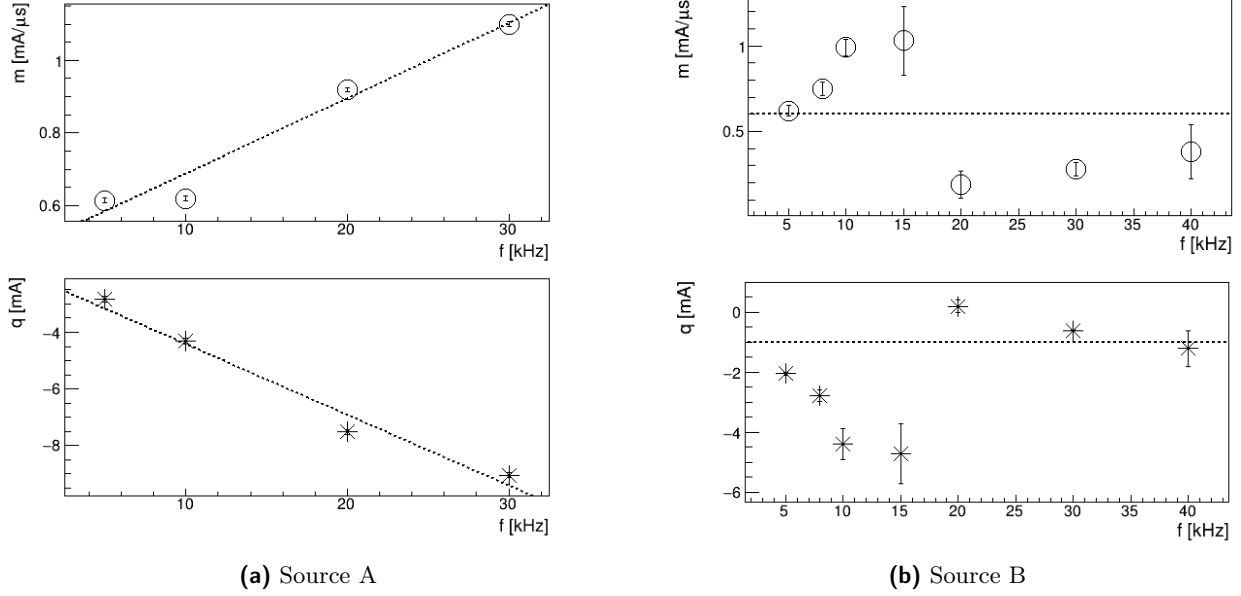


Figure 2.11: We fit also current peaks with a linear function $I_{peak} = m\Delta t + q$, in figure we see fit parameters at different pulse repetition rates for both sources. For prototype **A** we find a linear dependency from f , in dashes in the figure. For prototype **B** we find again a random displacement around the average value.

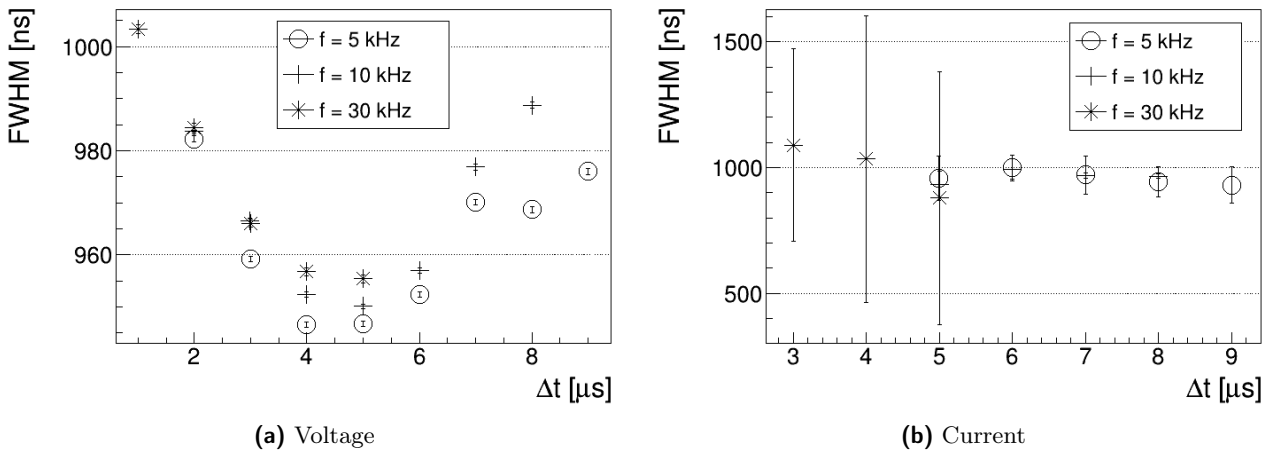


Figure 2.12: FWHM of voltage and current pulses varying opening time, for different pulse repetition rates.

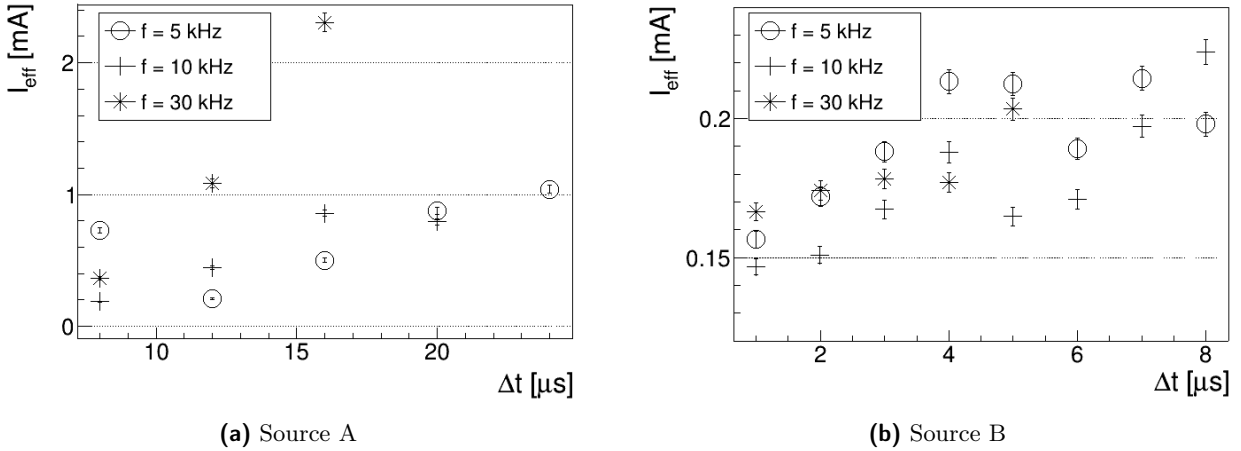


Figure 2.13: Effective current values measured for a time interval of 1 ms.

2.3.3 Effective current

Current effects in applications on biological tissues have to take into consideration current intensity in a time interval typically larger than the pulse widths used in our sources ([39], [28]). It's possible to estimate an effective current that is more appropriate to take into consideration when evaluating damage due to currents, as a mean of current intensity in a defined time interval calculated with equation 2.1, taking $t_2 - t_1 = 1 \text{ ms}$. The effective current takes into consideration that current values are very small for all the time between two pulses.

$$I_{\text{eff}} = \sqrt{\frac{1}{(t_2 - t_1)} \int_{t_1}^{t_2} I^2 dt} \quad (2.1)$$

Figure 2.13 shows effective currents measured for both sources. Values are significantly smaller than maximum peak values, especially for prototype **B** where oscillations after the main peak are smaller. The maximum value for the two prototypes is given by $I_{\text{effA}} = 2.47 \pm 0.07 \text{ mA}$ and $I_{\text{effB}} = 0.23 \pm 0.01 \text{ mA}$.

2.3.4 Plasma impedance

From voltage and current measurements we can define plasma's electric behavior, in this subsection we try to estimate plasma impedance with measurements from prototype **B**. Voltage output from head's transformer can be modeled as a damped sine wave around the peak, as in equation 2.2, where V_{pulse} is the amplitude of the undamped pulse, τ is the characteristic damping time and f_{V_s} is the explicit parametrization of the frequency of the single pulse that we observe on measurements.

$$V_S = V_0 + V_{\text{pulse}} \sin(2\pi f_{V_s} t) e^{-t/\tau} \quad (2.2)$$

We can study how plasma impedance changes for different frequency pulse f_{V_s} to understand its electric behavior. Frequency pulse it's different for every opening time of the circuit, Δt , but it's constant when changing pulse repetition rate, as explained before analyzing voltage outputs. In figure 2.14 there is an example of a peak fitted with the function in formula 2.2 while in figure 2.15 we show the resulting fit parameters for different Δt .

With higher opening times V_{pulse} is higher as expected, while f_{V_s} and τ have their own behaviors that depends from V_s . To estimate plasma's impedance it's useful to observe that voltage peak is quite large in time: it varies of less than 3% of peak's value in an interval of 150 ns around it. As voltage and current peaks times differs always by a time interval $|t_{V_p} - t_{I_p}| \leq 150 \text{ ns}$, it's possible to assume

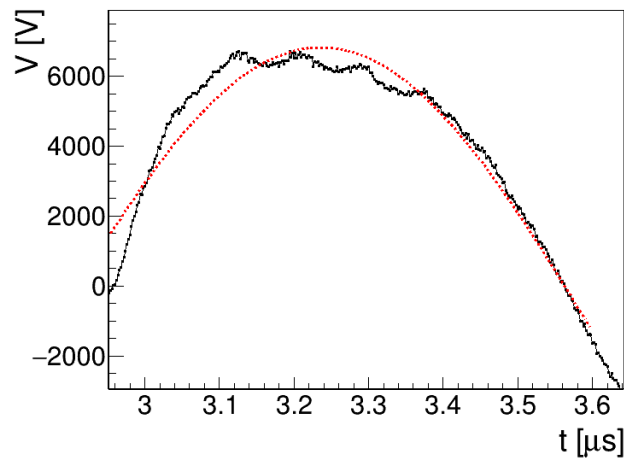


Figure 2.14: Example of a fit of voltage measurements with function 2.2.

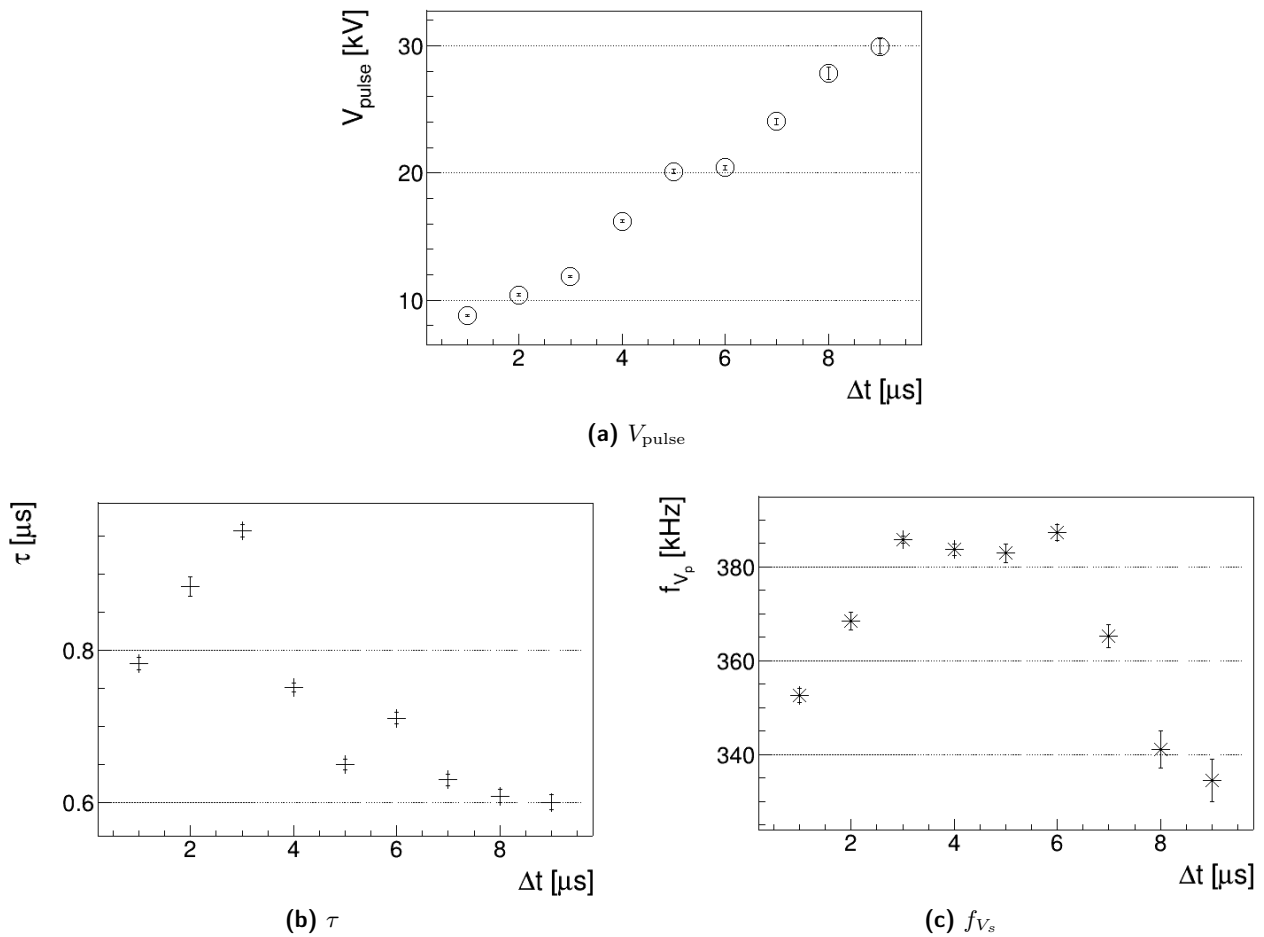


Figure 2.15: Dumped sin fit parameters, as in equation 2.2, for pulses with $f = 8 \text{ kHz}$ and different Δt .

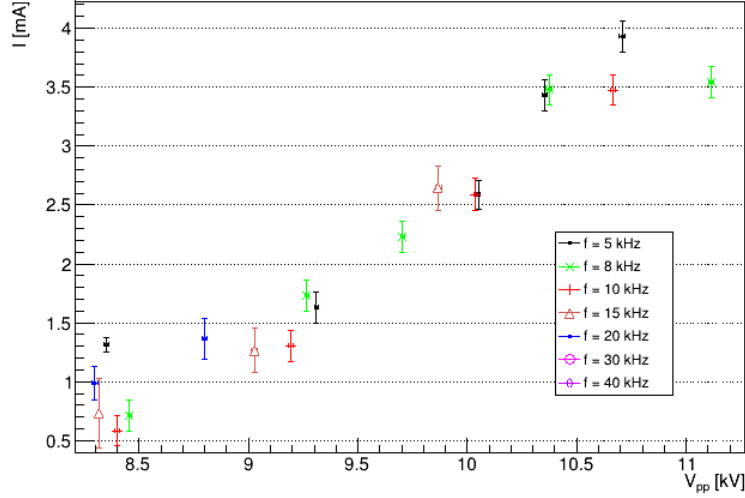


Figure 2.16: Voltage peak values against current peak values for different Δt and f .

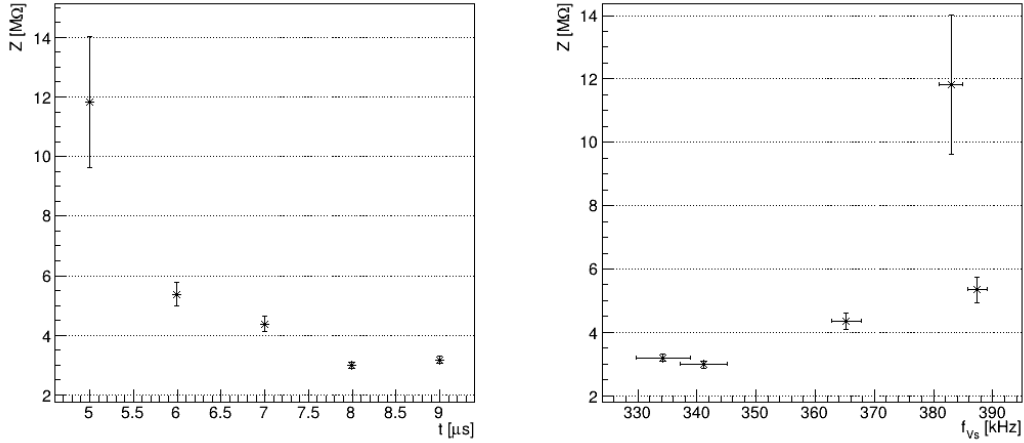


Figure 2.17: Impedance module estimation for different opening times (left) corresponding to different frequencies fit parameter (right).

$V_{t_{I_p}} \simeq V(t_{V_p})$, i.e. that voltage during the current peak maximum is equal to voltage peak value. With this approximation, we can study voltage peak values in function of current peak value, as in figure 2.16. We can have an estimation of average plasma resistance from a linear fit or for a particular Δt it's possible to estimate it as $R = \frac{V_p}{I_p}$. Results are shown in figure 2.17, changing opening times and changing frequency of single pulse f_{V_s} .

From the graphs it's possible to extrapolate that plasma resistance goes from $2.98 \pm 0.11 \text{ M}\Omega$ to $11.82 \pm 2.19 \text{ M}\Omega$, with near constant values in the range of opening times $7 - 9 \mu\text{s}$. From a deeper analysis and specific measures it could be possible to expand the analysis here presented and estimate plasma's electrical capacitance or inductance.

Chapter 3

Shape and dynamics

PCC expels a column shaped plasma plume that emits radiation in a visible range, with different colours and intensity for different gas composition, gas flow and intensity of electric field. In figure 3.1 there are pictures of plasma plume with different gas used to start the discharge.

Recent studies shows that what is expelled is not a continuos flow, but the plume is formed by compact collections of emitting particles called *bullets*. Those bullets forms in coincidence of voltage pulses and propagates in air with velocities from 10 to over 150 km/s ([40], [41]).

An example of this phenomenon measured with the experimental apparatus used in thesis is shown in figure 3.2.

Plasma bullets still needs to be studied in depth, at today are known the basic dynamic of formation and expulsion. Some general features are that:

- bullets velocities are $> 10 \text{ km/s}$;
- bullet formation, it's velocity and it's travel distance depend on applied voltage on the electrode.

The scope of this experiment is to observe plasma bullets produced by our source, their shape and their velocity and how they change with different discharge conditions.

Given their typical velocities and the temperature of the plasma, bullet propagation is tought to be related to a travelling ionization front. This propagation can be studied with simplified simulation of DBD discharges, where it's reproduced the behaviour of plasma bullets ([42], [43]) or the interaction between plasma and a target ([44]). Possible explanation for bullet propagation are analyzed at the end of this chapter, with estimation of electron temperature and mobility that give better insight on the phenomenology.

3.1 Experimental setup

To visually observe dynamics of plasma formation and propagation with enough resolution, it is needed an acquisition setup with a fast camera that has short integration time, below 20 ns, and an image intensifier that allows to visualize light emitted in such a short time interval.

To guarantee synchrony between plasma discharge and frame acquisition it is necessary to consider instruments and plasma source specific delays and give appropriate triggers.

Experimental setup is shown in photo 3.3 and a scheme is presented in 3.4. In the scheme there are the voltage signal lines that trigger the discharge and the acquisition, the optical acquisition apparatus pointed at source exit and the measurements acquisition instruments that are a computer and an oscilloscope.

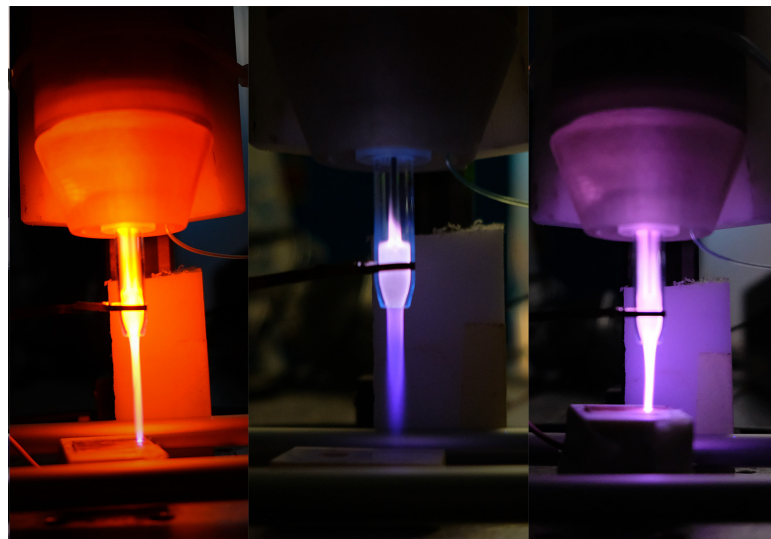


Figure 3.1: Plasma plume pictures with different gasses used to start the discharge: neon on the left, argon in center and helium on the right. The source points to a conductive target positioned in front of the nozzle, after 22 mm for neon and argon, after 14 mm for helium.

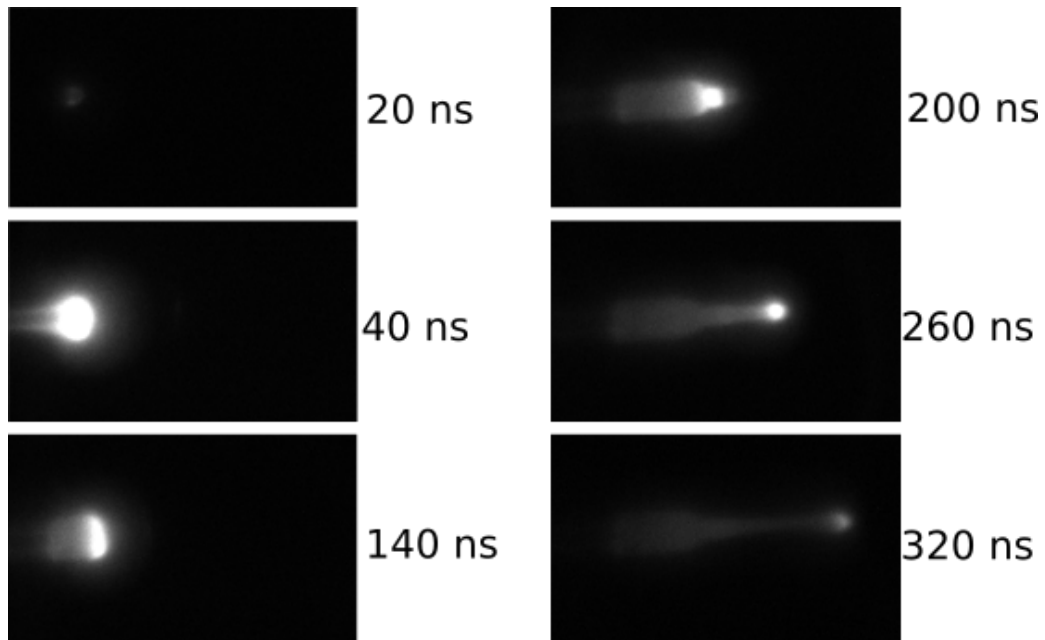


Figure 3.2: Example of helium plasma bullet expulsion, as measured with our experimental setup. The single frames are taken with a fast camera with integration time of 15 μ s.

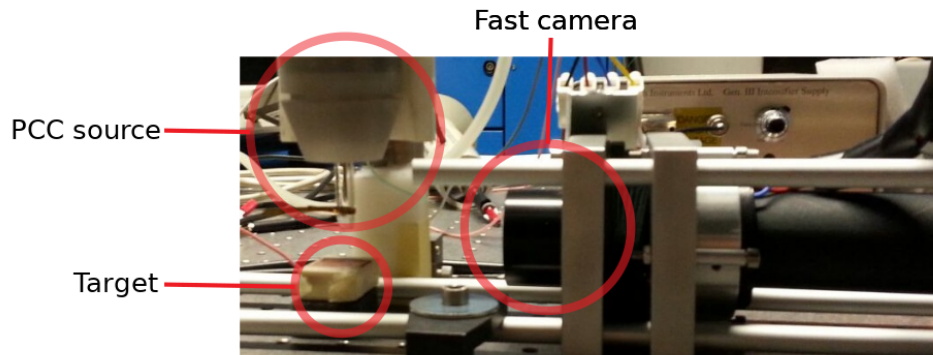


Figure 3.3: Picture of the experimental setup. The source PCC is mounted vertically and points to a removable target that can be positioned at different heights. Plasma is observed with a fast camera from the side.

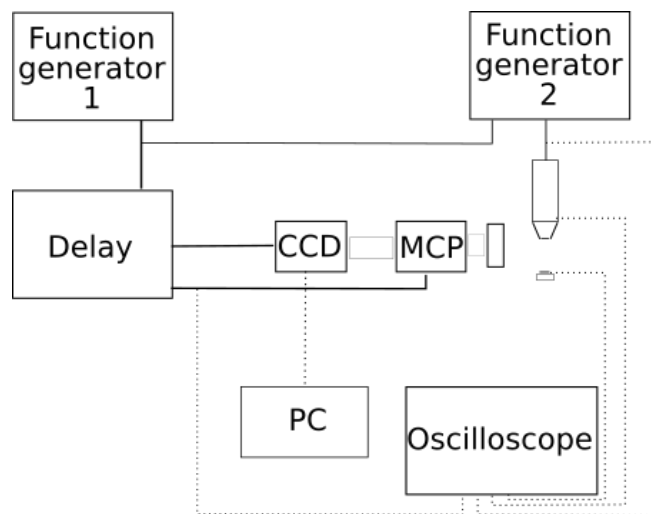


Figure 3.4: Experimental setup scheme. Function generator 1, function generator 2 and delay generator send trigger signal to camera (CCD), to source and to image intensifier (MCP), full lines in the scheme. Camera sends measured frames to a computer (PC). From source, source's target, function generator 2 and delay are taken signals read on the oscilloscope, pointed lines in the scheme.

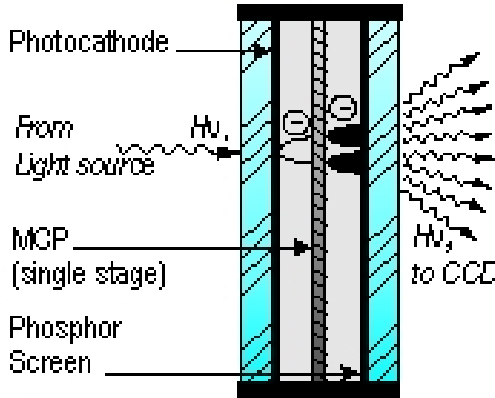


Figure 3.5: Micro Channel Plate image intensifier functioning.

3.1.1 Source and optical setup

Optical apparatus is composed by a lens coupled with a Micro Channel Plate image intensifier (MCP). An MCP works as in figure 3.5: for every photon received it emits many photons with little angular deviation.

Those photons are received by an high-speed camera *Point Grey Flea* ([45]) equipped with a CCD of 1024×768 square pixels $4.75 \mu\text{m}$ wide. Every frame is sent to the pc where FLIR software elaborates and saves them in pgm format ([46]).

3.1.2 Source, power lines and electric signals

The source utilized is the latest prototype, **B** in chapter 2. It has a voltage pulse peak value between 3 and 10 kV, regulated by the lenght of the trigger signal Δt (see chapter 2). To synchronize measures and discharge the trigger signal a generator function gives the trigger signal (generator 2 in the scheme) instead of the usual controller module of the source.

The source is positioned vertically at a distance of 42.0 ± 0.1 mm from optical bench, with the glass nozzle that allows to observe plasma formation inside it (external diameter 8.0 ± 0.1 mm, internal diameter 6.0 ± 0.1 mm). The distance from the end of the electrode and nozzle exit is 12 mm. At the exit the nozzle shrinks for 3.0 ± 0.1 mm, until a diameter of 5.0 ± 0.1 mm

Under the source is possible to position targets. Two different targets are used at different heights: a conductive target and an insulating target. The first one is a copper square sheet of dimensions $10 \text{ mm} \times 10 \text{ mm} \times 1 \text{ mm}$ (used for current measures in chapter 2), the second one is a plastic material.

CCD camera is powered by a common voltage supply, while image intensifier MCP is powered by an high voltage supply. A delay generator trigger both instruments, with different delay times (see next section).

The oscilloscope *Yokogawa DL9040*, utilized in chapter 2, reads on different channels the trigger signal given to source head, the trigger signal given to MPC, the voltage electrode with high-voltage probe *Tektronix P6015A* and the current intensity when it's used the conductive target. Measurements of current intensity are done by a voltage probe with attenuation $\times 10$ that measures the voltage drop on a resistance of $1 \text{ M}\Omega$ connected to the conductive target.

3.1.3 Trigger synchronization

Experiment's objective is to observe plasma formation and propagation in synchronization with the measurement of voltage on the electrode, so it's necessary to know precisely discharge and measure times.

The trigger lines is composed with:

- function generator *Or-x 310*, 1 in figure, that sends a square pulse with set amplitude and width, with pulse repetition rate f ;
- function generator *Lecroy 9210*, 2 in figure, that sends a square wave with repetition rate given by the trigger, with constant amplitude and variable width Δt ;
- delay time generator *Stanford DG535*, that sends a square wave with constant amplitude and repetition rate given by the voltage input. Start time of this signal is given by input starting time plus settable delays (4 different channels).

Every measuring instrument has it's own time delay between trigger signal and effective measure. The higher delay is the arming time for fast camera, in the order of ms, the shortest one is the integration time for acquisition system, that starts from the activation of the image intensifier and span 15 ns.

A time line is shown in figure 3.6, an example of signals taken with the oscilloscope is in figure 3.7. There are three relevant times defined by function and delay generators:

1. t_0 is the starting time for the square pulse given by *Function generator 1*, with an amplitude of 5 V and repetition rate f . The pulse is the external trigger for *Function generator 2* and the voltage input of *Delay generator*. The square wave that triggers the voltage pulse on the source starts at t_0 from *Function generator 2*; it has a time width of Δt that defines voltage amplitude (see chapter 2) and repetition rate f . The trigger signal that arms the camera starts at t_0 from *Delay generator*.
2. t_{DIS} is the effective discharge starting time, when the voltage peak starts. From trigger signal end to voltage peak start there is a time delay given mainly by the response time of the photodiode on source head. Measuring the signals as in figure 3.7, it's possible to estimate this delay as 987.7 ± 56.7 ns, constant for every f and Δt . The discharge happens after t_{DIS} , measurement times must be inside the grey zone in the scheme.
3. t_{MIS} is the measurement time, when MCP is triggered on. *Delay generator* gives the delay between t_0 and t_{MIS} , called t_D , with possible steps of 1 ps. Changing t_D it's possible to see plasma dynamics at different times that corresponds to different electrode voltage values, as in figure 3.7.

Integration time for a single frame is 15 ns, so the time step between two measures has to be larger than it. Time steps chosen are 20 ns for high resolution measurements, 50 ns for standard measurements.

It's important to point out that pulse repetition rates are $f \geq 1$ kHz corresponding to a time interval between two pulses lower than 1 ms; while the measure interval time between the acquisition of two frames is larger than 50 ms because of the camera. It is not possible to see two consecutive times for the same discharge, the frames are always measures of different discharges.

Each pixel on the CCD has a minimum and maximum intensity value, is possible to maintain the measure on the wanted level changing the settings on camera acquisition software. One of the parameters is the *Shutter time*, the opening time of the camera shutter. If the emission intensity is too low we can set the shutter time larger than the time between two acquisition, to acquire a frame that is the sum of two discharge. Another parameter is the *Gain* value, that amplifies or reduces the output. For each used gas we select an appropriate *Gain* value and an appropriate *Shutter time*.

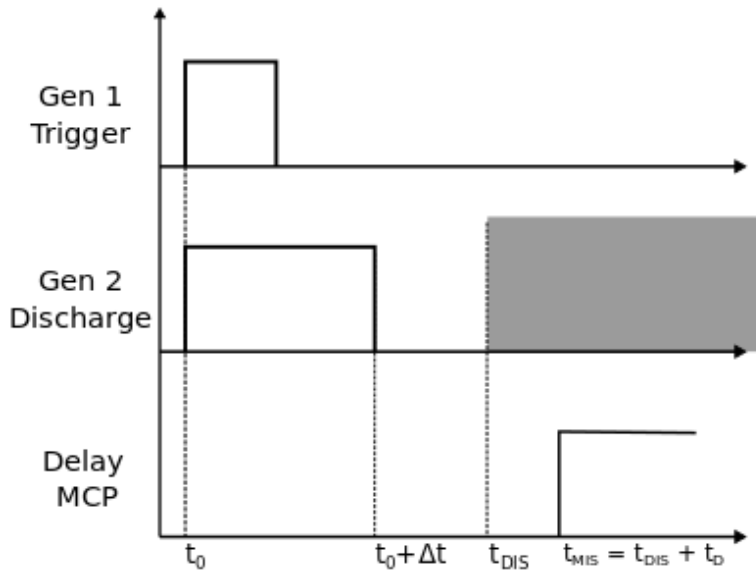


Figure 3.6: Time signal synchronization scheme: t_0 is the starting trigger time, Δt is the opening time for plasma source (see chapter 2), t_{DIS} is the starting time for the discharge and t_{MIS} the starting time for the MCP i.e. the measure time

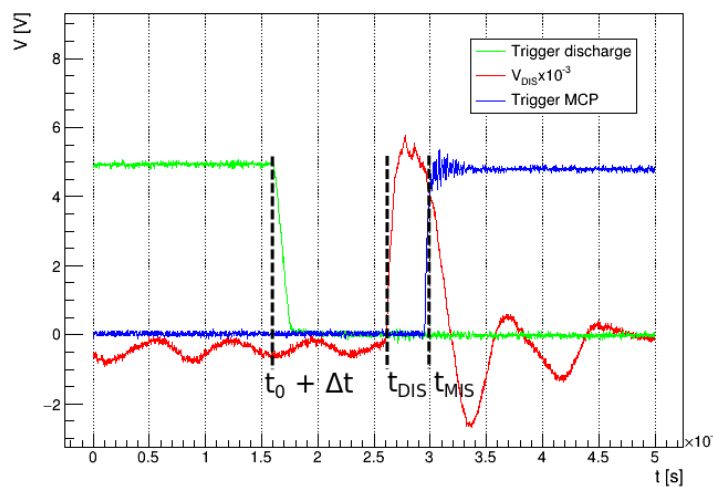


Figure 3.7: Example of oscilloscope measure. In green the discharge trigger, in red the electrode voltage output and in blue the MCP trigger. The dashed lines indicate times described in 3.6.

Gas	Setup	Δt [μs]	Target	Target position [mm]	Flow rate [L/min]	Other	Δt_D [ns]
He	A	3, 3.5, 4	-	-	2	-	20
	B	3.5	-	-	1	-	20
	C	3.5	-	-	3	-	20
	D	3.5	-	-	4	-	20
	E	3, 3.5, 4	Insulator	24	2	-	20
	F	3, 3.5, 4	Conductor	32	2	-	20
	G	3, 3.5, 4	Conductor	24	2	-	20
Ne	A	2, 2.5, 3	Insulator	24	2	-	50
	B	2, 2.5, 3	Conductor	32	2	-	50
	C	2, 2.5, 3	Conductor	24	2	-	50
	D	2, 2.5, 3	-	-	2	-	50
Ar	A	3.5	-	-	2	Grounded ring	50
	B	3.5	-	-	2	-	50
	C	3.5	Conductor	20	2	Grounded ring	50
	D	3.5	Conductor	20	2	-	50

Table 3.1: Description of measure setups. In first column there is the gas; second column is the setup name; third column is voltage pulse time width; four and fifth columns are target information, if it's used a target; sixth column is gas flow; seventh column are other informations, e.g. if it's positioned a grounded ring around the nozzle; eight column is the time step between acquisitions.

3.1.4 Different setups

Many parameters have an effect on plasma formation: voltage pulse repetition rate, voltage rise time, voltage peak value, gas type, gas flow, presence of a target and its features (see [40], [47]). This study presents different setups with three different gasses, as shown in table 3.1. There is a lower limit value for pulse repetition rate, different for each gas, under which there is no discharge. The electric behavior of the source is the same for values higher than this threshold (see chapter 2). For each gas is chosen a repetition rate value that allows the discharge to start.

Gasses with different composition will have different ionization reactions and will produce different reactive species, with different masses and ionization energies. With this study is possible to observe how peak voltage value, gas type and gas flow determine plasma bullet formation and affect its expulsion velocity.

A conductive target near plasma exit at ground potential will modify the electric field produced by the electrode. With this study is possible to observe how the target affects bullet expulsion and propagation. Furthermore the bullet can hit the target, introducing into reactions balance also the electrons on the target.

When argon is the neutral gas used to start the discharge a grounded conductive ring can be placed around the nozzle after the electrode, to help the start of the discharge.

3.1.5 Frame analysis and calibration

Once a measure setup is chosen, the first acquisition is set around the start of the discharge. On the oscilloscope is saved the signal waveform for every channel (setup as explained before), on the computer 5 frames for every t_D are saved. Measures are taken with steps of Δt_D until it is not possible to observe

plasma anymore.

Measure time from the start of the discharge can be evaluated from waveforms on the oscilloscope.

Frame analysis is done converting the pgm files in 2-dimensional histograms, with *TH2* class written in *ROOT* libraries (see [48]).

From the five frames taken it is evaluated the average value for each pixel. From the resulting frame the plasma bullet is isolated as the collection of pixels with maximum intensity in the frame. The estimation of the bullet position is given by the coordinates of its luminosity barycenter on the plane seen by camera, called x-y in the analysis. Once established the center, the points were luminosity goes under a certain percentage of the maximum define its contour. Bullet dimensions along x and y axis are evaluated from the contour, while average luminosity is given by pixel values inside the contour. With barycenter coordinates it's possible to compute bullet velocity using a finite difference formula [49].

Frame dimensions are found through a calibration with a known target: at plasma exit is positioned a plate with 4 holes, diameter of 1.0 ± 0.1 mm at the vertices of a square with an edge lenght of 10.0 ± 0.1 mm, and illuminated from behind with a torch. For the frame of this setup it's possible to extrapolate the pixel distance that corresponds to 10 mm for every square edge, average them, and calculate pixel's width in frames, resulting a value of $d_{pix} = 0.172 \pm 0.002$ mm.

3.2 Helium flow

Helium it's an element with standard atomic weight of 4.002, 1st ionization energy of 24.587 eV and 2nd ionization energy of 54.418 eV. It is easy to produce helium plasma, when ionized it emits radiation with principal wavelengths in violet and orange ($\lambda = 388.86$ and 587.56 nm).

In this work helium plasma is produced with pulse repetition rate $f = 5$ kHz and different voltage peak values, as explained in table 3.1. Delays are setted to take a single frame during every acquisition, for every measure are acquired 5 frames.

3.2.1 Plasma bullet description

A description of bullet propagation can be given with setup A, for $\Delta t = 3.5$ μ s, i.e. absence of a target and gas flow of 2 L/min.

It's possible to divide the phenomenon in four phases, as presented in figure 3.8: bullet formation, bullet displacement inside the nozzle, bullet expulsion and bullet propagation outside the nozzle, in air. When the voltage goes over a definite value, a rapid increase in luminosity is observed around the electrode. From there, in a time of ~ 50 ns the plasma modifies it's shape and becomes the bullet: a zone with high luminosity confined in space. The bullet then moves in the exit direction and it's expelled always with a well defined front. The round shaped bullet propagation can be seen in air until it reaches a maximum travel distance and then luminosity decreases rapidly. In these measurements conditions plasma forms again in correspondence of the negative tension peak, but it is a rapid process without propagation.

Electrode voltage and bullet intensity The time interval where there is the bullet can be defined as where it is possible to see a definite zone with mean luminosity higher than the background. The starting time is given by voltage reaching a certain value, and the bullet expires when it's luminosity decreases.

The average intensity value inside the bullet and the voltage measurement in the intersted time interval are presented in figure 3.12. Plasma formation is observed around 120.93 ns after peak start, at a tension

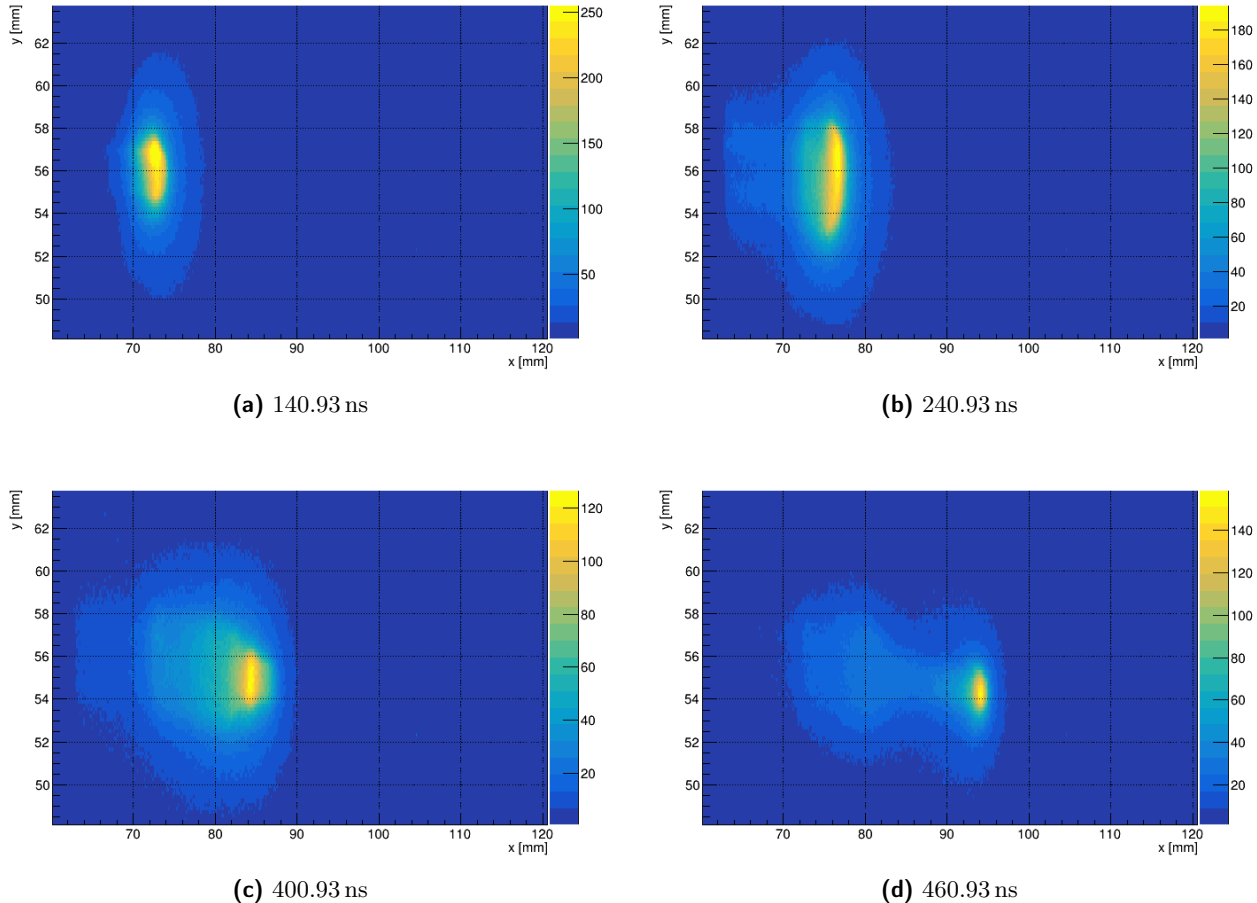


Figure 3.8: Four phases of plasma dynamics: bullet formation (a), bullet displacement inside the nozzle (b), bullet expulsion (c) and bullet propagation outside the nozzle (d). Time intervals are calculated from the start of the voltage peak.

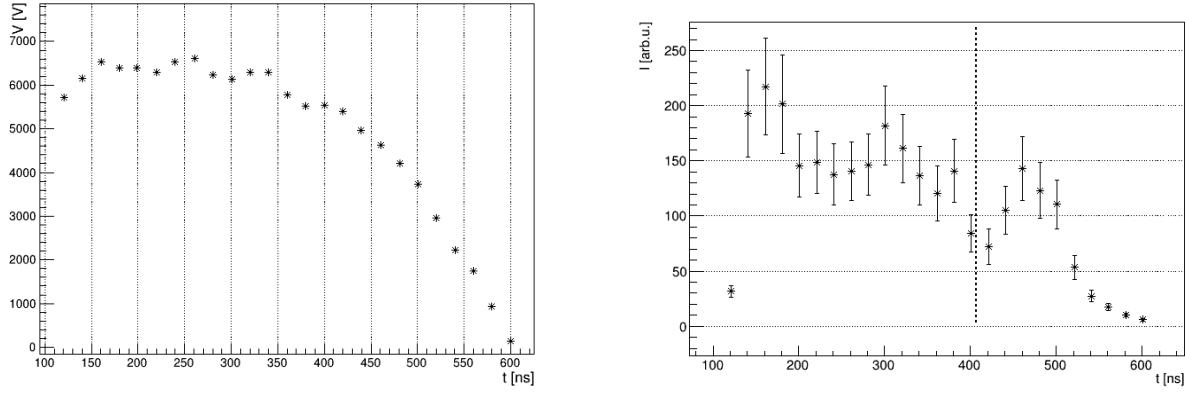


Figure 3.9: Voltage waveform and intensity of the bullet versus time, measurements setup A with voltage peak of 6.6 kV. Time zero is the start of the voltage peak, ending time is taken as the time where intensity reaches background value. The dashed line for intensity indicates when the bullet reaches the end of the nozzle.

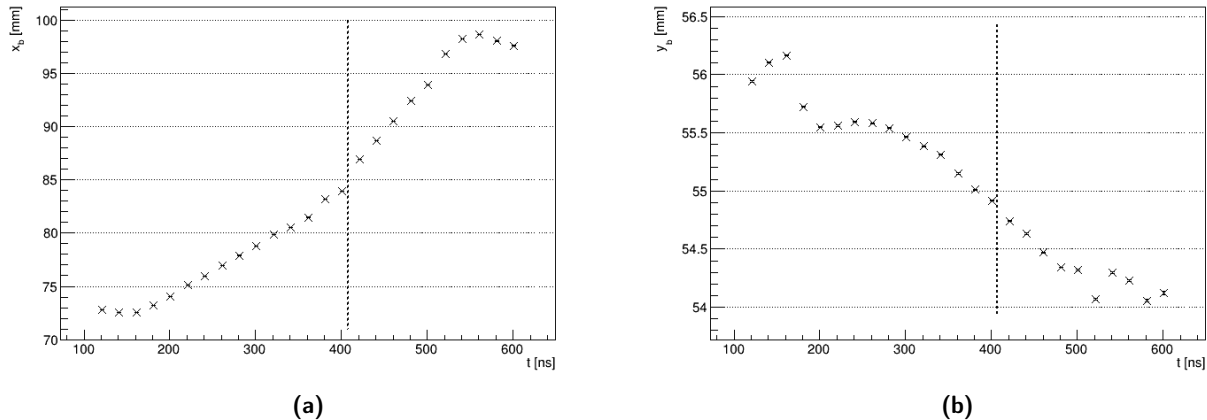


Figure 3.10: Barycenter coordinates of the bullet for measurements setup A with voltage peak of 6.6 kV. Pointed lines indicate the end of the nozzle.

value of 5710.00 ± 285.50 V. Luminosity is higher during plasma formation around the electrode and it decrease very little during all the propagation, even after the expulsion in air (pointed line on the graph). After a time of 440 ns the bullet luminosity decreases rapidly and it disperses in the air.

Barycenter coordinates and direction The motion of the bullet on observing plane can be extrapolated from its barycenter coordinates.

In figure ?? there are the two coordinates for different times. Coordinate x, along the axis of the source is more relevant to observe bullet expulsion. Plasma forms around position 73 mm and the nozzle ends at 85 mm, compatible with the distance described before. Plasma bullet moves in the nozzle with a certain velocity, until it reaches the exit and propagates in the air more rapidly. In air the bullet travels until it reaches a maximum x, covering a distance of 26.08 ± 0.02 mm from the electrode. The bullet stops before its luminosity reaches the minimum value.

Coordinate y it's relevant to show bullet direction. From figure it is possible to see that it moves in a space interval of 2 mm. The bullet forms over the electrode, then it enlarges to cover all the nozzle diameter and lowers it's barycenter with a constant slope, even after the expulsion. Once the bullet starts to decrease in luminosity, it stops its motion also on the y direction.

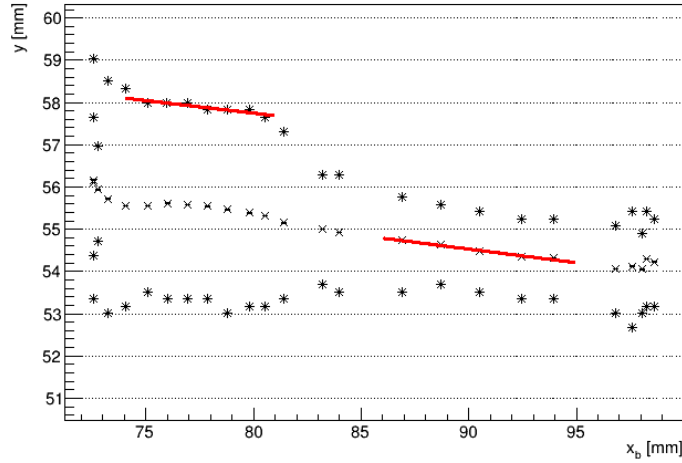


Figure 3.11: Countour of the bullet in y direction as a function of barycenter coordinate x, for measurements setup A with voltage peak of 6.6 kV. For each x value is possible to see y maximum, y minimum and y barycenter of the bullet. There are two linear fits to compare the inclination of the source (first linear fit of y maximum inside the nozzle) with the inclination of bullet propagation direction in air (second linear fit of y barycenter).

Baricenter motion in the y direction it's explainable by a tilt in the source, that is not perfectly perpendicular to the optical bench. In figure ?? there is the countour of the bullet in the y direction in function of the x brycenter coordinate, is possible to see that the figure is inclined. Inside the nozzle y maximum is the value that defines the contour of the nozzle, the angle of inclination is given by a linear fit as in figure and it is $3.39 \pm 0.10^\circ$. Outside the nozzle the barycenter direction is inclined at an angle of $3.71 \pm 0.04^\circ$. The values are almost compatible with each other, so it seems that tilting the source it is possible to direct the bullet even after its propagation in air.

Bullet dimensions Once the contour of the bullet is defined, it is simple to evaluate its dimensions along x and y directions, in figure ?? are presented the results for each time. . In the x direction, the bullet presents constant diameter until it approaches nozzle exit, where it enlarges to reach the exit. In air the bullet mantaines its dimension, with lower values then inside the nozzle, but compatible within the error. When it stops the measure loses significance as the bullet loses luminosity and it is not distinguishable from the background. In y direction there is a constant value of 4.65 ± 0.20 mm during propagation in the nozzle, as expected because the bullet covers all the nozzle area. Once the nozzle shrinks, the bullet diminish it's diameter and maintains a constant value of 2.07 ± 0.20 mm during all the propagation in air.

Bullet velocity From barycenter graphs it is possible to estimate the bullet velocity at different times. With a linear fit of the x barycenter inside the nozzle, as shown in figure 3.13, bullet velocity is found to be $v_N = 46.48 \pm 0.20$ km/s. Once it exits the nozzle the speed goes up, until a value of $v_A = 95.16 \pm 0.60$ km/s.

Velocity for each time can be calculated with a 3 point finite difference formula (that excludes the first and the last point), finding the values shown in figure 3.13. The average velocity value inside the nozzle and in air is compatible with the result from the linear fit: $v_N = 48.23 \pm 1.03$ km/s and $v_A = 95.16 \pm 1.82$ km/s.

It's interesting to point out that those velocities are much higher then the average velocity of the neutral gas: for a flow of 2 L/min it is of 12 m/s.

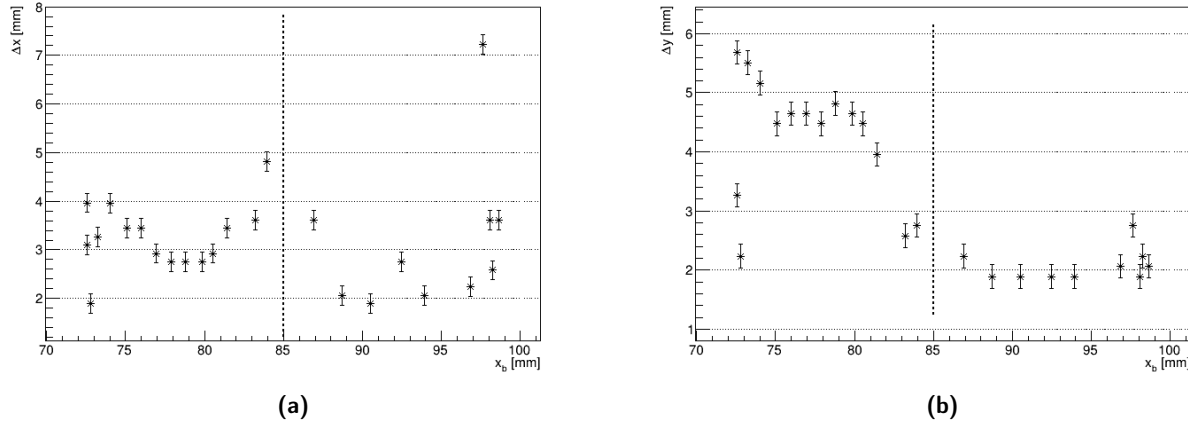


Figure 3.12: Dimensions of the bullet for measurements setup A with voltage peak of 6.6 kV. Pointed lines indicate the end of the nozzle.

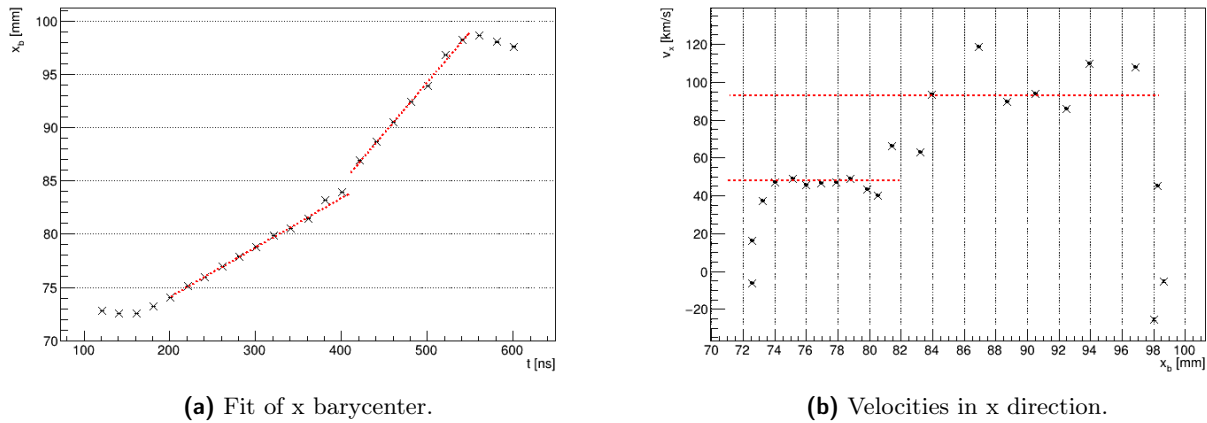


Figure 3.13: Velocity of the bullet in x direction for measurements setup A with voltage peak of 6.6 kV. In (a) linear fit of barycenter position as function of time inside the nozzle and in air; in (b) velocities evaluated for each time with a three point difference formula, where dashed lines indicate average values inside the nozzle and in air.

V_p [kV]	V_0 [kV]	x_{dist} [mm]	y_{dist} [mm]	v_N [km/s]	v_A [km/s]
5.66 ± 0.30	5.55 ± 0.28	15.99 ± 0.01	1.66 ± 0.02	37.72 ± 0.04	-
6.59 ± 0.33	5.71 ± 0.29	26.08 ± 0.02	1.92 ± 0.04	46.48 ± 0.02	95.16 ± 0.06
7.22 ± 0.36	6.01 ± 0.30	34.55 ± 0.05	2.07 ± 0.01	59.80 ± 0.03	149.47 ± 0.09

Table 3.2: Result of the analysis for measurements setup A. V_p is the voltage peak value, V_0 is the voltage value at plasma formation time, x_{dist} and y_{dist} are the highest distances reached by the bullet from electrode position, v_N is the velocity in x direction reached inside the nozzle, v_A is the velocity of propagation in air in x direction.

3.2.2 Voltage influence

An increase in trigger width Δt correspond to an increase in voltage peak values (see chapter 2) and an increase in electric field intensity. The voltage peak value could change bullet formation and propagation. The results of the analysis for setup A with different voltage values are in figure 3.14 and table 3.3.

The discharge starts always in the same voltage interval, around 5.7 kV. At an higher voltage corresponds an higher luminosity, but the time interval where luminosity decreases is always around 100 ns once it exits the nozzle (figure 3.14 (a)).

The plot for the barycenter coordinates (figure 3.14 (b) - (c)) shows that higher voltage corresponds to further distances reached by the bullet (x_{dist} and y_{dist} in table). For the lower voltage peak the bullet doesn't even propagate in air, as it stops right after nozzle exit.

Dimensions of the bullet (figure 3.14 (d) - (e)) are not influenced by voltage value, they have the exact same behaviour for every measurements set. A single notable difference it's in the y diameter inside the nozzle, where for higher voltage there are slightly larger values. However inside the nozzle there are refraction effects due to the glass, the increase is compatible with the variation in dimensions that could be given by higher luminosity.

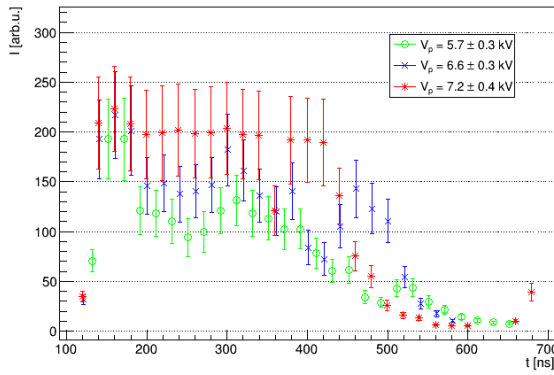
Velocity values (figure 3.14 (f)) show how the bullet behaviour is costant during the propagation inside the nozzle and becomes more erratic once it exits. As mentioned before, for the lowest voltage value the bullet stops right after it exits the nozzle, in this configuration it's not possible to find a propagation velocity in air. For other sets velocity has the same profile, with a proportionality between peak voltage value and velocity value: increasing voltage velocity goes from $v_A = 92.93 \pm 0.06$ km/s to $v_A = 149.47 \pm 0.09$ km/s.

3.2.3 Flow influence

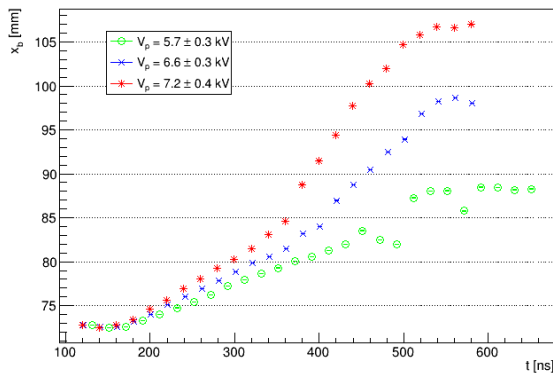
As said before, neutral gas velocity is low if compared to bullet speed, however it could influence the overall dynamic of bullet propagation. Setup A, B, C and D correspond to four different flows with the same peak voltage. In figure 3.15 and table ?? are presented the results of the analysis.

Also for this parameter, the discharge starts always in the same voltage interval, for values higher then 5.7 kV. For gas flows of 1 and 2 L/min bullet luminosity decreases in a time interval around 100 ns once it exits the nozzle. For flows > 2 L/min it has luminosity clearly stronger then background for a longer time interval, around 200 ns (figure 3.15 (a)).

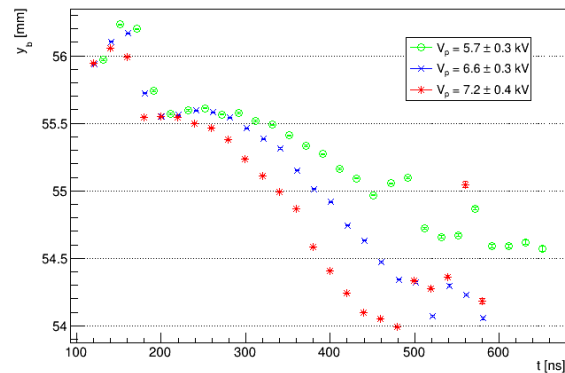
From the barycenter coordinates (figure 3.15 (b) - (c)) can be seen that more gas flow is correlated with lower mobility of the bullet: it propagates for shorter distances when there are higher flows. For maximum flow, even if bullet luminosity is comparable to the other measurements, the bullet travels a short distance from the exit of the nozzle and its barycenter stays in the same position until bullet luminosity reaches background value.



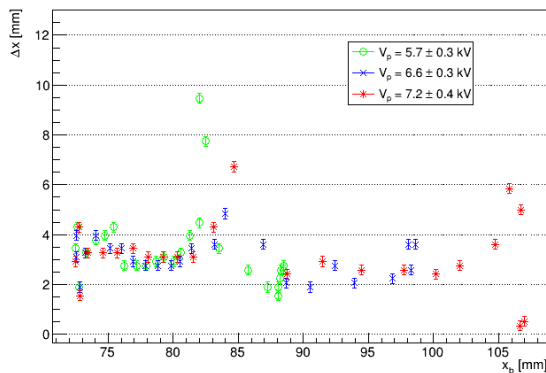
(a) Mean luminosity.



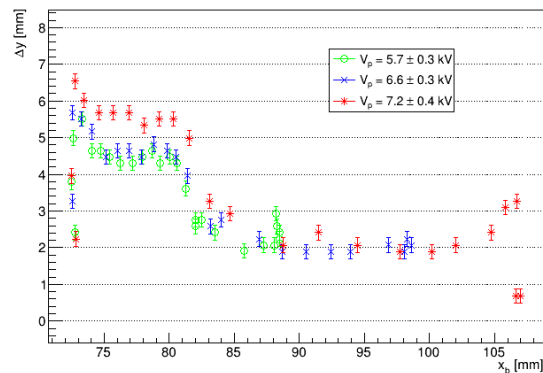
(b) x barycenter.



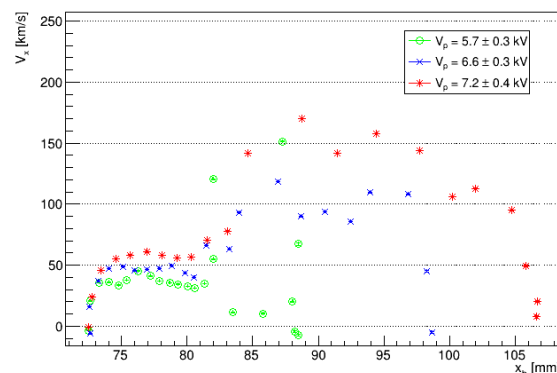
(c) y barycenter.



(d) x diameter.



(e) y diameter.



(f) x velocity.

Figure 3.14: Results of the analysis for setup A (helium flow of 2 L/min without target), with different peak voltage values.

Flow [L/min]	V_0 [kV]	x_{dist} [mm]	y_{dist} [mm]	v_N [km/s]	v_A [km/s]
1	5.87 ± 0.08	30.65 ± 0.03	2.75 ± 0.01	54.33 ± 0.10	113.97 ± 0.09
2	5.71 ± 0.29	26.08 ± 0.02	1.92 ± 0.04	46.48 ± 0.02	95.16 ± 0.06
3	5.41 ± 0.27	19.38 ± 0.01	1.84 ± 0.01	39.88 ± 0.04	80.96 ± 0.30
4	5.90 ± 0.12	22.80 ± 0.03	2.30 ± 0.01	58.89 ± 0.14	41.94 ± 0.44

Table 3.3: Results of the analysis for setup A, B, C and D: different gas flow, voltage peak value of 5.7 kV, without target. V_0 is the voltage value at plasma formation time, x_{dist} and y_{dist} are the highest distances reached by the bullet from electrode position, v_N is the average velocity in x direction inside the nozzle, v_A is the average velocity of propagation in air in x direction.

Q [L/min]	$v_{N,\text{min}}$ [km/s]	x_{air} [mm]	Rn
1	48.46	78.78	36.88
2	40.09	80.55	73.77
3	33.74	81.75	110.65
4	17.01	81.28	147.54

Table 3.4: Bullet propagation parameters inside the nozzle for different neutral gas flow. v_N is the lowest velocity reached inside the nozzle; x_{air} is the position where the bullet increases velocity, thought to be where the bullet meets the air outside the nozzle; Rn is the Reynold number associated to the gas flow.

The study of bullet's velocity can give more insight to the phenomenology of bullet propagation, it is shown in figure ?? (e), with higher detail for values inside the nozzle in figure ?? (f). Bullet's velocity always decreases moving inside the nozzle, until it reaches a certain distance. The deceleration inside the nozzle is more evident with higher flow, especially when the flow is higher than 3 L/min (as we can see also in [47]). The distance at which the bullet speeds up is different for different flows as can be seen in table 3.4. Once the bullet exits from the nozzle, its velocity decreases more rapidly with higher gas flow.

The different behavior of the bullet with different neutral gas flow could be related to the variation of the Reynold number of the fluid, that could assume critical values. Following the study in [50] the Reynold number with different flow can be evaluated as in equation 3.1, where v is the gas velocity found from the gas flow value Q , ρ is helium density, μ is helium viscosity and D is the nozzle diameter.

$$\text{Rn} = \frac{v\rho D}{\mu} = \frac{Q}{\pi(D/2)^2} \frac{\rho D}{\mu} \quad (3.1)$$

Resulting values are presented in table 3.4, always below critical Reynold number (> 2000), there is not transition from laminar to turbulent flow for changes on neutral gas flow from 1 to 4 L/min.

While the bullet propagates inside the nozzle, at a certain time it meets the air outside, changing the elements that participate in ionization reactions from helium to those found in air. The bullet decelerate inside the nozzle and accelerate when it meets air ([47]). The change in bullet velocity when there is an increase in neutral gas velocity could be related to the different transition time and position from helium to air. With a higher flow the bullet travels in a gas of almost only helium for longer time and its velocity decreases more, leading to a different dynamic during propagation in air.

3.2.4 Insulating target

The electric field created by the electrode is not expected to change if there is an insulating target in front of the nozzle. An interesting effect is seen after the bullet impacts on the target, as shown in

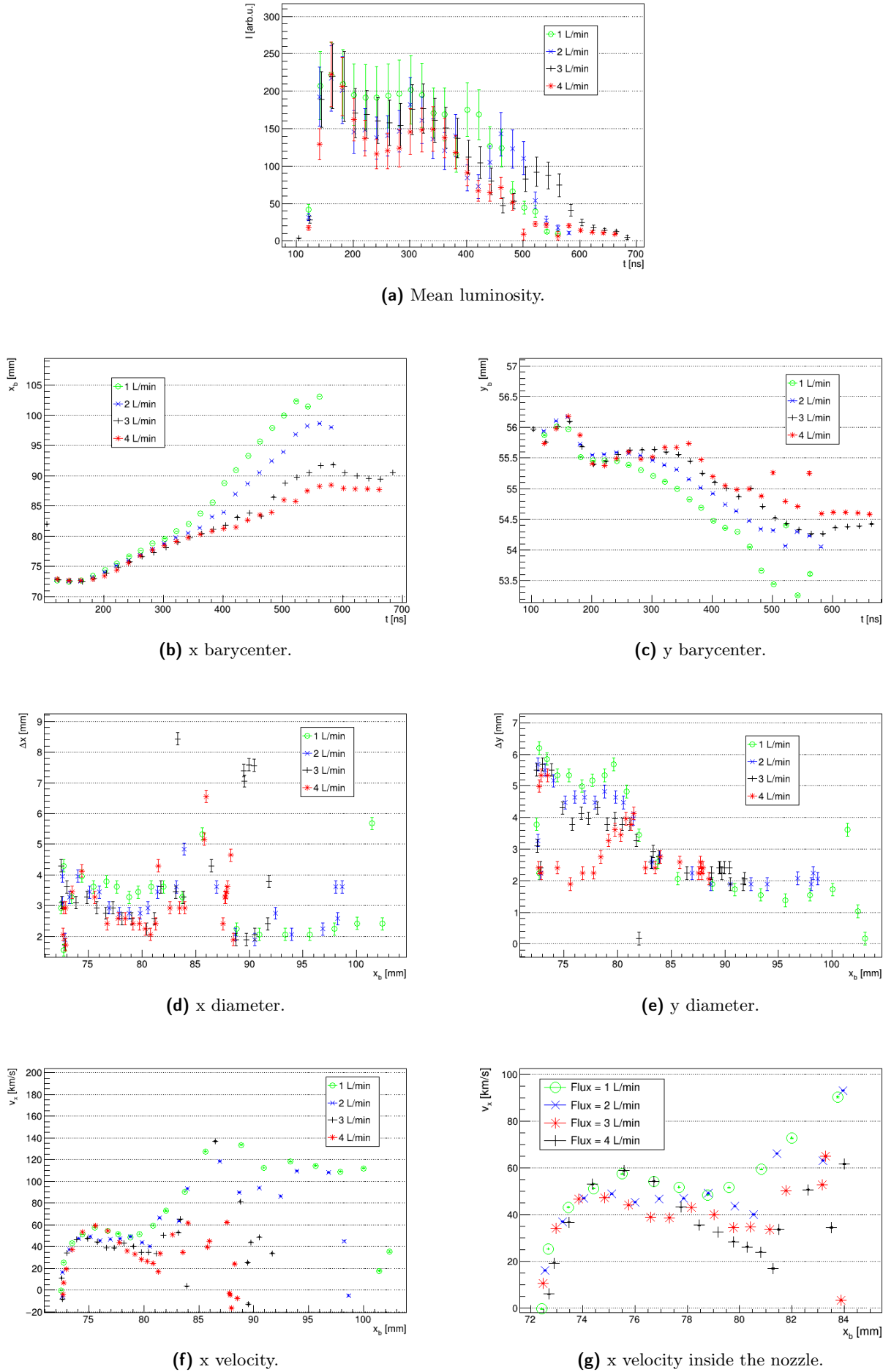
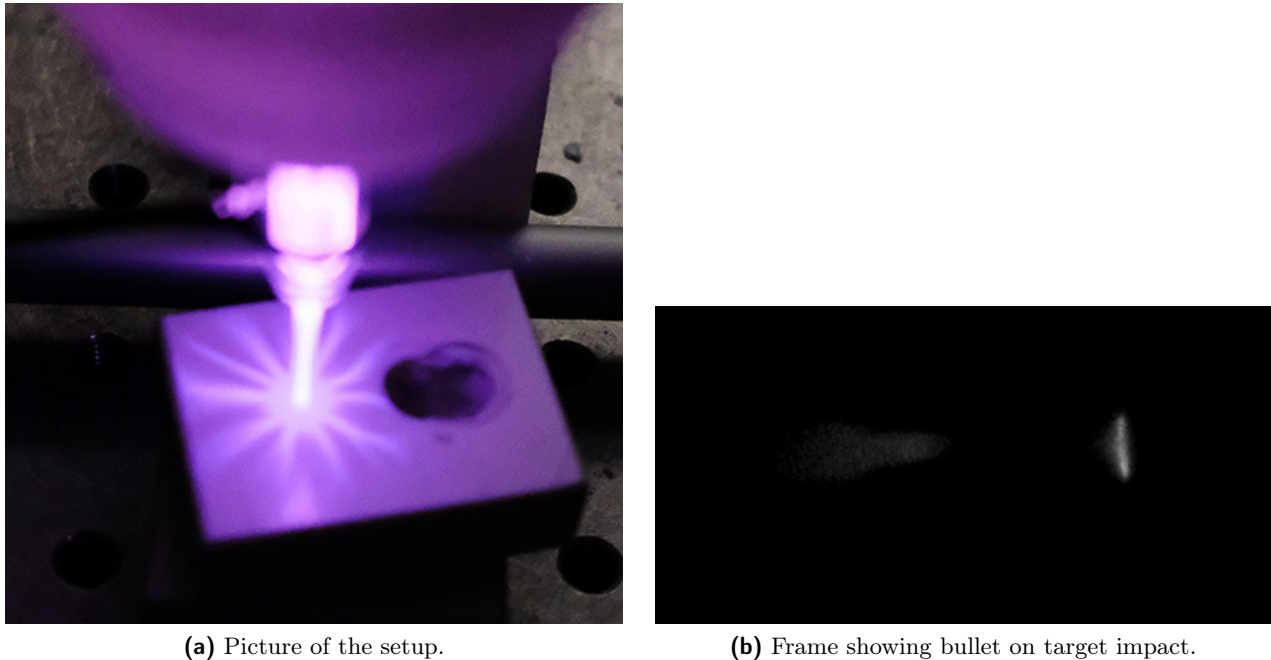


Figure 3.15: Results of the analysis for setup A, B, C and D: different gas flow, voltage peak value of 5.7 kV, without target.



(a) Picture of the setup.

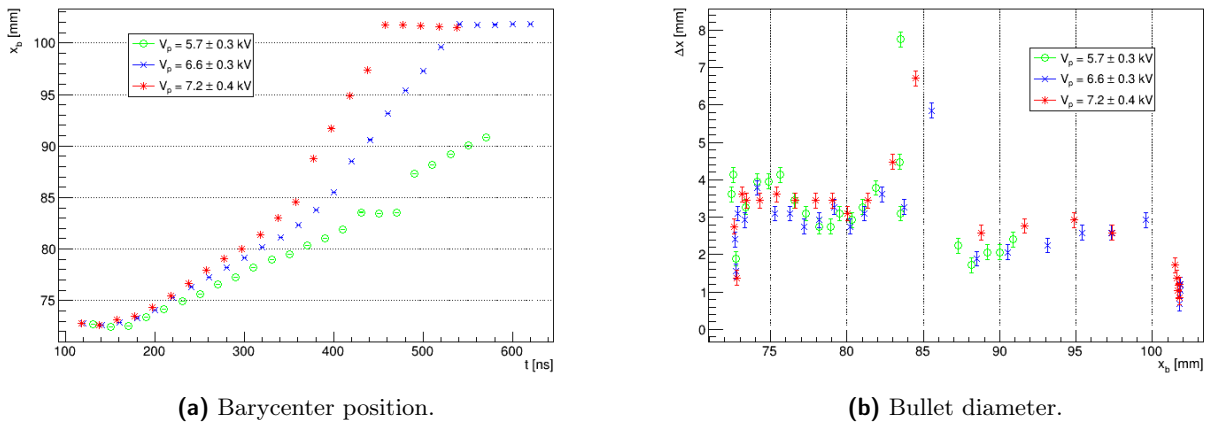
(b) Frame showing bullet on target impact.

Figure 3.16: Impact of plasma on an insulating target. In (a) picture of the plume, in (b) frame acquisited for setup E, voltage peak 7.2kV.

figure 3.32: plasma forms a round shaped figure on the insulator that enlarges on the target until the luminosity decreases.

Barycenter x coordinate of the bullet and its diameter are presented in figure 3.17. While for the lowest tension value the bullet stops before it reaches the target, for the other two sets it clearly stops at the target position. Distance values are comparable with those without target (figure 3.14), higher for medium voltage value. Bullet width is exactly the same with or without target, it shows differences only when it impacts on the target and shrinks rapidly. Displacement velocities inside the nozzle and propagation velocities in air are of the same order of values without target, shown figure ???. There is higher v_A only for medium tension value, where it reaches 118.98 ± 0.07 km/s, due to the rapid collision with the target instead of slowing down and stopping.

Charge deposition Once the bullet reaches the target it is possible to see how the glowing region enlarges on its surface and the bullet diameter increases, as shown in figure 3.18. Is possible to



(a) Barycenter position.

(b) Bullet diameter.

Figure 3.17: Barycenter motion and diameter in x direction for measurements setup E (presence of insulating target) for different voltage peak values.

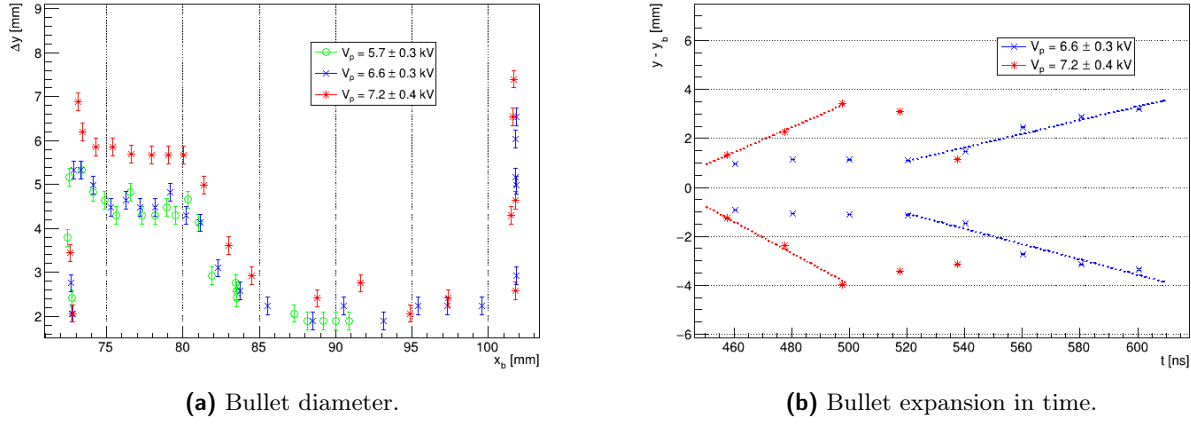


Figure 3.18: Charge deposition in y direction on an insulating target, for measurements setup E. In (a) there is the absolute value for the diameter for all barycenter positions; in (b) the expansion of y contour after it reaches the target for medium and high voltage peak value. Contour values are calculated as difference with the barycenter y coordinate, linear fits show how much the diameter enlarges in time.

evaluate the expansion diameter and velocity observing bullet contour in the y direction once the bullet reaches the target. In figure 3.18 can be seen that the diameter and the expansion velocity are higher for higher voltage value: for a voltage peak of 6.6 kV the shape on the insulator has a maximum diameter of 6.54 ± 0.04 mm and an expansion velocity of 31.36 ± 0.25 km/s; for 7.2 kV the values are 7.40 ± 0.02 mm and 64.04 ± 0.39 km/s.

3.2.5 Conductive target

A grounded conductive target could influence bullet propagation because it fixes the value of the electric field on that point in space and it presents free charges on its surface. In measurements setup F and G a conductive target is positioned in two different positions.

For measurement setup F a conductive target is positioned at 24 mm from the bench, corresponding to 30 mm from the electrode.

When the bullet impacts on the conductive target can be observed a rapid increase in luminosity on the target and in the space between nozzle and target as shown in figure 3.19. In this work it will be referred as “backstream” (because it seems to have motion inverse to that of the bullet). Analysis of bullet propagation, impact and evolution on target is treated separately from analysis of backstream, to allow comparison with other measurements setup.

Bullet dynamics Bullet propagation is different if compared to measurements without conductive target. From figure 3.20 is possible to see that bullet luminosity presents an increase in correspondence of the second voltage peak (negative). This results in an increase of bullet lifetime up to 900 ns from the first voltage peak.

Barycenter motions shows that even with low voltage the bullet reaches the target, different from the behavior with the insulating target. Propagation velocity is higher than values found in other configurations. Bullet diameter doesn't show different behaviour, it stays constant until nozzle exit and remains constant until it reaches the target and shrinks to a point. As said before, velocities of propagation in air are generally larger than without target, they arrive from 112.04 ± 0.05 km/s for low voltage peak to 160.55 ± 0.09 km/s for high voltage peak.

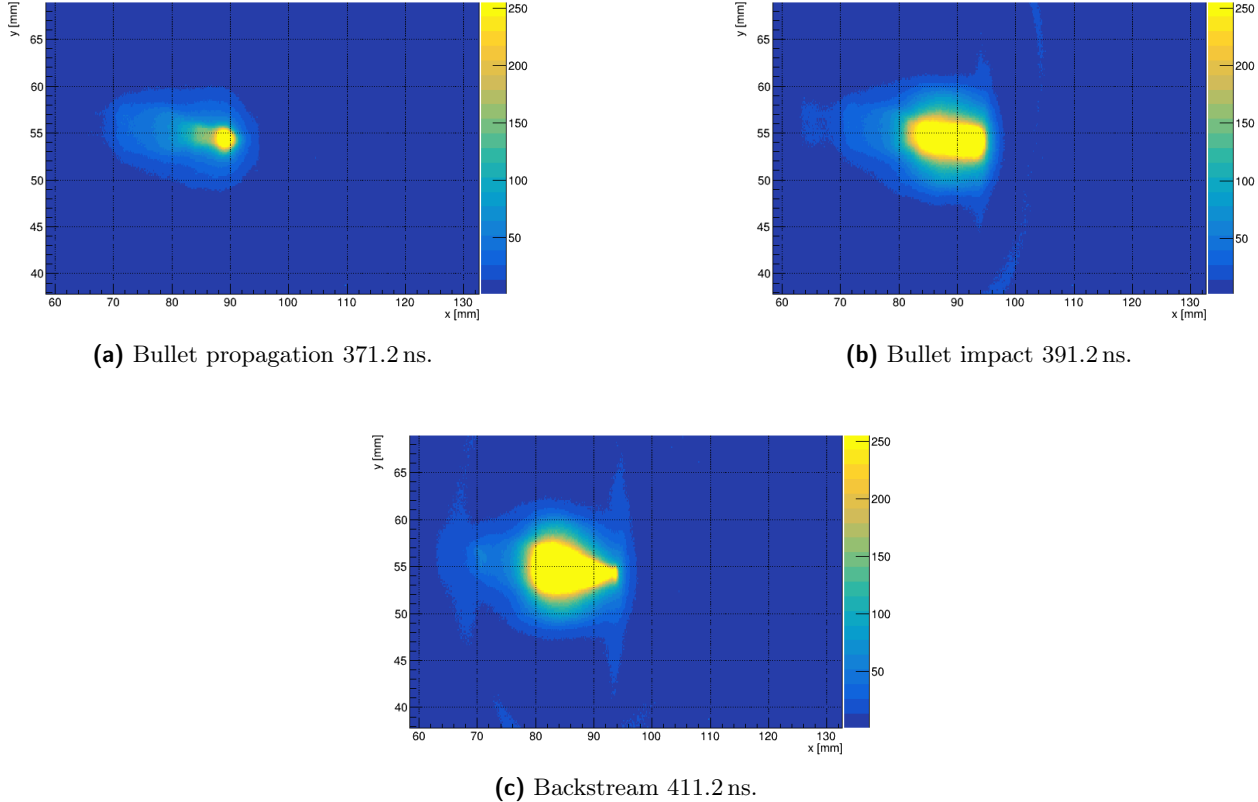


Figure 3.19: Example of frames showing impact on a conductive target and consequent backstream, measurements setup F with voltage peak value 7.2 kV.

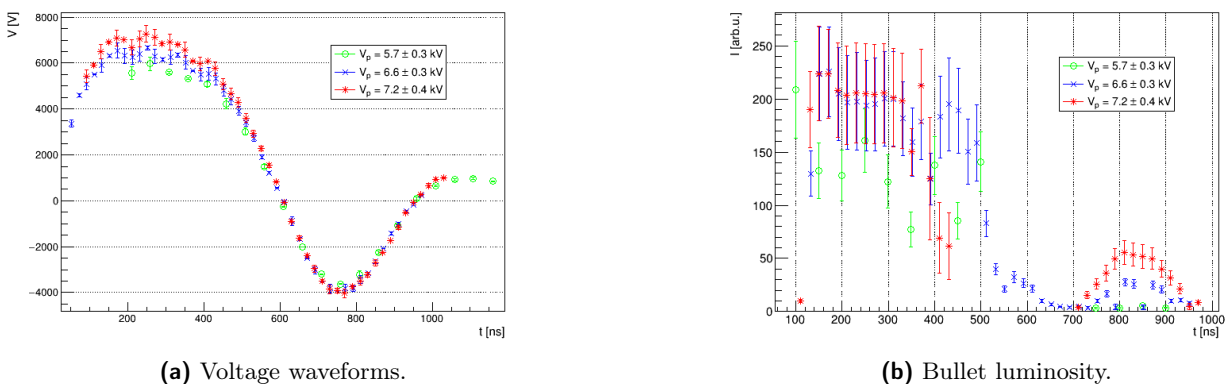


Figure 3.20: Voltage on the electrode and bullet luminosity for measurements setup F, different peak voltage values. Note the second luminosity peak in correspondence of the negative voltage peak.

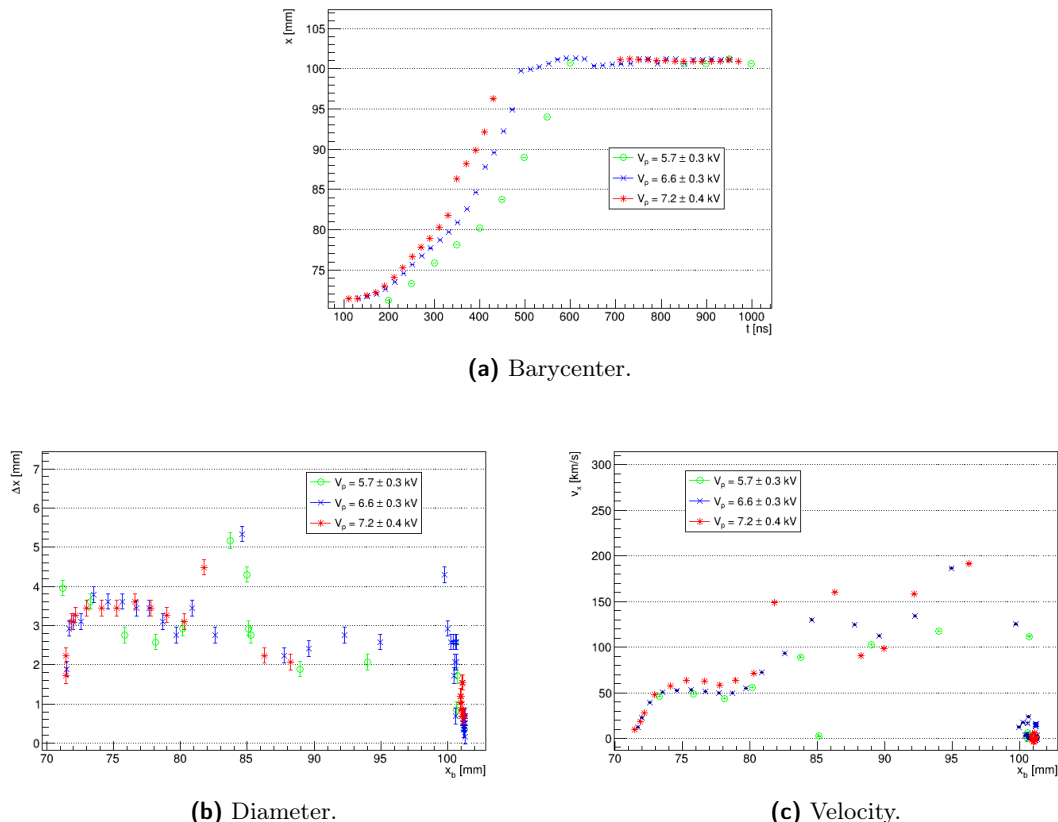


Figure 3.21: Bullet barycenter coordinate, diameter and velocity along x direction, for measurement setup F and for different peak voltage values. Can be seen as the bullet reaches the target, it shrinks and stops.

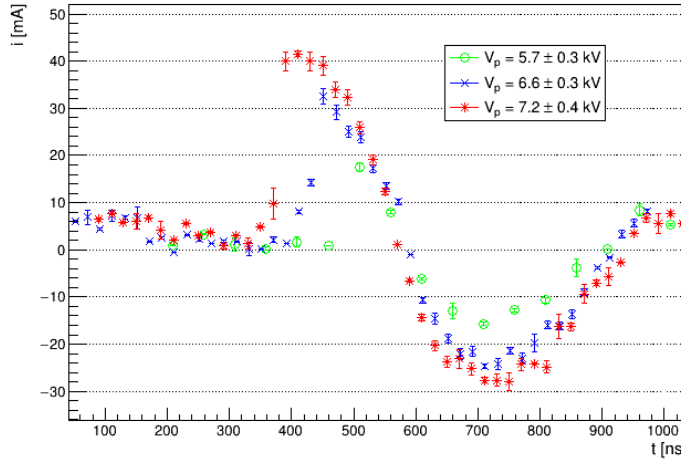


Figure 3.22: Current intensity for measurements setup F, for different voltage peak values.

V_p [kV]	i_p [mA]	$t_{0,i}$ [ns]	$t_{p,i}$ [ns]	t_{imp} [ns]	$x_{\text{target}} - x(t_{0,i})$ [mm]
6.6 ± 0.3	32.63 ± 1.63	391.6 ± 15.0	451.6 ± 15.0	511.6 ± 15.0	9.22 ± 0.01
7.2 ± 0.4	41.50 ± 0.62	350.3 ± 15.0	410.3 ± 15.0	450.3 ± 15.0	15.18 ± 0.02

Table 3.5: Results of the analysis of current measurements for setup F. V_p is the voltage peak for the pulse, i_p is the current peak value, $t_{0,i}$ is the starting time for the current pulse, $t_{p,i}$ is the maximum current time, t_{imp} is the time impact of bullet on target, $x_{\text{target}} - x(t_{0,i})$ is the distance between bullet position when we start to measure current and target position.

Current measurements Current intensity flowing in the conductive target due to charge transported by plasma can be measured. The correlation between bullet and charge deposition can be verified observing the relation between impact time and peak current starting time.

Current intensity it's shown in figure 3.22, it presents two peaks, a positive one and a negative one. For the lowest voltage value current peaks are not high enough to analyze them, this set is excluded from the following analysis. The positive peak value starts at time $t_{0,i}$ and reaches the maximum at time $t_{p,i}$. Both values are inversely proportional to voltage peak value, we have lower and slower current intensity when the voltage is lower. Those times can be compared with the impact time of the bullet on the target, t_{imp} , in table ?? are presented the values. It is possible to see that current starts flowing into the target before the bullet reaches the target, and even maximum current is measured before the impact time of the bullet. It's also interesting to evaluate the distance of bullet from target when we measure current, in table ?? there is the difference between bullet barycenter position and target position $x_{\text{target}} - x(t_{0,i})$.

Those results could be explained by the presence of ionized particles that does not produce reactions with emission at visible wavelengths. Current would be measured even without seeing the impact of plasma on the target if the bullet has a diameter higher than the one measurable with the camera. This invisible portion of the bullet would have the same behavior of the bullet for different voltage values, i.e. it would increase its velocity with higher voltage. As can be seen from table ?? the current peak starts indeed before with higher voltage.

Backstream Dynamics of the backstream is difficult to analyze as it's a rapid phenomenon with too high luminosity. Frames right after the impact of the bullet on target present another zone with high luminosity right after nozzle exit. This other glow has stable position and diameter, as can be seen in figure 3.23, with a slow tendency to shift towards the target when voltage is positive and towards the electrode when it's negative. The phenomenon can be explained as a very rapid charge stream

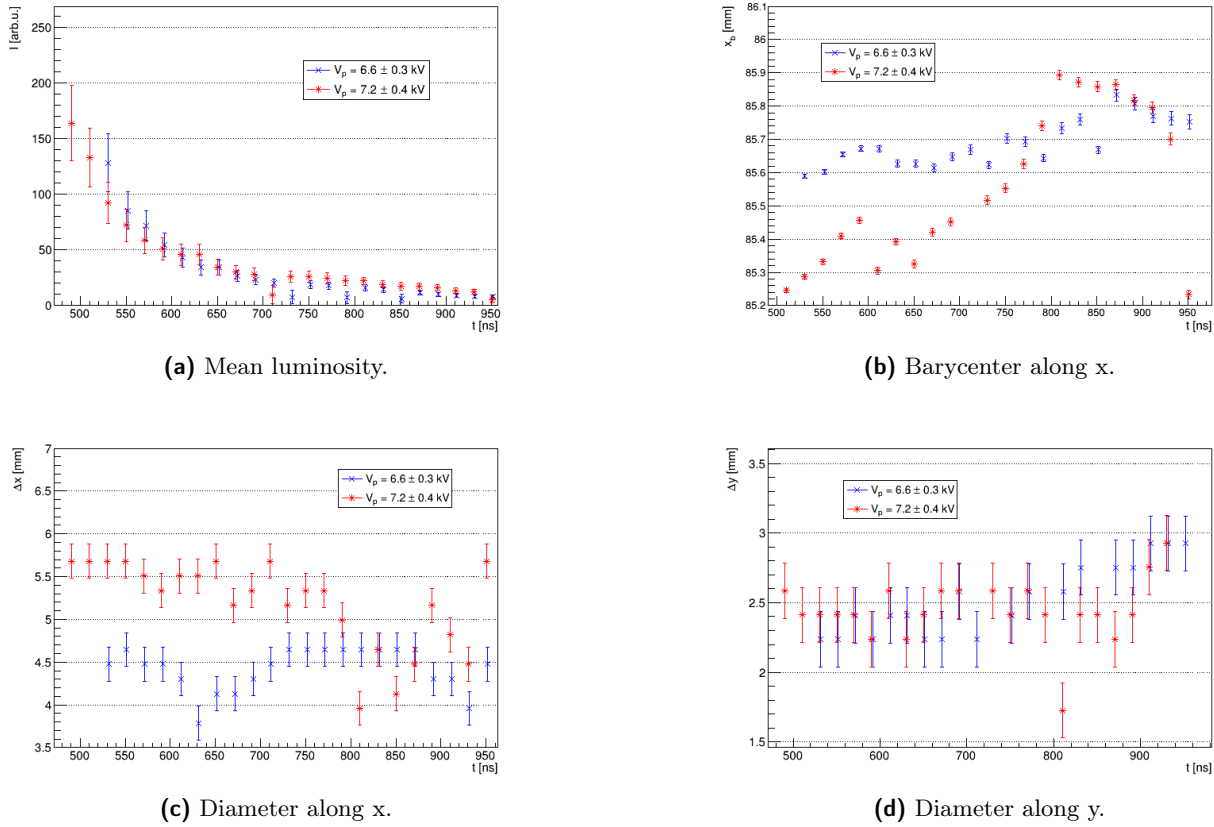


Figure 3.23: Backstream analysis for measurements setup F. It's possible to see the decreasing luminosity while the barycenter stays around the nozzle exit and diameter stays constant.

from the target to the electrode, that stops when meets the nozzle, but to study it are necessary other specific measures with more time resolution.

Position of the target

The position of the target could influence bullet propagation. In measurement setup G the conductive target is positioned at 32 mm from the bench, corresponding to 22 mm from the electrode, closer to the nozzle respect setup F.

With a conductive target this close it's more difficult to see the bullet evolution, as it is more rapid and the backstream has even higher relevance.

In figure 3.24 are presented the results of the analysis. For all the sets there is high luminosity, even after a time interval corresponding to the end of the voltage peak. For higher voltage peak values, it is not possible to see the bullet, as it reaches the target in a sort of large plume right after nozzle exit. The other two sets shows the same behaviour described before, with even higher velocities: for medium voltage velocity inside the nozzle velocity is 59.30 ± 0.05 km/s, while maximum velocity in air is 174.44 ± 0.08 km/s.

Current measurements As done with previous setup, for low and medium voltage it's possible to analyze time and space intervals between bullet barycenter motion and current measurements. Obtained values are shown in table ??.

Again current flows in target before the impact of the bullet, when it is distant from the target (parameter $x_{\text{target}} - x(t_{0,i})$ in table). Comparing these values with results for setup F, is possible to see

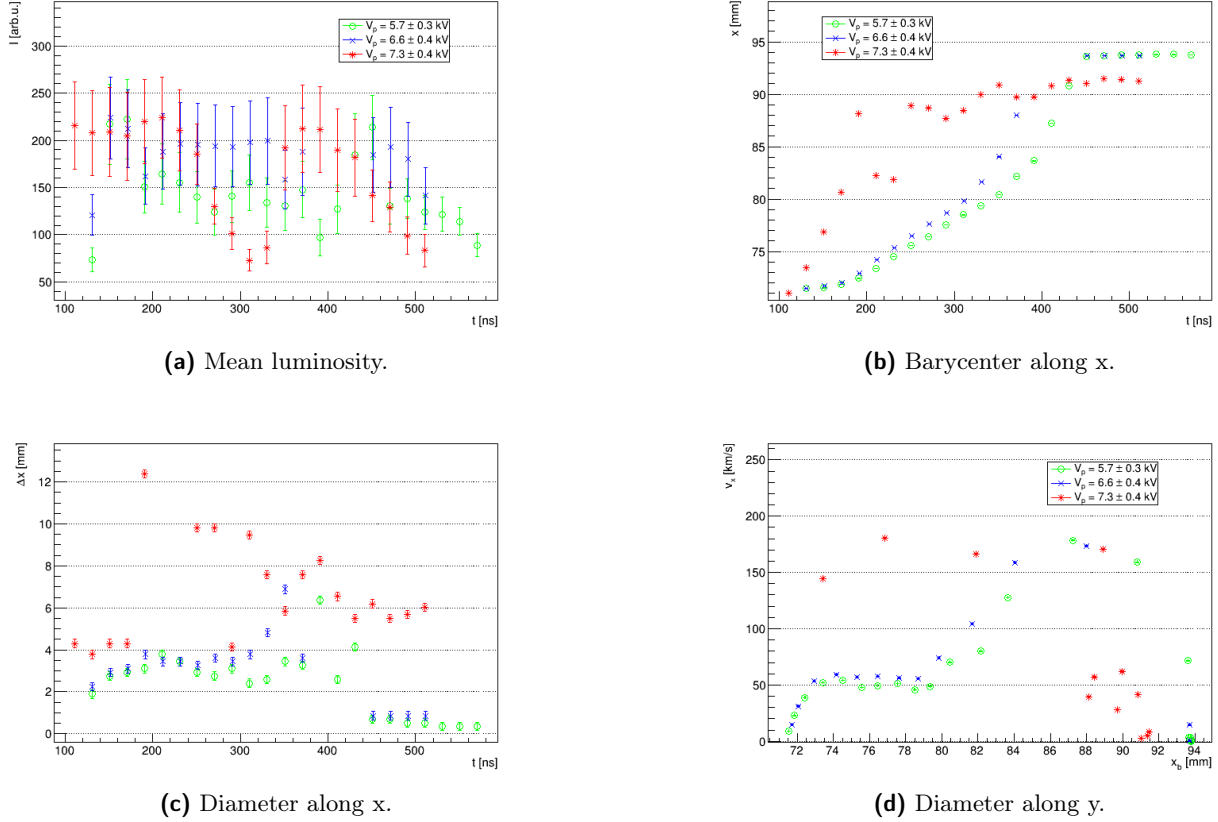


Figure 3.24: Analysis of measurement setup G: conductive target positioned close to the nozzle.

V_p [kV]	i_p [mA]	$t_{0,i}$ [ns]	$t_{p,i}$ [ns]	t_{imp} [ns]	$x_{\text{target}} - x(t_{0,i})$ [mm]
5.7 ± 0.3	47.41 ± 2.37	370.6 ± 15.0	450.6 ± 15.0	450.6 ± 15.0	11.34 ± 0.02
6.6 ± 0.4	77.41 ± 3.87	311.2 ± 15.0	411.2 ± 15.0	391.2 ± 15.0	13.61 ± 0.04

Table 3.6: Values extrapolated from current measurements and bullet barycenter motion for setup G. V_p is the voltage peak for the pulse, i_p is the current peak value, $t_{0,i}$ is the starting time for the current value, $t_{p,i}$ is the time of current peak value, t_{imp} is the time of the impact of bullet on target, $x_{\text{target}} - x(t_{0,i})$ is the distance between bullet position when current peak starts and target position.

V_p [kV]	V_0 [kV]	x_{dist} [mm]	v_N [km/s]	v_A [km/s]
4.81 ± 0.24	4.81 ± 0.24	18.13 ± 0.05	34.59 ± 0.03	43.19 ± 0.07
5.33 ± 0.27	5.20 ± 0.26	22.42 ± 0.06	42.82 ± 0.04	61.17 ± 0.05
6.05 ± 0.30	5.16 ± 0.26	26.60 ± 0.09	62.92 ± 0.05	160.32 ± 0.07

Table 3.7: Results of the analysis for measurements setup A with neon, for different voltage peak values. V_p is the peak value for the pulse, V_0 bullet formation tension, x_{dist} is the highest distances reached by the bullet from electrode position, v_N is the velocity in x direction reached inside the nozzle, v_A is the velocity of propagation in air.

that for the same voltage peak value, the current peak starts faster and reaches an higher peak value. Hypotizing that charge motion is correlated to bullet motion an earlier impact point means that the bullet will lose less charge during the propagation in air and that there will be higher current intensity flowing on target.

3.3 Neon flow

The second noble gas used to produce cold plasma is neon, the one with more emission intensity at visible wavelength. Neon it's an element with standard atomic weight of 20.180, 1st ionization energy of 21.565 eV and 2nd ionization energy of 40.963 eV and several lines with wavelength in visible spectrum. It's easy to produce neon plasma, when the voltage pulse is applied, even with low repetition rates, the gas presents high luminosity in a wide space. This emissivity it's the reason why neon is commonly used to build neon lamps.

The working pulse repetition rate is set to $f = 1 \text{ kHz}$ and three opening times equivalent to low, medium and high voltage in helium. Different measurement setup are presented in table 3.1.

3.3.1 Free bullet

First measurements are done to see plasma dynamics without a target, changing between low, medium and high tension peak value. Results are shown in figure 3.25 and table 3.7. First thing to notice is that plasma is produced not specifically at electrode's end where the electric field should be higher, as in helium, but a little before, with lower luminosity. Luminosity evolution from there is similar to that of helium bullet, but there is a residual luminosity tail that lasts longer. Barycenter motion and diameter evolution present the same evolution of helium bullets inside the nozzle. Outside the nozzle there are two main differences:

- neon bullets come out of the nozzle more difficultly and lose velocity more rapidly, covering shortest distances. Propagation velocity in air rises exiting the nozzle (until $160.32 \pm 0.07 \text{ km/s}$ with high voltage), but goes down abruptly and the bullet slows down rapidly.
- neon bullet's x diameter rises increasing voltage. As can be seen from figure ??, diameter evolution is the same as in helium bullet, but there are higher diameter values with higher voltage.

Those differences can be explained by the different reactions that have place in neon plasma. If those reactions need less energetic electrons, we would have more of them that partecipates, increasing the diameter of the bullet.

For both helium and neon inside the nozzle there is bullet propagation, it is possible to compare how the velocity v_N changes varying voltage peak value for the gasses. In figure 3.26 there is the plot for the two gasses. With few points it's not possible to extrapolate accurately the behavior, but a linear plot shows that helium bullet's velocity grows with a slope of $14.55 \pm 2.40 \text{ km/s/kV}$, while neon

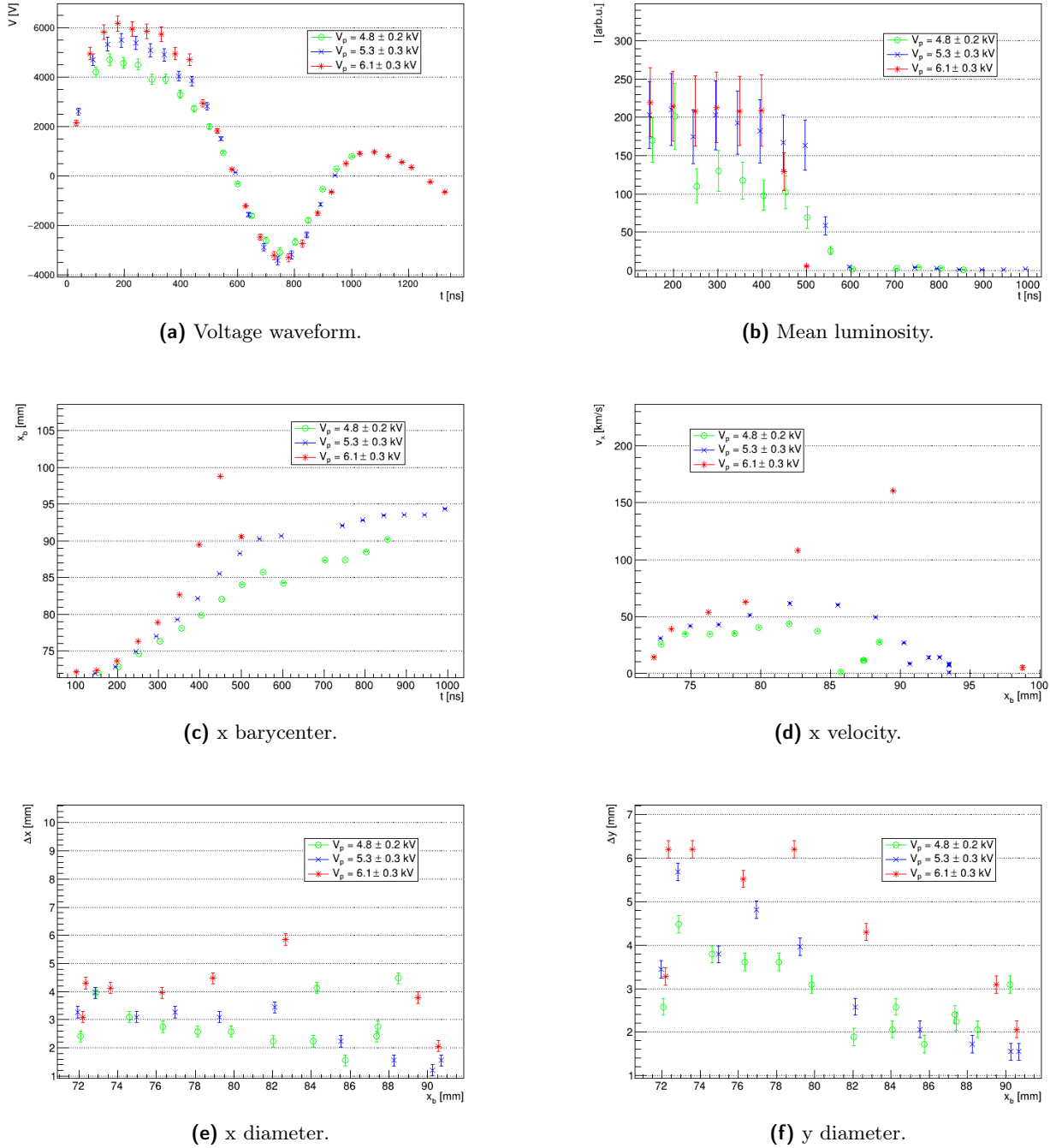


Figure 3.25: Results of the analysis for measurement setup A with neon gas, for different peak voltage values.

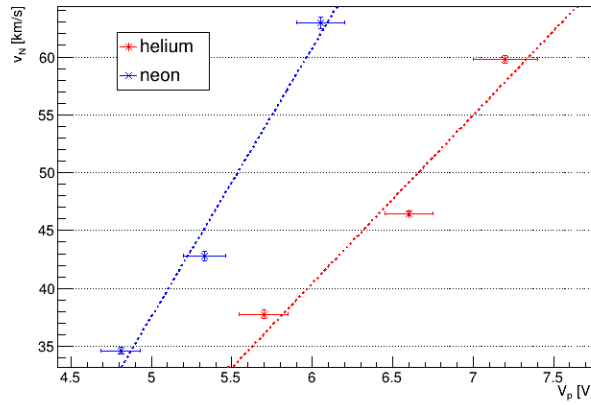


Figure 3.26: Bullet velocity inside the nozzle as a function of voltage peak value, for helium and neon.

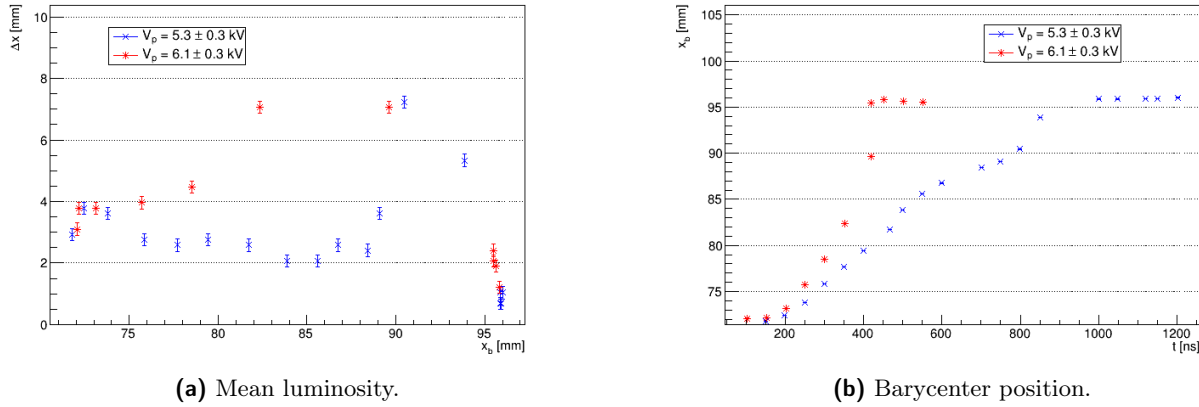


Figure 3.27: Mean luminosity and barycenter motion for neon gas in setup measurement D.

bullet's velocity has a slope of 23.23 ± 3.66 km/s/kV. Those values are of the same magnitude, but not compatible, suggesting that bullet's velocity may depend from gas composition.

3.3.2 Insulating target

Also for neon is studied the dynamic with an insulating target positioned at 30 mm from the electrode, in measurement setup B. Results are similar with helium or neon bullets: plasma forms near the electrode, exits from the nozzle and the impact on the target produce a round shaped figure on it, as in figure 3.32. Also in neon for low voltage peak value the bullet doesn't reaches the target, as the maximum distance travelled is lower then target distance. This suggests that the target does not influences the bullet when it is not in its proximity. A peculiarity with neon is that there is a second, very low, peak in luminosity corresponding to the second voltage peak of the pulse.

The figure that bullet impact produces on target can be analyzed as with helium. In figure 3.28 there is the y contour in function of time and is possible to extrapolate an expansion velocity of 5.01 ± 0.29 km/s for medium voltage and 30.76 ± 0.25 km/s for high voltage. They are both lower compared to helium, probably because the bullet in neon slows down more rapidly once it's outside the nozzle.

3.3.3 Conductive target

As with helium, a conductive target has an influence in all neon bullet's dynamics. If compared to helium the bullet goes more rapidly from a round shape to the elongated one that gives rise to the

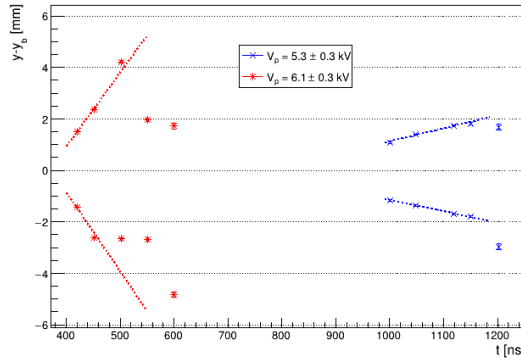


Figure 3.28: Neon plasma expansion on insulator target, measurements setup B for different voltage peak values.

Δx_{targ} [mm]	V_p [kV]	i_p [mA]	$t_{0,i}$ [ns]	$t_{p,i}$ [ns]	t_{imp} [ns]	$x_{\text{target}} - x(t_{0,i})$ [mm]
30	6.05 ± 0.30	6.87 ± 0.34	329 ± 15	477 ± 15	453 ± 21	19.96 ± 0.03
22	5.33 ± 0.27	7.72 ± 0.39	347 ± 15	447 ± 15	447 ± 15	13.06 ± 0.03
	6.05 ± 0.30	14.56 ± 0.73	300 ± 15	398 ± 15	380 ± 21	13.66 ± 0.04

Table 3.8: Values extrapolated from current measure and bullet barycenter motion for neon in setups C and D. Δx_{targ} is the distance between electrode and target, V_p is the voltage peak for the pulse, i_p is the current peak value, $t_{0,i}$ is the starting time for the current value, $t_{p,i}$ is the time of the peak value, t_{imp} is the time of the impact of bullet on target, $x_{\text{target}} - x(t_{0,i})$ is the distance between bullet position when current peak starts and target position.

backstream described in figure 3.19.

In figure 3.29 is possible to see that the distant target (setup C) is reached by the bullet with medium and high voltage, but there isn't a change in luminosity. Near nozzle exit the bullet speeds up, reaches rapidly the target, stretches and then reduces its diameter to the impact point. For a close target there is a change in luminosity in correspondence of the negative voltage peak and of the second voltage positive peak. With high voltage the bullet shape is losed completely once plasma exits the nozzle, all the space between nozzle exit and target is completely filled by glowing gas.

Current measurements In figure 3.30 ad in table ?? there are results for the analysis of current measurements, similar to those done with helium. A current peak is measured only for high voltage with distant target and for medium and high voltage with close target. Starting time of current peak is again precedent to the impact time of the bullet with the target. Interaction distances presented in table are similar to the ones found for helium. The absence of the current peak for medium voltage with distant target could mean that the target is not reached by the charge carrier, even if we see luminosity on the target. With higher voltage the bullet and the charge carrier are more rapid, reach the target and we measure current.

Backstream Backstream phenomenon in neon is easily observable, where the bullet reaches the target there is high luminosity around nozzle exit. It presents itself as zone of glowing gas with large width and near constant height, with a barycenter motion that shift direction towards the electrode or towards the target. The changes of barycenter coordinates in time is so low that is not possible to infer it's dynamics. Once the pulse voltage lowers, also the backstream fade away.

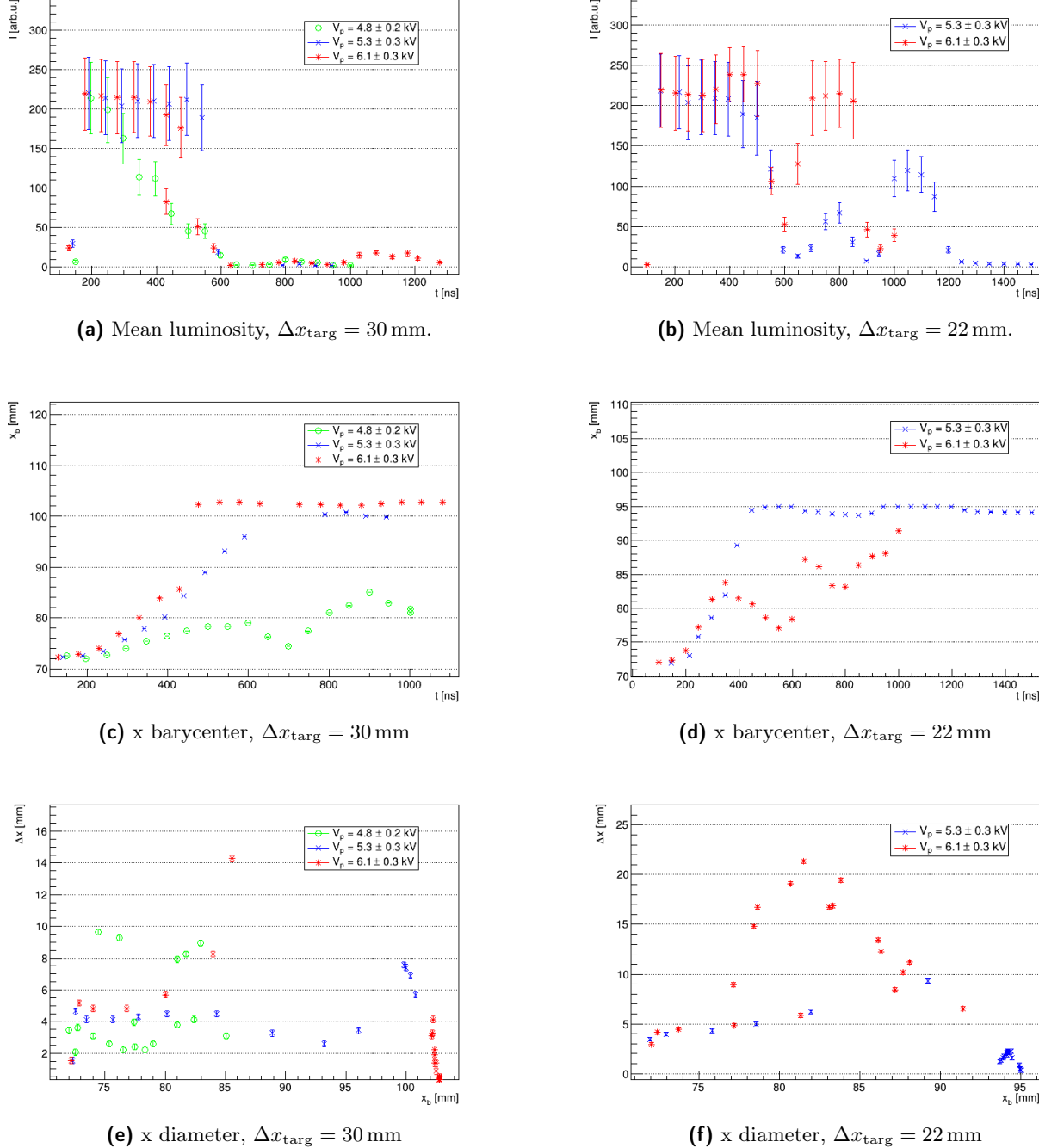
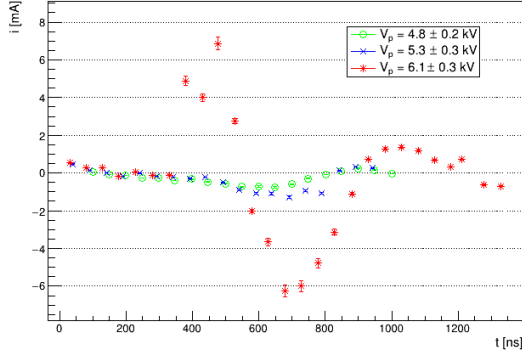
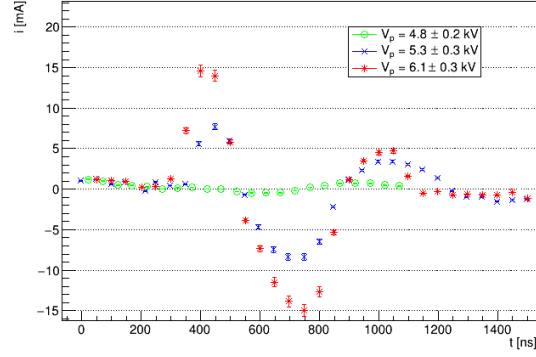
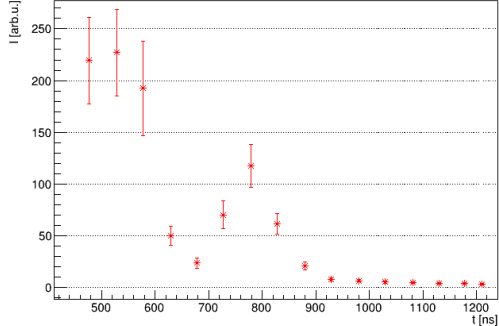
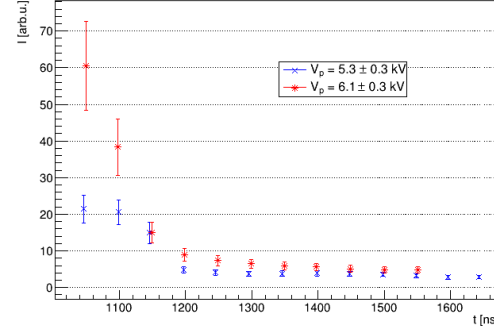
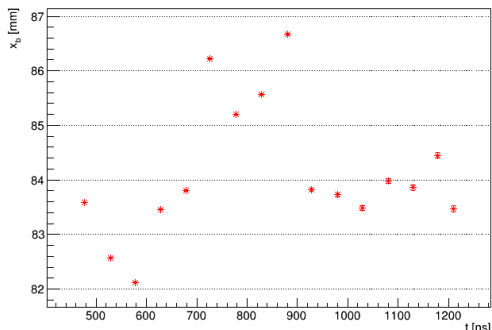
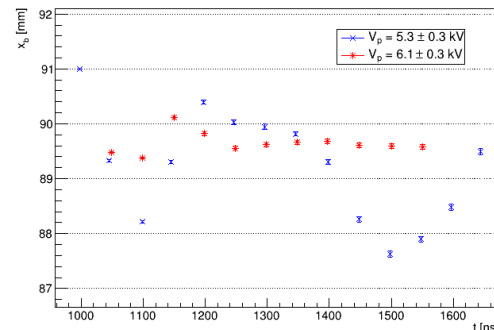
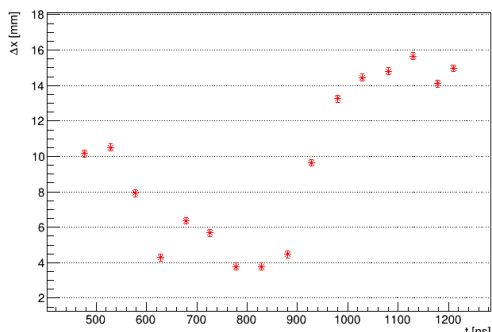
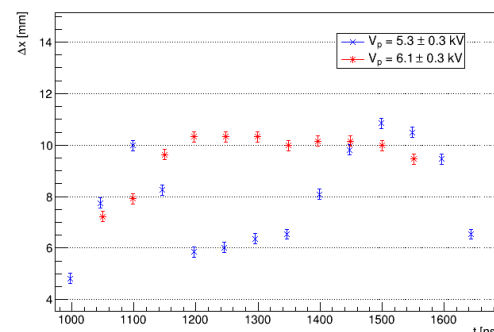


Figure 3.29: Results of the analysis for measurement setup C and D with neon gas, for different peak voltage values.

(a) $\Delta x_{\text{targ}} = 30 \text{ mm}$.(b) $\Delta x_{\text{targ}} = 22 \text{ mm}$.**Figure 3.30:** Current intensity measured for neon in setups C and D, with different voltage peak values.(a) Mean luminosity, $\Delta x_{\text{targ}} = 30 \text{ mm}$.(b) Mean luminosity, $\Delta x_{\text{targ}} = 22 \text{ mm}$.(c) Barycenter along x, $\Delta x_{\text{targ}} = 30 \text{ mm}$.(d) Barycenter along x, $\Delta x_{\text{targ}} = 22 \text{ mm}$.(e) Diameter along x, $\Delta x_{\text{targ}} = 30 \text{ mm}$.(f) Diameter along x, $\Delta x_{\text{targ}} = 22 \text{ mm}$.**Figure 3.31:** Analysis of the backstream in neon for measurement setups C and D.



(a) Picture of argon plasma.



(b) Frame after 120 ns from discharge start.

Figure 3.32: Example of argon discharge in measurement setup A.

3.4 Argon flow

The third noble gas used it's Argon, it is the harder one to produce plasma with at atmospheric pressure. Argon has a standard atomic weight of 39.948, 1st ionization energy of 15.760 eV and 2nd ionization energy of 27.629 eV. The peculiarity of this gas is its tendency to form filaments of plasma, instead of a large column as seen with helium or neon. Figure ?? shows an example where there is a grounded ring made of copper positioned around the outer nozzle, that allows to produce plasma with lower voltage and repetition rate. The chosen pulse repetition rate and an opening time for the voltage pulse are chosen to observe plasma formation with and without this ring, to see differences between the setups.

Along the production of filaments, argon shows also the tendency to transite from a glow to an arc discharge when a target is positioned near it, as in figure 3.33. As described in chapter 2, when there is a plasma arc there is also large current intensity circulating in plasma and in the target, a condition that has to be avoided for blood coagulation with cold plasma. Target position in measurement setups C and D is chosen to allow plasma impact without arc transition.

3.4.1 Dynamic example

An example of the dynamic can be seen with measurement setup A: argon flow of 2 L/min, presence of the grounded ring outside the nozzle and absence of target. Formation, expulsion and propagation of argon plasma is phenomenologically different if compared to helium or neon plasma, but can always be separated two phases: inside the nozzle and outside it.

Plasma formation Inside the nozzle plasma forms as filaments that start on the electrode and reach nozzle's walls, with different lengths for each frame. There isn't a uniform propagation of those filaments toward the exit, however after a time of 180 ns, every filament covers all the distance between electrode and nozzle exit (10 mm), as in figure 3.34. Hypotizing the definition of a propagating front composed by the filament's ends it would have a velocity of, at least, $v_N = 55.56 \text{ km/s}$.

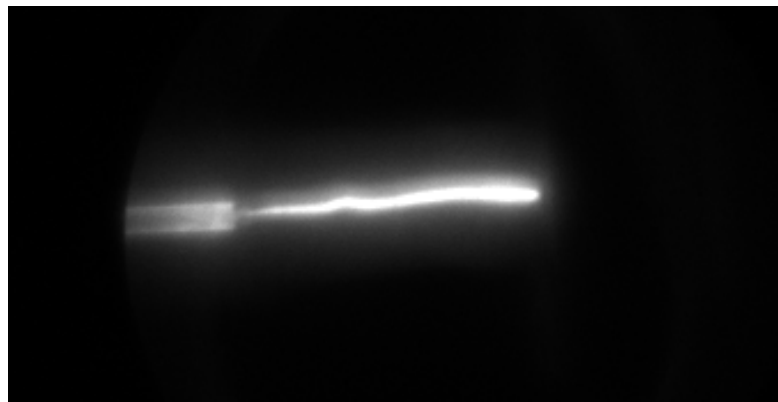
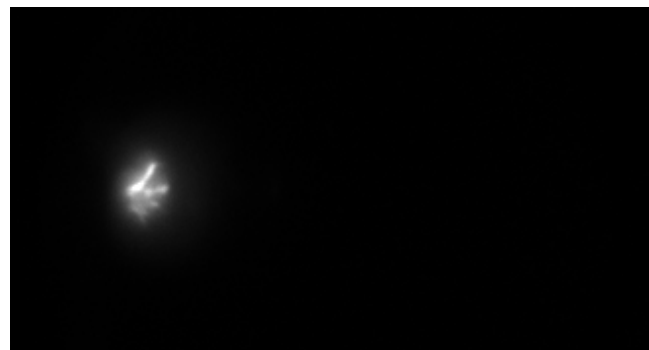


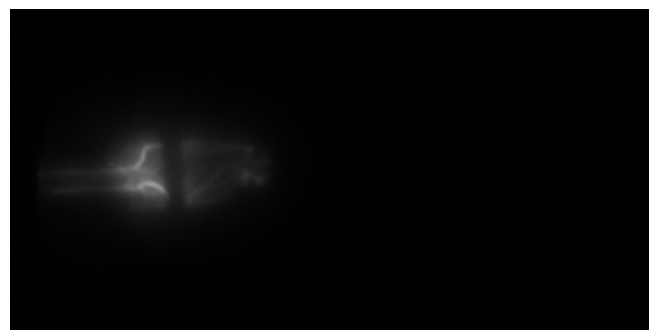
Figure 3.33: Example of arc discharge with argon and a target positioned 22 mm from the electrode, after 500 ns from discharge start. The arc covers all the gap between electrode on the left and conductive target on the right.



(a) $t = 0 \text{ ns}$



(b) $t = 80 \text{ ns}$



(c) $t = 180 \text{ ns}$

Figure 3.34: Propagation of argon plasma filaments inside the nozzle, measurements setup A.

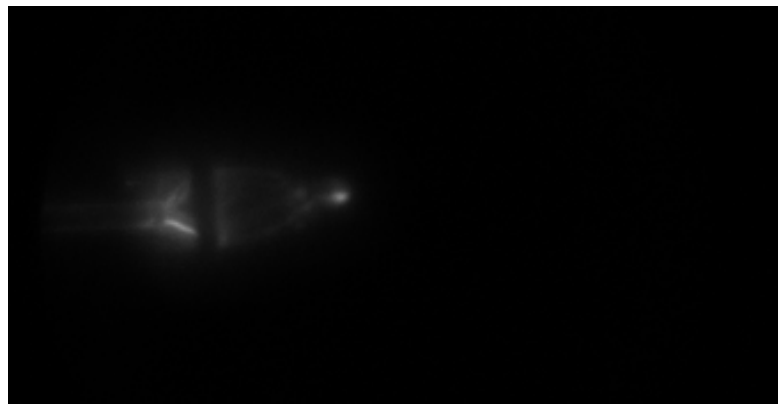


Figure 3.35: Expulsion of argon plasma in air at 220 ns from discharge start, measurements setup A.

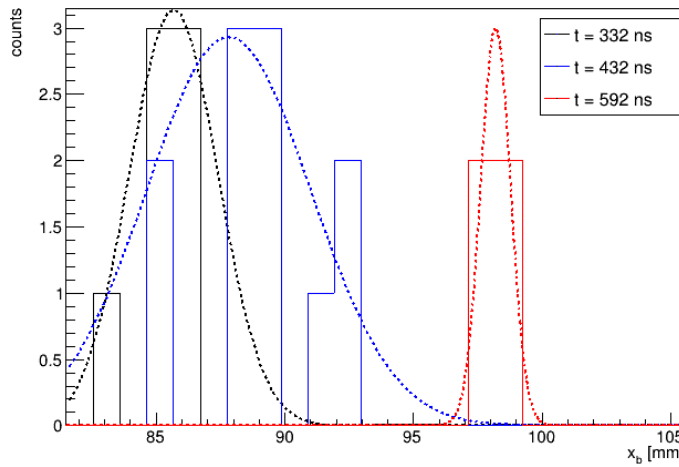


Figure 3.36: Distribution of barycenter's coordinate x , for plasma formations expelled from the source, at three different times, in measurements setup A. For each time, each bin counts how many formations are observed centered at a specific position x_b .

Plasma expulsion After the time interval where plasma is seen only inside the nozzle, it's possible to observe zones with high luminosity also in air. Plasma is expelled as tiny round shaped formations, separated from each other, as in figure 3.35.

For every frame there are several formations with different positions and diameters. It is possible to study the dynamic of plasma propagation studying the evolution of those parameters. For each frame each formation that presents luminosity over a limit value is isolated. It is possible to count how many formations there are, what are their mean luminosities, barycenter coordinates and diameters, as done with the bullets in helium and neon. Given a frame at a specific time, from those parameters are made histograms and is possible to extrapolate the parameter distribution. For different times, it's possible to compare those distributions, as it's done for barycenter's coordinate x in figure 3.36 as an example.

Given those distributions for every parameter, it's possible to evaluate the mean value for luminosity, barycenter coordinates and diameters at any given time, reconstructing an analysis similar to that presented for other gasses. Results are presented in figure 3.37, where the points are the mean value of the distribution and the error is associated with distribution widths.

The number of plasma formations follows voltage waveform: there are more plasma formations right after the voltage positive peak value and right after the voltage negative peak value. Also average luminosity shows this behavior: there is emission with more intensity right after the positive and the negative voltage peaks, with higher errors during the negative peak, showing that values are more

spread around the average value. Barycenter motion in the x direction shows that the distribution propagates during the time interval where voltage is positive and stops when it becomes zero, at a certain distance from the end of the nozzle. It's relevant to point out that the propagation is observed only outside the nozzle, so position values starts around 85 mm, that is the end of the nozzle. During the propagation phase it's possible to estimate a velocity for the mean value of those formations with a fit as shown in figure, resulting in $v_A = 30.16 \pm 3.56$ km/s. Diameters values are presented to show dimensions of plasma formations. Diameter along x and y direction varies in a range between 0.3 and 1.3 mm, with a stretch in the x direction where voltage's absolute value is higher, and a stable value in the y direction around 0.7 ± 0.2 mm.

3.4.2 Absence of target

The grounded ring positioned around the nozzle for measurements sets A and C, phenomenologically, helps the formation of plasma, allowing to produce it with lower amplitude and repetition rate of voltage pulses. The effects of this ring on plasma dynamics is analyzed comparing the expulsion of plasma in setups with or without it, respectively measurements set A and B.

Analysis is done as described before for setup A, results are in figure 3.39, where the voltage waveform is identical to the one presented in figure 3.37. As in setup A, the peak in plasma formation numbers and luminosity is in correspondence of voltage peak values, positive and negative. Interesting thing to note it's that the number of formations is always lower for measurements without the ring, implying that it's expelled more plasma when there is the ring. Baricenter position changes uniformly for both sets, resulting in a velocity of the mean value of $v_A = 47.90 \pm 4.75$ km/s with the ring and $v_A = 39.03 \pm 2.95$ km/s without it. Diameters have an average value higher for set A in both directions, but data is spread a lot for all measurements sets, so it's not possible to note differences outside the error.

Argon plasma dynamics doesn't change behavior introducing the grounded ring on the nozzle, but plasma formations that are expelled reach higher velocities.

3.4.3 Influence of target

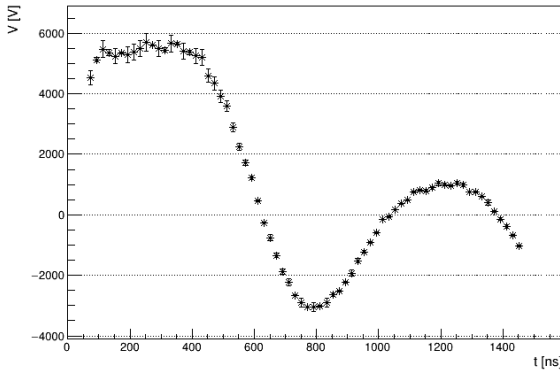
In measurements setups C and D is observed plasma formation and evolution with a copper target (the same described before) positioned at 30 mm, respectively with and without grounded ring around the nozzle.

Analysis is done as described before, results are in figure ??, where the voltage waveform is identical to the one in figure 3.37. For those setup the number of formations, their luminosity and the diameters are not influenced by the presence of the grounded ring. The most relevant difference between those measurements and the ones in setups A and B it's that now with the grounded ring the mean position of formations travels with a velocity lower than the velocity in absence of it. For setup C the velocity is $v_A = 30.49 \pm 4.10$ km/s, while for setup D, without the ring, it is $v_A = 61.24 \pm 2.84$ km/s.

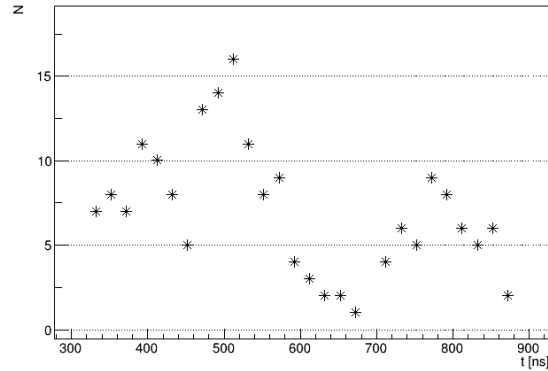
An explanation could be that plasma is attracted by a conductor at ground potential, when there isn't the grounded ring the target is the conductor at ground potential more close to the electrode, so plasma is attracted by it.

3.5 Hints on bullet propagation model

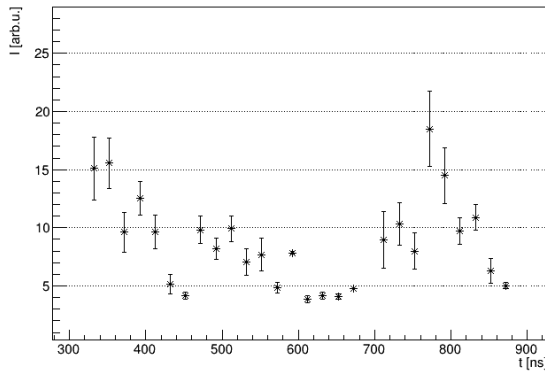
Formation and propagation of bullets in cold plasma discharges is a phenomenon that still has to be explained, there isn't a specific model that describes it in its entirety. From measurements shown before it is possible to make some hypothesis and correlate what we see to plasma parameters such as electron temperature and transport coefficients.



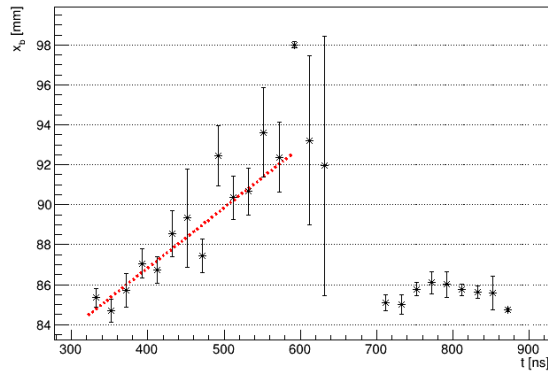
(a) Voltage waveform.



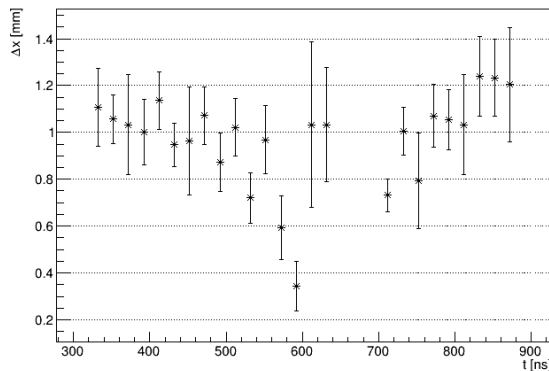
(b) Number of formations.



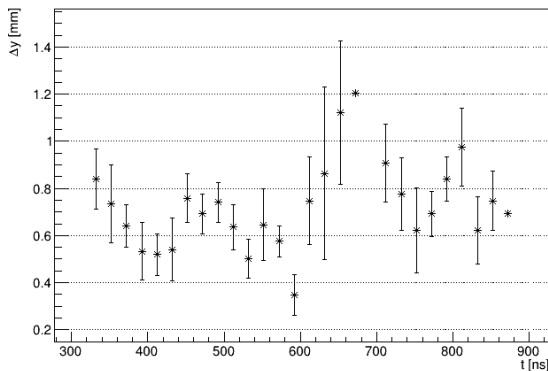
(c) Mean luminosity.



(d) Barycenter along x.



(e) Diameter along x.



(f) Diameter along y.

Figure 3.37: Analysis of argon plasma formations, measurements setup A. Every point identifies the mean value of considered parameter between all plasma formations observed at a given time, while the error is associated with the distribution width.

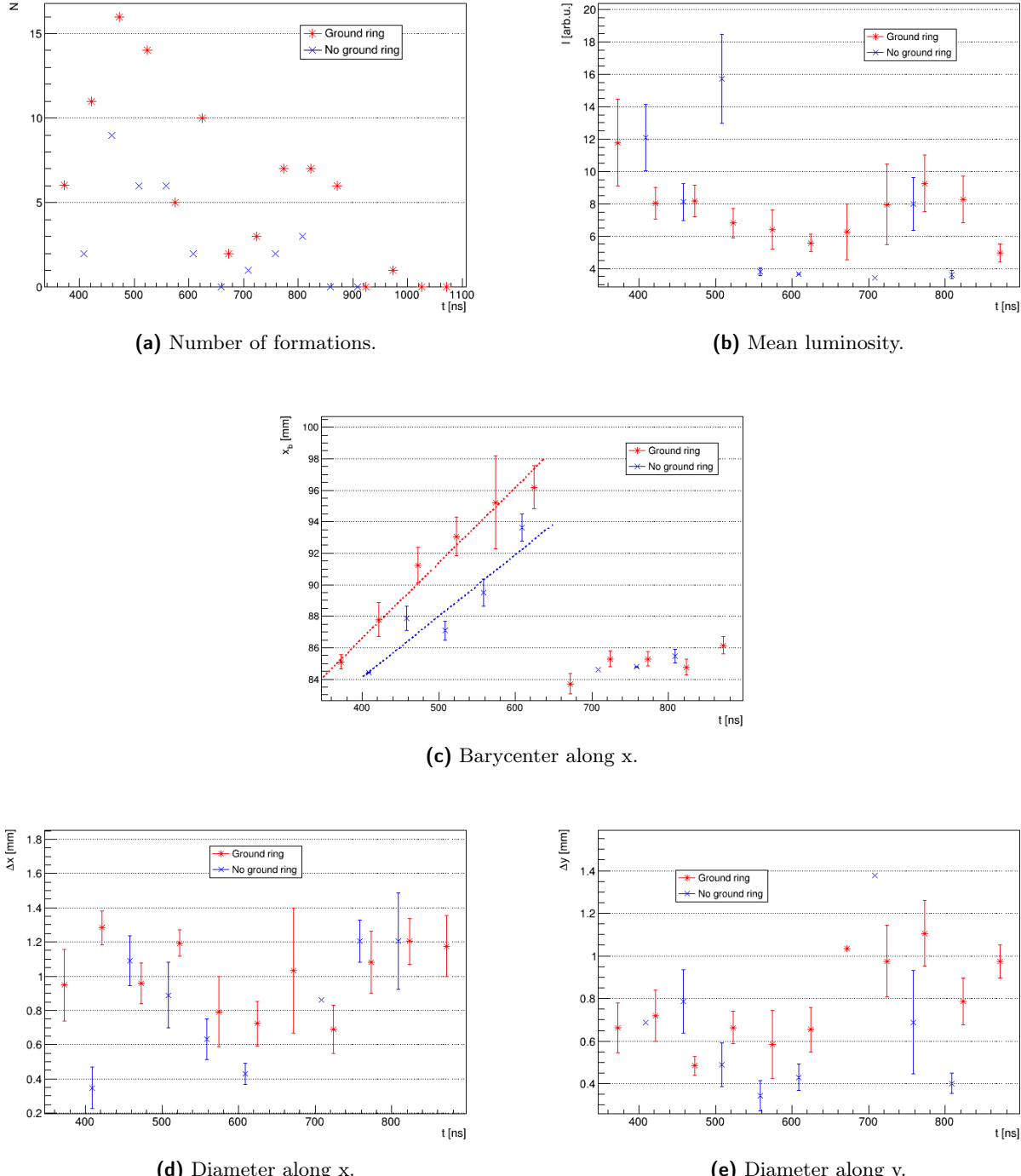
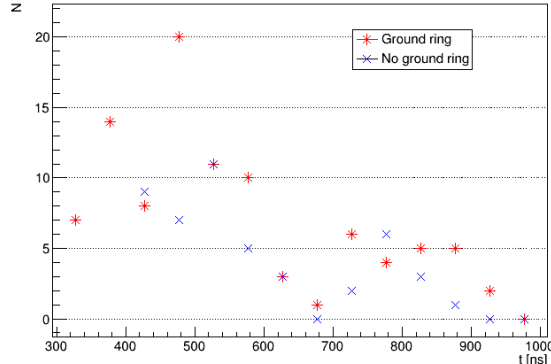
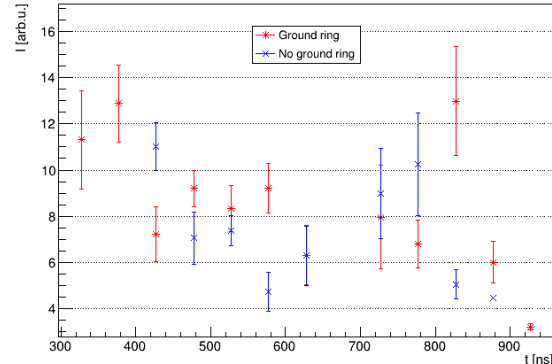


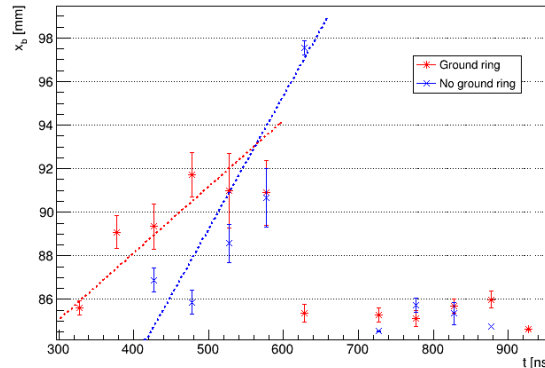
Figure 3.38: Analysis of argon plasma formations, with grounded ring positioned outside the nozzle (setup A) and without it (setup B).



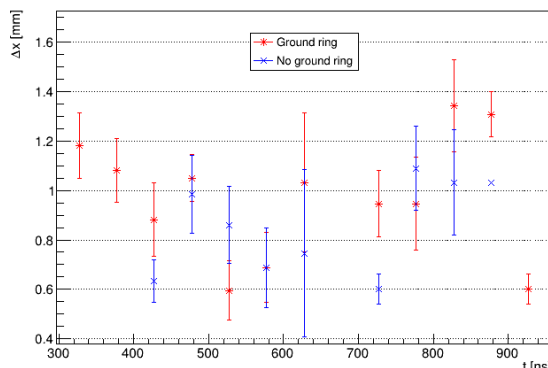
(a) Number of formations.



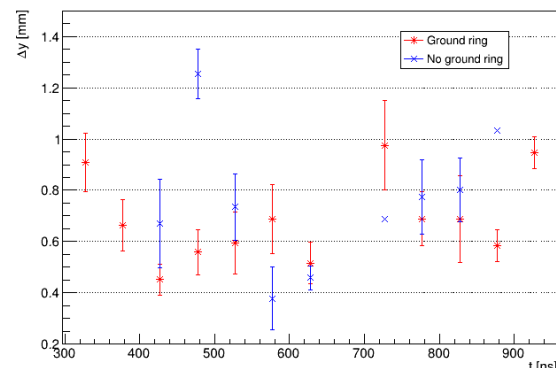
(b) Mean luminosity.



(c) Barycenter along x.



(d) Diameter along x.



(e) Diameter along y.

Figure 3.39: Analysis of argon plasma formations, when there is a target in front of nozzle exit, with grounded ring (setup C) and without it (setup D).

Bolsig+ and electron temperature There are a few softwares that can estimate electron temperature and its transport coefficients. In this work is utilized *Bolsig+*, a Boltzman equation solver that permits to evaluate plasma parameters with different gas temperature and composition ([51]).

Electron motion in a plasma inside an electric field E is described with the electron distribution function in the six-dimensional phase space f , estimated resolving the Boltzmann equation 3.2, where $C[f]$ represents the change rate of f due to collisions.

$$\frac{\partial f}{\partial t} + v \cdot \nabla f - \frac{e}{m} E \cdot \nabla_v f = C[f] \quad (3.2)$$

Once f is known, it's possible to evaluate the electron temperature T_e of the plasma considering that f should follow a Maxwell-Boltzmann distribution.

The first two moments of 3.2 are, respectively, the continuity equation and the momentum equation, approximated by the drift-diffusion equation, as in 3.3, where Γ is the electron flux, S is the electron source term related to reactions, μ is the mobility coefficient and D is the diffusion coefficient.

$$\begin{aligned} \frac{\partial n}{\partial t} + \nabla \Gamma &= S \\ \Gamma &= -\mu E n - \nabla(Dn) \end{aligned} \quad (3.3)$$

If an high intensity electric fields is applied to the gas, the drift term in electron motion controls plasma dynamics and electron velocity is proportional to its mobility.

Bolsig+ allows to insert reactions that have place inside the plasma, gas temperature and gas composition. Once those input values are inserted it uses approximations on the dependance of f from energy, time and space, to solve the equations shown before and simulate electron temperature and transport coefficients. Those parameters are found in function of the reduced electric field E/N , where N is the neutral numarical density of the plasma, that is the one of an ideal gas at atmospheric pressure $N = 2.687 \times 10^{25} \text{ m}^{-3}$.

Thys analysis includes four different gasses, to simulate the ones used and the principal components of air: helium, neon, nitrogen and oxygen. A selection of considered reactions is presented in table 3.9, they are taken from the archive in *LxCat* ([52]).

3.5.1 Ion waves or electron drift

The hypotesis under this study is that bullets visble radiation is emitted by recombination of ions and electrons inside the gas, giving birth to molecules and atoms in excited states that goes rapidly to lower energy levels emitting photons. A model for bullet propagation would have to elaborate a description of the conditions under which ions and excited species are created, how they propagates in space and how the behavior changes in different experimental setup, in agreement with the experimental results shown in this chapter.

For ionization propagation can be considered two possible different mechanisms: propagation of a ionization wave or electron motion.

Ion waves In absence of magnetic fields, neglecting reactions contribute to motion, it is possible to describe ions dynamics as in equations 3.4 ([53]), where M is the ion mass, n_i its density, γ_i is the adiabatic consant of ion species and T_i is the ion temperature.

$$\begin{aligned} \frac{\partial n_i}{\partial t} + \nabla \cdot (n_i v_i) &= 0 \\ M n_i \left(\frac{\partial v_i}{\partial t} + (v_i \cdot \nabla) v_i \right) &= e n_i E - \gamma_i K_B T_i \nabla n_i \end{aligned} \quad (3.4)$$

Gas	Reaction	Threshold energy [eV]	Description
He	-	-	elastic
	$\text{He} \longrightarrow \text{He}^*$	19.8	excitation
	$\text{He} \longrightarrow \text{He}^+$	24.6	ionization
Ne	-	-	elastic
	$\text{Ne} \longrightarrow \text{Ne}^*$	16.6	excitation (3P2)
	$\text{Ne} \longrightarrow \text{Ne}^*$	16.7	excitation (3P1)
	$\text{Ne} \longrightarrow \text{Ne}^*$	16.8	excitation (1P1)
	$\text{Ne} \longrightarrow \text{Ne}^+$	21.6	ionization
N_2	-	-	elastic
	$\text{N}_2 \longrightarrow \text{N}_2^*$	0.02	excitation (rot)
	$\text{N}_2 \longrightarrow \text{N}_2^*$	0.29	excitation (vib v=1)
	$\text{N}_2 \longrightarrow \text{N}_2^*$	0.59	excitation (vib v=2)
	$\text{N}_2 \longrightarrow \text{N}_2^*$	1.47	excitation (vib v=4)
	$\text{N}_2 \longrightarrow \text{N}_2^*$	6.17	excitation (vib A3 v=1-4)
	$\text{N}_2 \longrightarrow \text{N}_2^*$	7.00	excitation (vib A3 v=5-9)
	$\text{N}_2 \longrightarrow \text{N}_2^*$	11.03	excitation (ele C3)
	$\text{N}_2 \longrightarrow \text{N}_2^*$	11.87	excitation (ele E3)
	$\text{N}_2 \longrightarrow \text{N}_2^+$	15.59	ionization
O_2	$\text{O}_2 \longrightarrow \text{O}^- + \text{O}$	-	attachment (2body)
	-	-	elastic
	$\text{O}_2 \longrightarrow \text{O}_2^*$	0.02	excitation (rot)
	$\text{O}_2 \longrightarrow \text{O}_2^*$	0.19	excitation (vib v=1)
	$\text{O}_2 \longrightarrow \text{O}_2^*$	4.5	excitation
	$\text{O}_2 \longrightarrow \text{O}_2^*$	8.4	excitation
	$\text{O}_2 \longrightarrow \text{O}_2^+$	12.06	ionization

Table 3.9: Selection of reactions used for different gasses. Elastic reactions are momentum transfer reactions; excitation reactions could be rotational, vibrational (it is indicated the starting vibrational quantum number) or electronic.

Those equations can be linearized considering their equilibrium solution plus a perturbation on every parameter. This perturbation can be expanded in linear plane waves (for detailed calculations see [53]). Imposing also electroneutrality condition ($n_i = n_e = n$), eqautions 3.4 becomes equations 3.5, where all quantities with subscript 1 are perturbations, ϕ is the electric potential relative to the electric field E , ω is the angular frequency of the wave perturbation and k is its wavenumber.

$$\begin{aligned} n_1 &= n_0 \frac{e\phi_1}{K_B T_e} \\ i\omega n_1 &= n_0 i k v_{i1} \\ i\omega M n_0 v_{i1} &= ik K_B (T_e + \gamma_i T_i) \frac{n_0 k v_{i1}}{\omega} \end{aligned} \quad (3.5)$$

The solution of this equation is a wave with speed v_s in equation 3.6, and ion temperature can be neglected compared to electron temperature under our hypothesis.

$$v_s = \sqrt{\left(\frac{K_B T_e \gamma_i + K_B T_i}{M} \right)} \simeq \sqrt{\left(\frac{K_B T_e \gamma_i}{M} \right)} \quad (3.6)$$

Considering also the ionization and recombination contributions there would be a suppression factor that would decrease the amplitude of the perturbation over time and space.

Ultimately if there is a perturbation on the electric field in a plasma, it propagates with a velocity proportional to the square root of electron temperature over ion mass. It is possible that the velocity of those ion waves is comparable with bullets measured velocities.

Electron velocity The second hypotesis to explain bullet propagation is that it is related to the actual motion of electrons inside the plasma, that colliding with ions leads to reactions as expleined before.

There are two possible electron velocities values: electron thermal velocity, the speed of a particle at a specific temperature, or electron drift velocity, the speed of a charged particle inside an electric field. With electron temperature and mobility, simulated by *Bolsig+*, is possible to estimate the average thermal velocity and the drift velocity as in equation 3.7.

$$\begin{aligned} v_{th} &= \sqrt{\frac{2K_B T_e}{m_e}} \\ v_d &= \mu_e E \end{aligned} \quad (3.7)$$

Result comparison To give an electric field value as input in *Bolsig+* is possible to consider an electric field uniform in space with a conductive target positioned at 32 mm. In those conditions *Bolsig+* can estimate electron temperature and electron mobility, from them is possible to evaluate ionization wave velocity, thermal velocity and drift velocity, to be compared with bullet velocity in the nozzle. In table ?? are presented resulting parameters for helium and neon (compatible with those found [54], [55], [56]), in table ?? evaluated velocities.

All estimated velocities are lower then the actual measured velocities, but they have the same magnitude order, especially for drift velocities. Measured velocities are higher for neon bullets compared to helium bullets for the same voltage value, as shown in figure 3.26. This behavior is respected only by drift velocities, because neon has always higher mobility then helium, while other velocities decrease with increasing ion mass. It is possible to compare if the increase in velocity due to increase in voltage value is comparable with the increase of drift velocity. More specifically, the ratio of neon mobility over helium mobility has to be comparable with the ratio of the slopes in figure 3.26 for helium and neon. From the experiment ratio of the slopes is $m_{Ne}/m_{He} = 1.60$, while ratio of mobility values is

Gas	V_p [kV]	E [kV/m]	T_e [eV]	μ_e [m^2/sV]
He	5.7	190	4.5	0.080
	6.6	220	5.2	0.079
	7.3	243	5.8	0.080
Ne	4.8	160	7.2	0.144
	5.3	177	7.3	0.142
	6.1	203	7.6	0.140

Table 3.10: Plasma parameters with different peak voltage values.

Gas	v_N [km/s]	v_s [km/s]	v_{th} [km/s]	v_d [km/s]
He	37.72	13.42	14.73	15.23
	46.48	14.15	15.53	17.40
	59.80	14.84	16.29	19.41
Ne	34.59	7.30	8.06	23.04
	42.82	7.41	8.18	25.13
	62.92	7.51	8.30	28.42

Table 3.11: Plasma velocities for different voltage peak values, evaluated with parameters in 3.10. v_N is the experimental bullet velocity measured inside the nozzle; v_s is the ion wave velocity; v_{th} is the electron average thermal velocity; v_d is the electron drift velocity.

$\mu_{\text{Ne}}/\mu_{\text{He}} = 1.75$. The values are compatible so it is possible to assume that the increase in neon bullet velocities is correlated with the increase of its mobility.

It is not possible to know the have an exact measure of the electric field with our experiment, however, with the assumption that velocities inside the nozzle are drift velocities, is possible to have an estimation of the electric field needed to reach those velocities. Electric field intensities would range from 300 to 700 kV/m, plausible values with the voltage values and distances in the experiment.

3.5.2 Mobility and velocity

With the assumption that bullet velocity is proportional to electron mobility, it is possible to describe bullet propagation qualitatively, inside the nozzle and in air.

Electron mobility in a gas is proportional to reactions rate relative to the gas, changes in gas composition will change mobility. For this description helium gas will be mixed with nitrogen and oxygen in different proportions, where the ratio of nitrogen to oxygen concentration remains constant at 7/3, similar to the value in air.

In figure 3.40 there is mobility as a function of the helium fraction with different electric fields, or as function of the electric field with different helium fractions. It's interesting to see that mobility has a peak when a little percentage of air is mixed in helium.

Bullet in nozzle When the bullet propagates inside the nozzle the gas is approximately only composed by helium and the electric field decreases due to voltage decrease and distance from the electrode increase. In those conditions the drift velocity decreases linearly, as in figure 3.42 (b), and in a similar way the bullet decelerates (a). When the bullet meets the air outside, it goes from one line to another in the graph, increasing or decreasing its velocity based on the air composition.

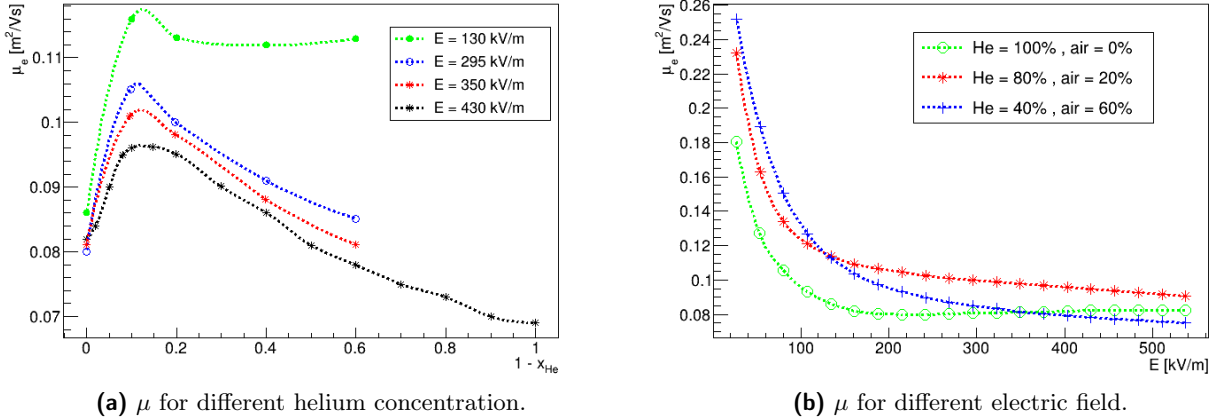


Figure 3.40: Electric mobility values with different electric field and gas composition. x_{He} is helium concentration, $1 - x_{He}$ is air concentration, where air is a gas of 70% nitrogen and 30% oxygen.

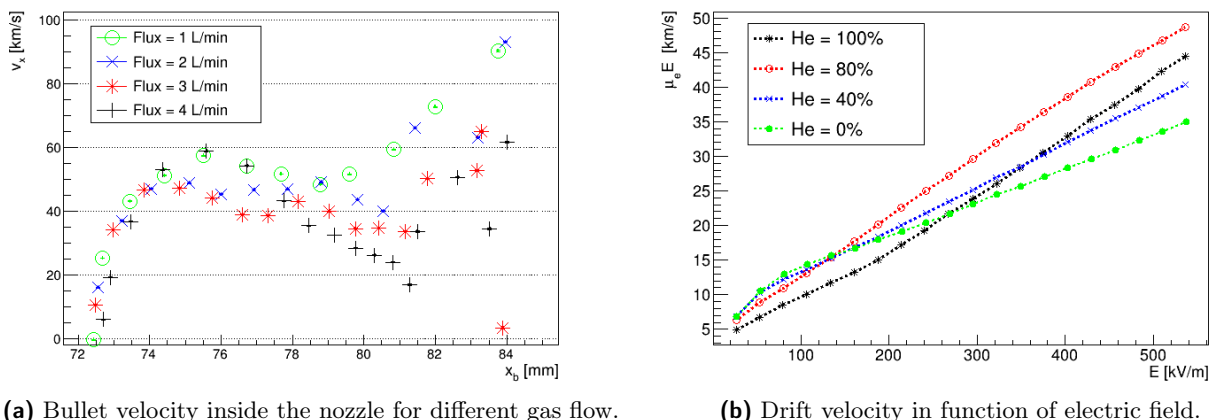
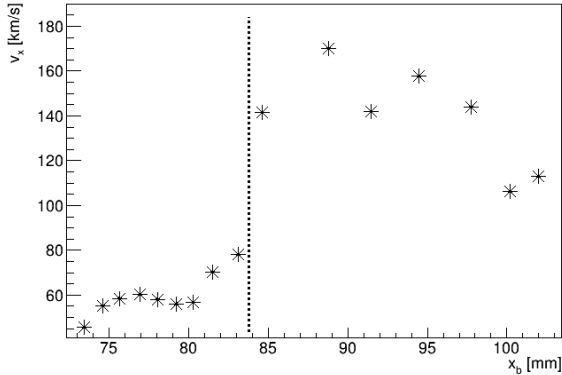
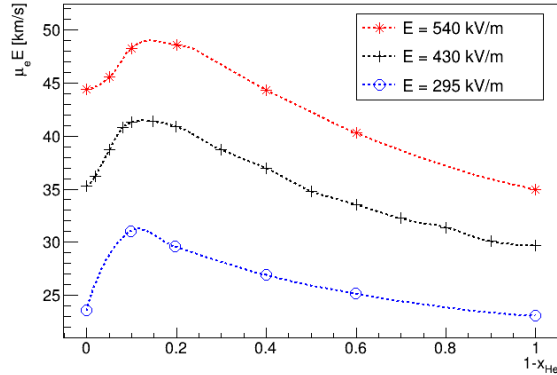


Figure 3.41: Comparison of bullet and drift velocity inside the nozzle.



(a) Bullet velocity at nozzle exit, gas flow = 2 L/min.



(b) Drift velocity in function of gas composition.

Figure 3.42: Comparison of bullet and drift velocity outside the nozzle.

Bullet in air When the bullet meets the air outside gas composition changes rapidly and consequently electron mobility changes. In measurements there is a peak in drift velocity right after nozzle exit, as there is a peak in electron mobility if we add a low percentage of nitrogen and oxygen in helium, figure ???. The drift velocity peak is higher for higher values of the electric field, compatible with what is seen from experiment.

Ultimately, there are several hints that suggests that bullet propagation velocity is correlated to electron mobility.

Chapter 4

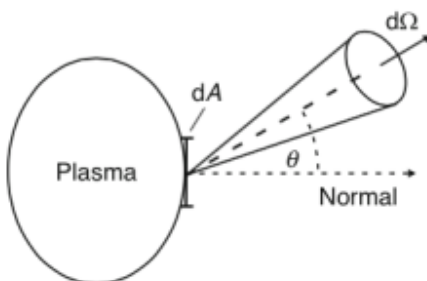
Spectral Analysis

One of the fundamental characteristics of Plasma Coagulation Controller for medical applications is what species are produced and deposited during its application. Various studies observed the spectrum of plasma DBD discharge in air at atmospheric pressure and ambient temperature ([57], [58]), it presents peaks relative to reactive species from water, oxygen, nitrogen and its oxides at visible wavelength, from 200 to 880 nm.

We are interested in plasma that contains molecules involved in blood coagulation mechanisms, Reactive Oxidant Species (such as hydroxyl radical OH) and Reactive Nitrogen Species (derived from nitric oxide NO) ([59]). In this spectroscopy study we give particular attention to them and their precursor, i.e. the presence of transitions relative to hydroxyl, oxygen and molecular nitrogen.

4.1 Radiation emission

The source produces plasma from a mixture gas of helium (or neon or argon) and air, along free electrons there are ions and species that collide with energetic electrons, and populate excited or metastable states with short lifetime. All reactive species participate in different reactions, and also in excitation and de-excitation reactions with consequent emission of radiation. When an electron goes from state p at higher energy to state k of lower energy, is emitted radiation with central wavelength λ_0 . Power emitted by this radiation is given by radiant flux $d\phi_\lambda$ and selecting a solid angle as in figure, is possible to define radiance L_λ , and intensity I , as in equations 4.1. Intensity for a radiation ultimately depends on $n(p)$, population density for state p, and Einstein Coefficient for the transition A_{pk} that is typical for the transition ([60]).



$$\begin{aligned}\lambda_0 &= \frac{hc}{E_p - E_k} \\ L_\lambda &= \frac{d^2\phi_\lambda}{dA \cos(\theta)d\Omega} \\ I &= \int L_\lambda d\lambda = n(p)A_{pk}\end{aligned}\quad (4.1)$$

Using air as gas, composed by molecules, reaction that emits radiation in visible wavelength are vibronic transitions where molecule goes from a vibrational state to another, with a change of vibrational quantum number ν , and/or from a rotational state to another, with change of quantum number J ([61], [62]). When there is a vibrational transition, each line corresponds to different numbers $\nu' - \nu''$, these are transitions well spaced in the spectrum, easy to recognize. Rotational transitions gives birth to bands of peaks not spaced much, hard to resolve without an efficient spectrometer.



Figure 4.1: Setup of the experiment for line recognition: we can see the source, the metal target and the optical setup on the left. Plasma emission is collected by the lens and sent to the spectrometer.

There are many reactions involving oxygen and nitrogen (see for example [63]), in this study we determine only principal transition observable with our spectrometer, to know dominant reactive species present in our plasma plume.

The experiments divides in emission line recognition and intensity measurements at different positions and with different gas mixtures.

4.2 Line recognition

We hypotize that plasma emission lines don't depend on which source we use, but on the discharge parameters, as described in chapter 2, we utilize prototype **A** presented before. A metal plate is positioned as target at a distance of 10 mm from plasma exit, as in figure 4.1. To start the discharge we use helium, with flow set to 2 L/min.

For line recognition we utilize an IsoPlane spectrometer, that separates emissions with different wavelengths with a grating. The spectrometer has a focal length of 320 mm and is equipped with three different gratings: 150, 1200 and 2400 gg/mm, corresponding to different resolutions. As in figure 4.1, light emitted by plasma is collected with a quartz lens and passes through an optical fiber connected to the spectrometer entry, while at the spectrometer exit there is a CCD camera of 2048 pixels and a count limit of 65 000.

Once a grating is chosen, we can set the start wavelength on the acquisition system and from there it takes measures until the end of the CCD, for a specific wavelength interval for every grating. For each measure we select an appropriate acquisition time that allows to observe peaks with a good count number and avoid saturation.

It's important to stress out that, with this measuring method and due to complexity of plasma reactions and composition, it's not possible to extrapolate quantitative considerations between different species concentration. However it's possible to recognize the presence of certain species and make some considerations watching spectra variation with different experimental setup.

4.2.1 Emission measurements

To see what's generally produced in a discharge we take the spectrum for the entire wavelength's region interested, from 230 to 800 nm, with standard discharge parameters: $f = 5 \text{ kHz}$ and $\Delta t = 15 \mu\text{s}$. First we do a rapid acquisition with the lowest resolution possible, to see interesting regions and have an idea of required exposition times. After that we do another acquisition with higher resolution for all wavelengths, measuring several spectra. The entire spectrum is reconstructed attaching different spectra, showed in figure 4.2, where are labelled principal transitions. For every measure we take also a background spectrum, without plasma, to recognize peaks that are not from the plasma.

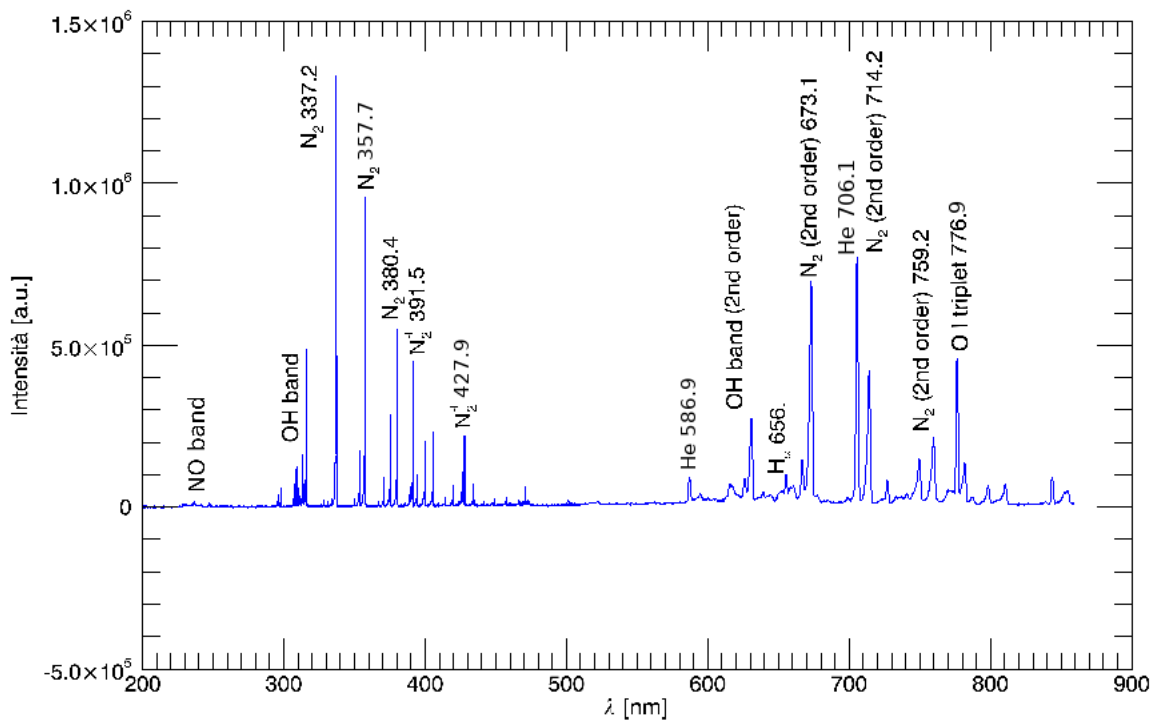


Figure 4.2: Spectrum with an helium flow of 2 L/min, pulse parameters of $f = 5$ kHz and $\Delta t = 16\ \mu\text{s}$. The emission is collected at the end of the nozzle, where plasma exits in air.

We read data with IDL routines ([64]) and analyze it with ROOT *TSpectrum.h* library ([65]). In every spectrum we divide each channel by the exposition time of the spectrum, evaluating the count rate at a specific wavelenght. We estimate white noise contribution as the average value from a portion of the spectrum that doesn't presents peaks, and subtract it to count rates for each wavelenght. In those spectrum we find emission peaks with *TSpectrum* functions (where is possible to set a treshold in heigth and the general width for lines to be searched) and isolate peaks from background. The exact wavelenght for each transition is found with a gaussian fit in an interval that takes into consideration the asymmetry where it's needed.

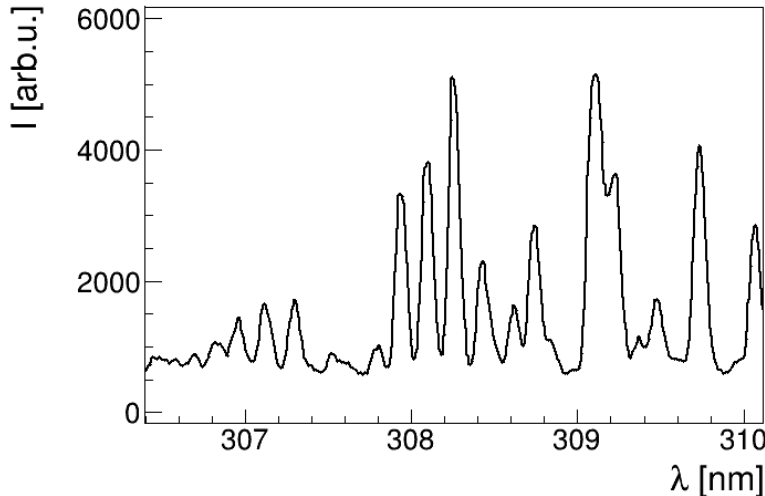
As said before, this study is focused on measure related to ROS and NRS, so in lines for NO, OH and N₂.

NO lines We observe two doublets for the transition A²Σ⁺ → X²Π with vibrational numbers (0-0) and (0-1) ([66], [67]), presented in table 4.1. Intensities for the peaks are normalized with maximum value of 1000 for the acquisition, the table shows as the intensities for this transition is very low. Other transition relative to this molecule have even lower relative intensity and are not observed in our study.

OH lines We find the rotational band for transition (A²Σ, ν' = 0 → X²Π, ν'' = 0), observing 13 principal lines ([68]). In figure 4.3 a zoom on the spectrum, in table 4.2 peak values.

N₂ and N₂⁺ lines Measured spectrum presents several lines relative to nitrogen molecules, including the strongest, for diatomic molecule dinitrogen. We observe the Second Positive System for N₂ transition C³Π → B³Π and the First Negative System for N₂⁺ transition B²Σ → X²Σ, in table

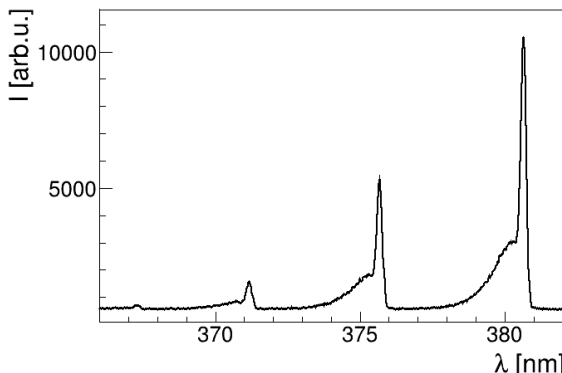
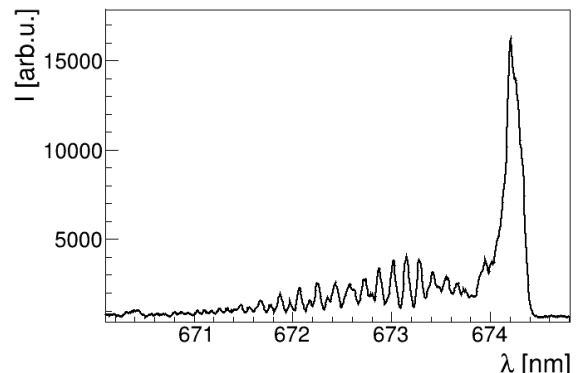
λ [nm]	I [arb.u.]
236.31 ± 0.24	27
237.00 ± 0.15	26
247.02 ± 0.05	28
247.86 ± 0.12	27

Table 4.1: Peaks measured for NO.**Figure 4.3:** Zoom on OH peaks

4.3 peak values ([69], [70]). For N₂ is found also a band of multiple rotational lines centered around 336.58 ± 0.01 nm. Some of the peaks are seen in the second diffraction order, where there is more distance between lines. In figure 4.4 we present two zooms for N₂ lines.

Atomic lines We observe other lines from elements present in the plume ([71]):

- H _{α} line corresponding to transition from quantum number $n = 3$ to $n = 2$
- He two of the strongest lines for helium
- O strong line of oxygen

(a) Transitions with $\Delta\nu = 2$ (b) Strongest line (0-0), 2nd diffraction order**Figure 4.4:** Zoom on N₂ transitions.

λ [nm]	I [arb.u.]
306.96 ± 0.01	53
307.11 ± 0.01	58
307.29 ± 0.01	62
307.94 ± 0.01	142
308.09 ± 0.01	148
308.26 ± 0.01	161
308.43 ± 0.01	112
308.62 ± 0.01	46
308.74 ± 0.01	137
309.11 ± 0.01	151
309.22 ± 0.01	120
309.45 ± 0.01	36
309.73 ± 0.01	125

Table 4.2: Peaks measured for OH.

	λ [nm]	I [arb.u.]	$(\nu' - \nu'')$
N_2	316.03 ± 0.01	381	(1-0)
	337.11 ± 0.01	1000	(0-0)
	357.77 ± 0.01	722	(0-1)
N_2	367.22 ± 0.20	58	(3-5)
	371.12 ± 0.04	172	(2-4)
	375.66 ± 0.02	232	(1-3)
	380.64 ± 0.02	423	(0-2)
N_2^+	391.50 ± 0.02	355	(0-0)
	427.45 ± 0.02	180	(0-1)

Table 4.3: Peaks measured for N_2 and N_2^+ .

	λ [nm]	I [arb.u.]
H_α	655.96 ± 0.04	113
He	586.94 ± 0.05	122
	705.56 ± 0.01	649
O	776.89 ± 0.01	393

Table 4.4: Lines measured for H, He and O.

4.3 Relative intensities

To understand the mechanisms of plasma expulsion and deposition, we measure plasma emission intensity varying voltage peak values, line of sight of the spectrometer and gas composition.

4.3.1 Pulse settings

We measure emission lines with different parameters for the voltage pulse, utilizing the same experimental apparatus as before. As seen in chapter 2 for different pulse repetition rates we have the same electric behavior, but this parameter could still influence species production rates.

We observe spectra with three different parameter combinations, corresponding to different intensity of the treatment:

- low: $f = 5 \text{ kHz}$ and $\Delta t = 15 \mu\text{s}$
- medium: $f = 10 \text{ kHz}$ and $\Delta t = 10 \mu\text{s}$
- high : $f = 15 \text{ kHz}$ and $\Delta t = 10 \mu\text{s}$

For every setting we collect plasma emission along two different line of sight:

- position 1: as close as possible to the end of the nozzle, near plasma exit point from the source;
- position 2: close to the target, at 10 mm from plasma exit point, where it collides with target.

We evaluate intensities for OH and N₂ species, collectively for the lines in a wavelength range specific for the peaks. For OH lines is considered all the rotational band between 306-309 nm, lines for N₂ are separated in those between 335-337 nm (rotational band and (0-0) transition) and those between 368-382 nm (vibrational transitions with $\Delta\nu = 2$).

In figure 4.5 we present measurements result for considered lines. .

Intensities for OH decreases drastically increasing the distance from the source, in position 2 we find values lower than 0.1% of those from position 1. OH lines for both positions have same intensity with low and medium power setup, while is lower with higher frequency, with similar behavior in both positions.

Also N₂ intensities depend on pulse repetition rate: they decrease with higher pulse rates, for every lines, reaching around 0.6% for $f = 15 \text{ kHz}$ in position 1, and lower values for position 2.

It seems that production of both those reactive species have rates dependant from pulse repetition rates, in particular the intensity of their emission decreases at higher frequencies.

4.3.2 Line of Sight

We want to analyze plasma emission at different positions with the other source analyzed in this work, prototype **B** in chapter 2, in a similar way to what we did in the previous measurements. The setup is similar to the one described in chapter 3: as in figure 4.6, we utilize the glass nozzle and a conductive target at 10 mm from its end.

We utilize a mini-spectrometer *Hamamatsu C10082CAH*, with resolution of 1 nm, spectral range from 200 nm to 800 nm and a CCD sensor *S10420-1106* with 2048 pixels. We find the efficiency of the spectrometer for different wavelenghts with measurements of emission from a lamp with known emission spectrum.

To produce plasma we use three different gasses: helium with a flow of 2 L/min, neon with gas flow 2.5 L/min and argon with flow 2 L/min.

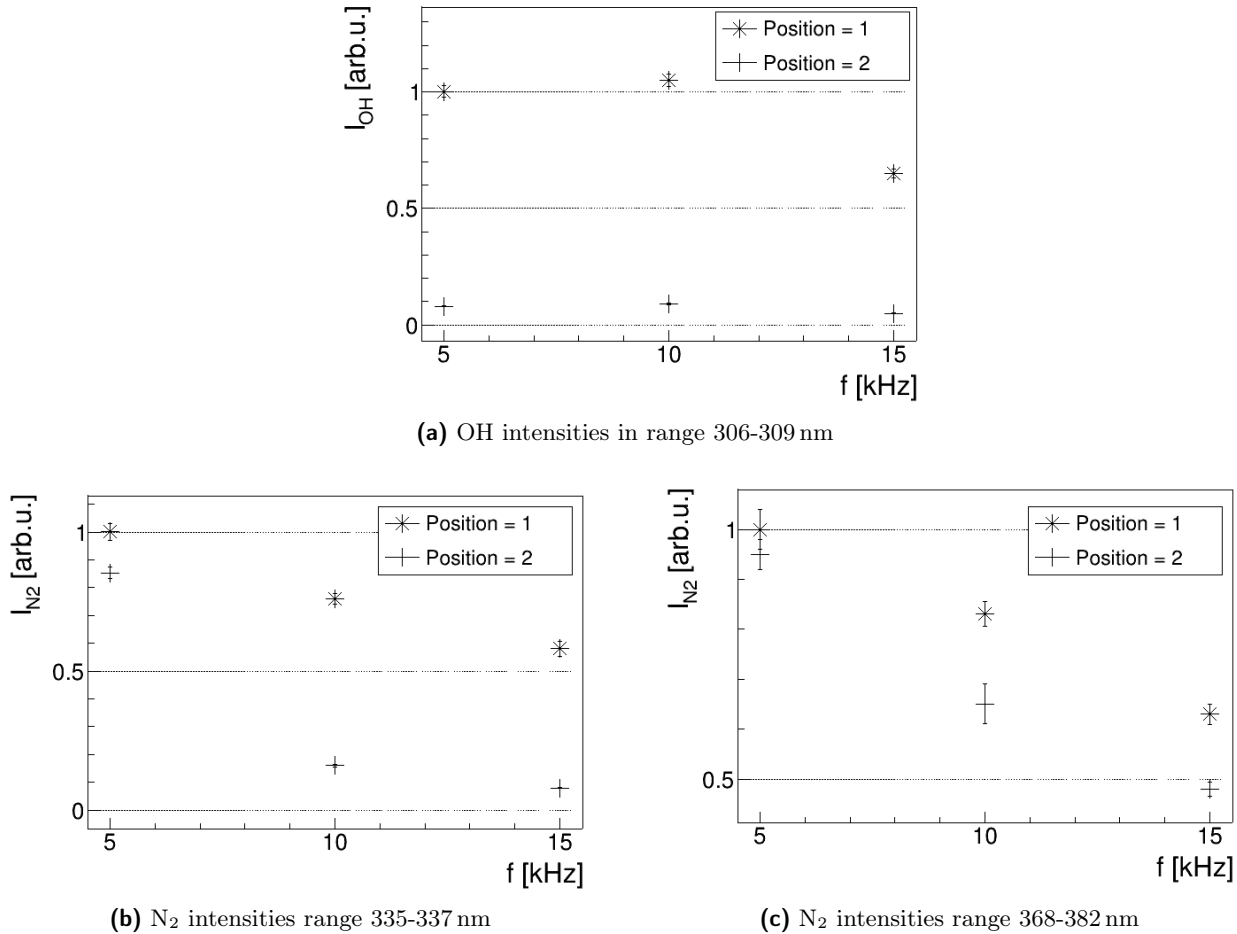


Figure 4.5: Relative intensities of selected portions of the spectrum, for different pulse repetition rates, for position 1 and position 2.

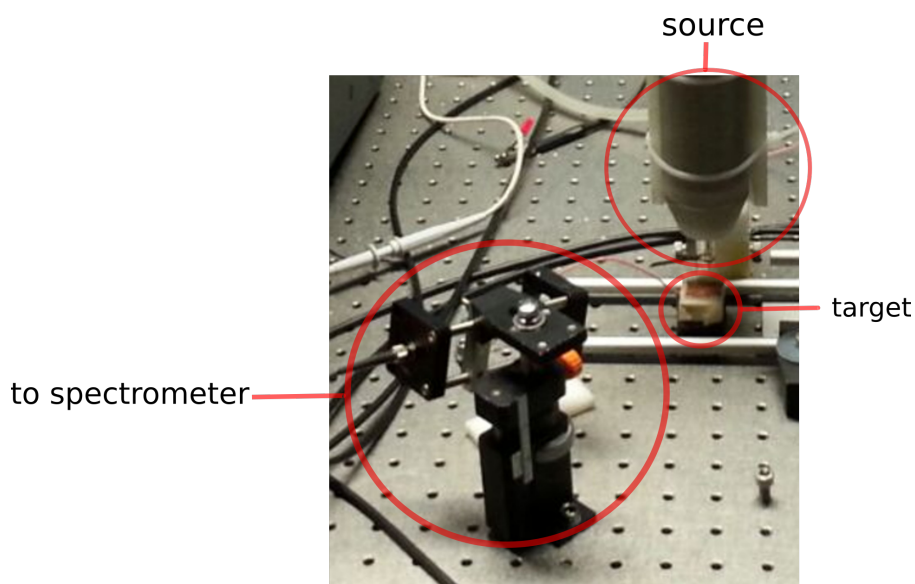


Figure 4.6: Setup of the experiment for intensity measurements: we can see spectrometer's lens on the left, the source and the metal target.

The experimental setup allows to measure plasma emission at different heights along the nozzle axis, we evaluate intensity in four different positions:

- -5 mm, inside the nozzle
- 0 mm, at the end of the nozzle
- 5 mm, between nozzle and target
- 10 mm, right before target position

We consider the total emission for the entire spectral range 200-800 nm and the relative emission for some selected lines, different for the different gasses:

- N₂ : three lines centered at 364.2 nm (transition (1 - 0)), 383.0 nm (transition (0 - 0)) and 403.9 nm (transition (2 - 4));
- He : one line at 446.2 nm;
- Ne : one doublet at 628.8 nm and 630.6 nm, one doublet at 639.2 nm and 641.0 nm and a single line at 683.1 nm;
- Ar : three different lines at 722.9 nm, 734.0 nm and 772.6 nm.

Results are in figure 4.7. We normalize total intensities to compare emissivity variation for different positions, while relative intensities are divided for the respective total intensity and multiplied for spectrometer efficiency for considered wavelenght. When we use helium to start plasma, emission is lower inside the nozzle, increase at the exit and decreases slightly moving towards the target. For other gasses emission decreases increasing distance from the source. For every gas, emission from N₂ increases until it reaches a constant value. Lines from specific gasses decreases distant from the nozzle, with slope different for different gasses. It's interesting to note how neon emission decreases linearly, while N₂ emission increases and it's an effect that we can see visually: going from the nozzle to the target plasma color goes to red (neon emission) to violet (nitrogen emission).

As we could expect we see that inside the nozzle the emission depends from the gas we use to start the plasma, going outside emission due to nitrogen species becomes dominant in the discharge.

4.3.3 Gas composition

We use helium as starting gas, mixed with argon or nitrogen using specific flowmeters, that allows to add up to 0.2 L/min, with resolution of 0.01 L/min. If we set the helium flow to 2 L/min, we can have gas mixtures where argon and nitrogen have a maximum percentage of 10%.

We point the spectrometer at the end of the nozzle and collect spectra for three different gas concentrations, finding the intensities in figure 4.8. When we add nitrogen to the gas, total emission intensity lowers, while nitrogen emission doesn't change as expected. We have this result because we are increasing very slightly nitrogen concentration respect to the quantity naturally present in air, it means that at the end of the nozzle we already see all possible nitrogen emission due to molecules naturally present in air. When we add argon, the total emission increases, while relative emission from elements other than argon decreases slightly, as we expect if we add he argon lines to the total sum. It means that the only variation when we add argon is that we see the emission relative to this element, the emission relative to other elements stays unchanged.

4.4 Estimation of plasma temperatures

From diatomic molecule's spectra it's possible to evaluate some parameters that are indicators of plasma's state: rotational temperatures for OH and N₂, T_r , and vibrational temperature for N₂, T_v .

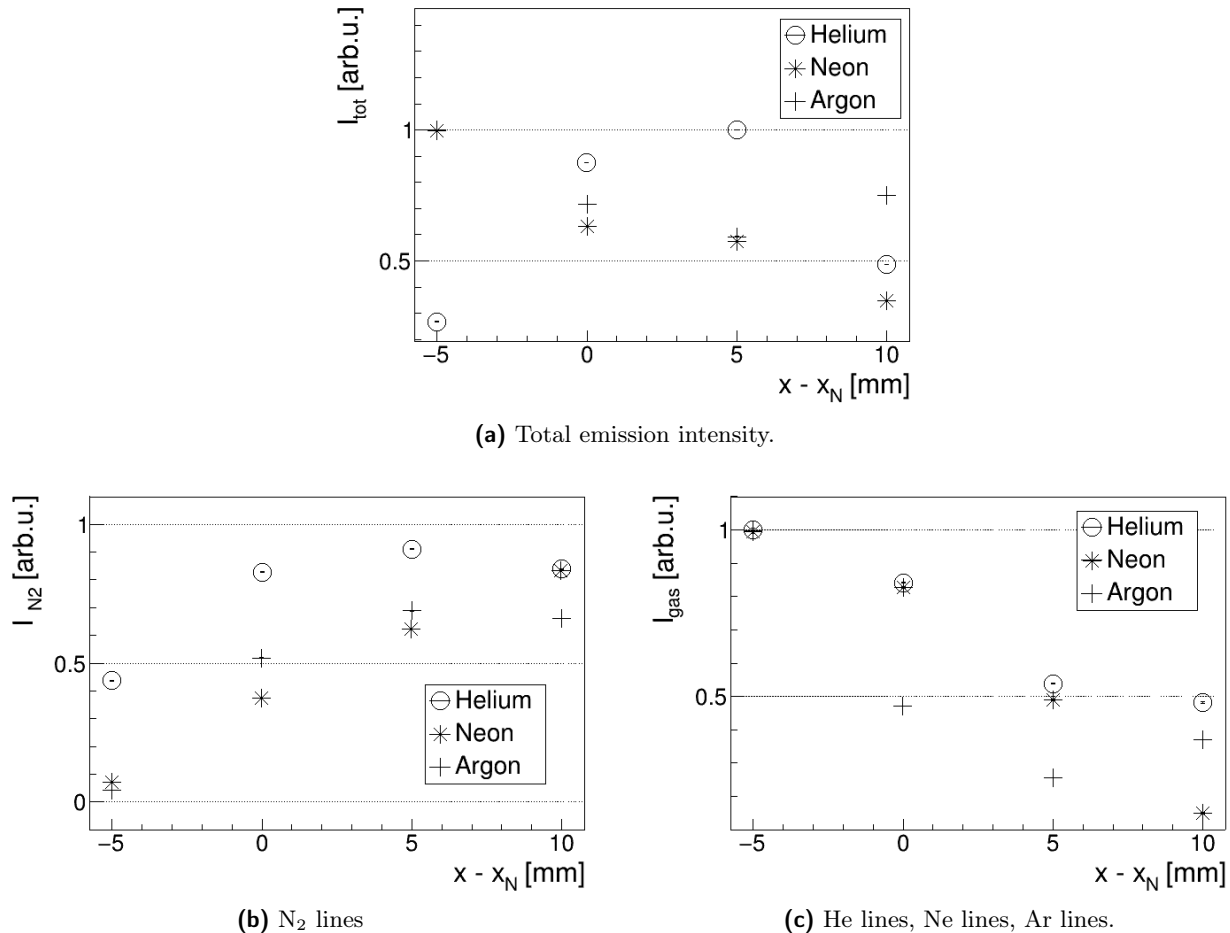


Figure 4.7: Behavior of total intensities (a) and relative intensities for selected portions of the spectrum (b-c-d), changing spectrometer's line of sight, with different starting gas. At 0 mm the lens points at the end of the nozzle, at 10 mm at a metal target. Relative intensities in (d) are for lines corresponding to the element that we use as starting gas. Relative intensities take into consideration spectrometer's efficiency and total emission for every position.

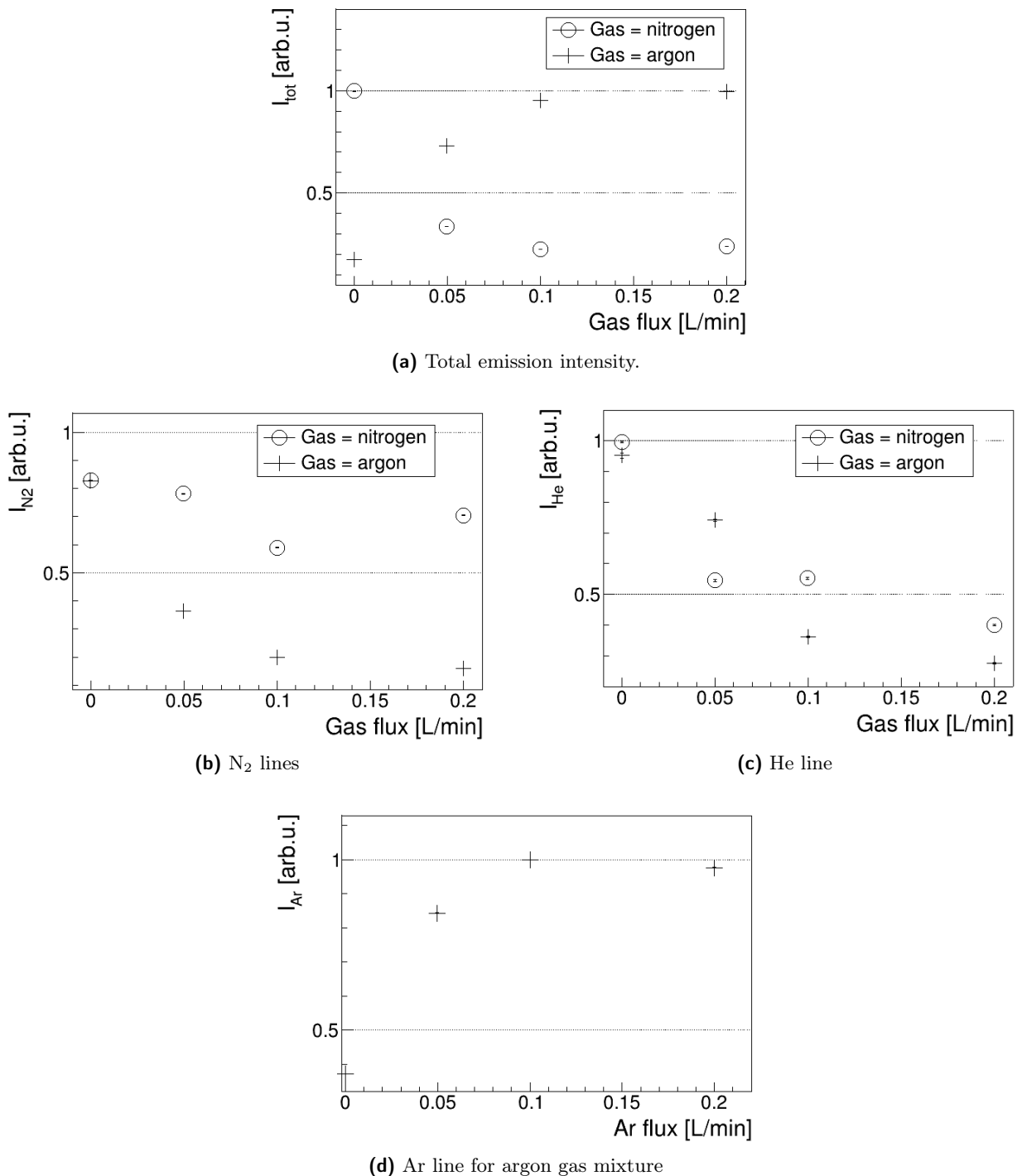


Figure 4.8: Behavior of total intensities (a) and relative intensities for selected portions of the spectrum (b-c-d-e), changing the composition of the gas. A flow of 0.2 L/min corresponds to the 10% of the total gas flow. Relative intensities take into consideration spectrometer's efficiency and total emission for every gas mixture.

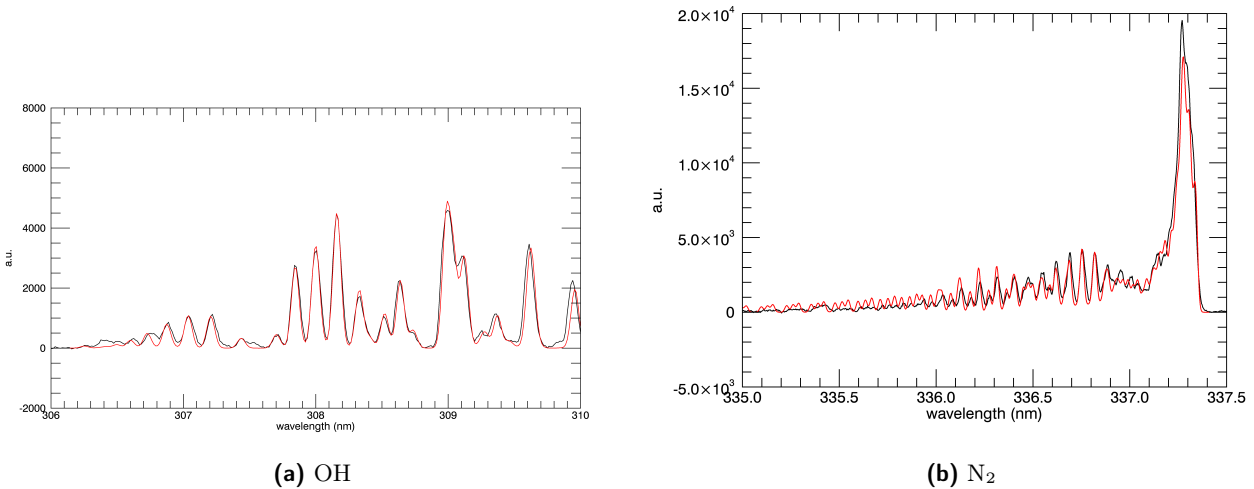


Figure 4.9: Example of optimal spectrum simulation for OH and N₂ considered species.

These parameters are estimation of the temperature at which thermal energy is comparable to the gap energy between rotational or vibrational state transitions, they can be defined as in equations 4.2 where ν is the vibrational quantum number and I is the quantized moment of inertia of the molecule.

$$\begin{aligned} T_r &= \frac{\hbar^2}{2k_B I} \\ T_v &= \frac{h\nu}{k_B} \end{aligned} \quad (4.2)$$

Rotational temperatures can be considered an estimation of neutral gas kinetic temperature. Vibrational temperature gives an idea of the population of vibrational states, useful to determine chemical reactions inside plasma.

4.4.1 Rotational temperature for OH and for N₂

In rotational bands the intensity of a transition for a specific wavelength is proportional to the number density population of upper state (equation 4.1), that, considering a Maxwell-Boltzmann distribution, is proportional to the temperature of the species. In equation 4.3 the proportionality is explicated, with D_0 parameter that depends on number of initial molecules, partition function of the rotational state and quantum rotational numbers for upper and lower state, S is the oscillator strength specific for the molecule and E_r depends from a constant defined by the vibrational state and from quantum rotational number for upper state ([72]).

$$I = \left(\frac{2\pi}{\lambda}\right)^4 D_0 S \exp\left(-\frac{E_r}{k_B T_r}\right) \quad (4.3)$$

As explained before, rotational bands have many lines, not distinguishable with our spectrometer, an approach to temperature estimation is to simulate spectra with different temperatures and to minimize differences for measured spectrum ([73]). In a predetermined range of temperatures we simulate different spectra with different temperatures, where each line is a gaussian peak with its width that takes into consideration broadening due to thermal motion, Doppler effect and measure resolution. For every spectrum we estimate the mean square difference and select the temperature associated with the minimum difference, while we estimate the error taking an upper and a lower limit where difference is larger by 5% of the minimum value. An example of the spectra is in figure 4.9, while resulting temperatures are in figure 4.10.

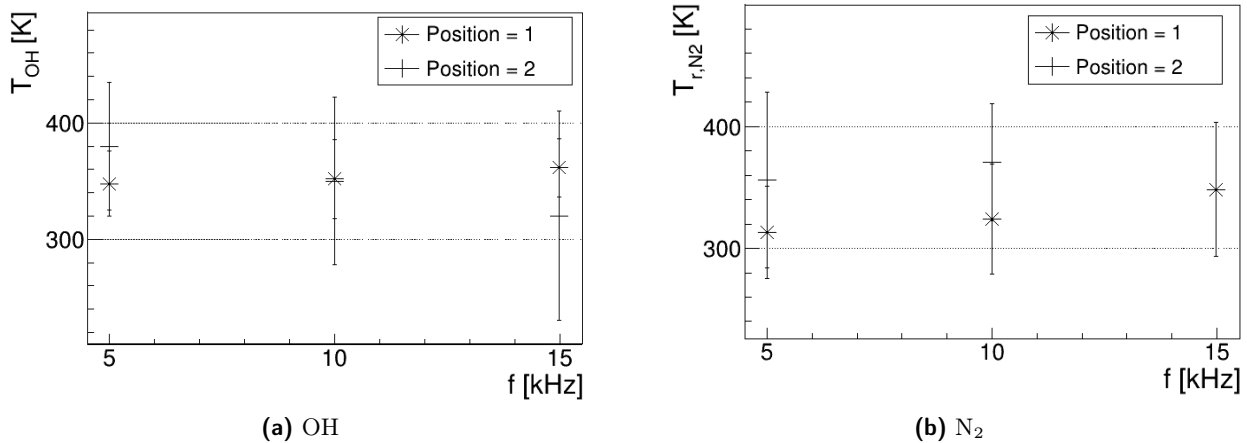


Figure 4.10: Estimation of rotational temperature of OH and N₂ molecules, for different parameters setup and positions.

From estimated temperatures we can see that they are compatible with each other, for every distance and for every pulse setup. It's then possible to evaluate a mean value for the species, that are $T_{r,\text{OH}} = 352 \pm 38 \text{ K}$ and $T_{r,\text{N}_2} = 321 \pm 41 \text{ K}$, compatible with each other, and that, as said before, can be taken as an indicator of kinetic temperature for neutral species, so as temperature of the fluid. Those temperatures are a little higher than room temperature, but they are compatible with the definition of cold plasma.

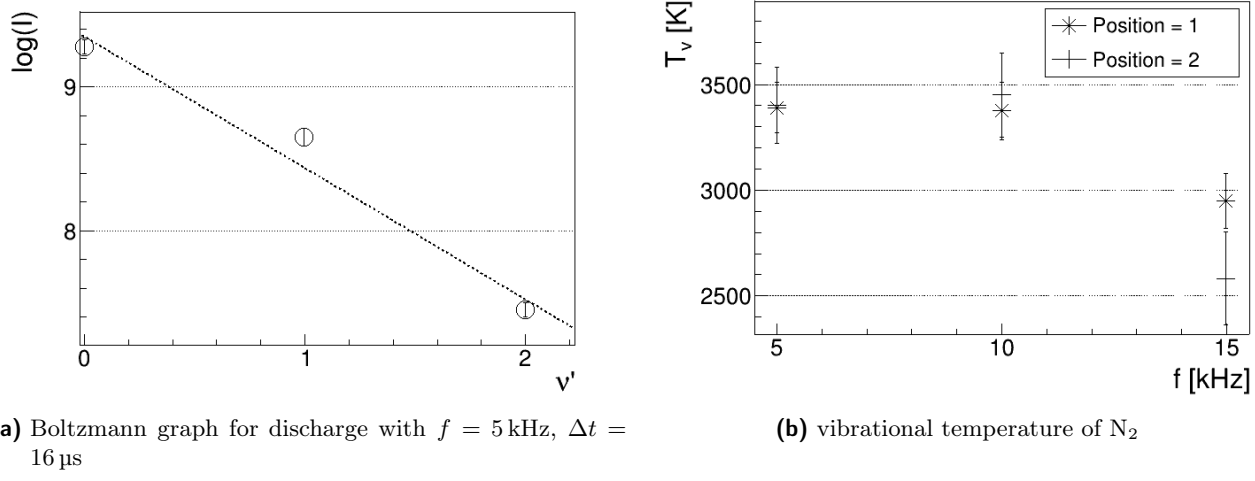
4.4.2 Vibrational temperature for N₂

Given a set of vibrational transition lines with defined $\Delta\nu = \nu' - \nu''$, their relative intensities are correlated to each other, with a proportionality that involves vibrational temperature ([70]). With peak intensities estimated for a given transition, we can make the Boltzmann graph as in figure ?? and evaluate T_v as in formula 4.4.

$$\log(I(\nu')) = S\nu'' + I_0$$

$$T_v[K] = \frac{10^4}{3.57 \cdot S - 0.03} \quad (4.4)$$

Results are in figure 4.11. For this parameter we have values compatible with each other at low and medium power pulse settings with a mean value of $T_v = 3405 \pm 154$ K, while we find a lower temperature for high power pulse settings $T_v = 2781 \pm 322$ K. It seems that with an higher pulse repetition rate we have lower concentration of excited N₂, produced with lower energy.



(a) Boltzmann graph for discharge with $f = 5$ kHz, $\Delta t = 16\ \mu\text{s}$

(b) vibrational temperature of N_2

Figure 4.11: Example of boltzmann graph for estimation of vibrational temperature (a), for discharge with $f = 5$ kHz, $\Delta t = 16\ \mu\text{s}$, lens in position 1 and vibrational temperatures of N_2 molecule (b), for different pulse parameters settings, emission measured from position 1 and 2.

Chapter 5

Temperature profile

Direct application of plasma leads to deposition of accelerated particles on application target, increasing it's temperature. For non thermal blood coagulation it's fundamental that on biological tissues this temperature increase must be below dangerous limits.

If we hypotize that the main heating mechanism of our source is by convection, we can estimate heat transfer rate, i.e. power, due to plasma application on a target and have an estimation of the temperature increase when applied on a biological tissue (for a review of their thermal characteristics see [74]). The main problem with this approach is that we exclude possible heat effects due to current induced in the target, however it gives a rough estimation of plasma power dependencies from application parameters such as pulse repetition rate or distance between source and target.

5.1 Experimental setup

Plasma heat power is measured estimating how much temperature increases with the application of plasma on a target with known heat capacity. The use of a thermocamera allows to study target's temperature profile in its entirety, visualizing also heat conduction on target's borders. An object at thermal equilibrium in a temperature range around 300 K emits radiation in the long-wavelength infrared region (from 8 to 15 μm). This radiation can be collected and it's intensity measured by a bolometer, evaluating the temperature of the object from it's infrared emission, as in common thermal cameras ([75]). The detector more used is an uncooled microbolometer VOx with an array of pixels as in figure ???. Incident radiation strikes a material that has an absorption peak in infrared wavelength, temperature increases changing the electrical resistance of the circuit and the resulting current intensity is measured and associated to collected radiation intensity.

Camera We utilize a termographic camera *FLIR A655sc* ([76]) with a spectral range of 7.5 – 14 μm , resolution 640×480 and detector pitch 17 μm , equipped with a lens with focal 41.3 mm (field of view

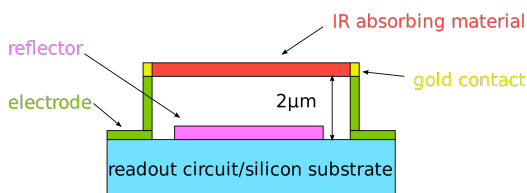


Figure 5.1: Representation of pixel in a microbolometer detector. When incident radiation arrives on the pixel, temperature increases and electric resistance of the circuit changes, giving rise to a current intensity proportional to radiation intensity.

15°). Temperature evolution is a phenomenon with characteristic time of several seconds, we have a reasonable resolution with frame rate acquisition set at 2 FPS.

The temperature conversion between intensity of the radiation and temperature is done by *FLIR* software, setting the appropriate emissivity.

Source We use the latest source model, B in chapter 2, at different pulse repetition frequencies f and voltage peak values V_p . Plasma formation and deposition it's not a continuous phenomenon, it happens in correspondence of voltage pulses, with a characteristic time around $1\ \mu\text{s}$, see chapter 3. Given a time interval, f defines the number of pulses that arrives in that interval.

The gas we use to produce plasma is helium, with flow of 2 L/min.

Target We use an aluminium target, disk shaped, with radius 7 mm and height 1 mm, on a plastic support with width 5 mm. Aluminium has specific heat capacity $c_p = 897\ \text{J/kgK}$ and density $\rho = 2700\ \text{kg/m}^3$, corresponding to target heat capacity $C = 0.373 \pm 0.005\ \text{J/K}$.

Target is positioned at a distance of 210 mm from camera lens. At those conditions, once the image is in focus, pixel to pixel distance on acquired frames is $86.4\ \mu\text{m}$.

We want to study proportionality with distance between target and source, so the target is positioned at a distance of 5.5, 7.5 or 9.5 mm from the end of the source head.

Measurements procedure Ultimately measurements are done with different voltage pulse repetition frequencies f , voltage peak values V_p and distances between target and source d . Once those parameters are set, we follow an approximative timeline:

- acquisition of at least 4 frames for background evaluation in 2 s
- start of gas flow for a minimum of 5 s
- start of the discharge for a minimum of 30 s
- stop of the discharge and acquisition with only gas flow for 5 s
- stop of gas flow

Start and end time for those phases can be observed directly from measures.

5.2 Temperature profile

Every frame gives information on the temperature of every pixel of acquired image at a given time, as in figure 5.2. We are interested in temperature difference, to find them we evaluate background temperature before discharge as the average value acquired before gas opening and subtract it to pixel value in other frames. In a given direction we obtain a graph as in figure 5.2.

Source is pointed to target center, for frames acquired with the discharge we see clearly where the temperature rises and estimate center position. We find the point with maximum temperature and select a square window interesting for temperature evaluation centered on it, with edge 15 mm where it's possible to see the entirety of the target. We find the center position, compatible in each measurements set, at coordinates $x_c = 25.06 \pm 0.20\ \text{mm}$, $y_c = 21.17 \pm 0.20\ \text{mm}$.

It's interesting to note that when there is only gas flowing on the target, temperature increases radially from the center, in an area larger than the target area, while when there is plasma, temperature increases rapidly in an area compatible with the target dimensions. It's possible that gas before

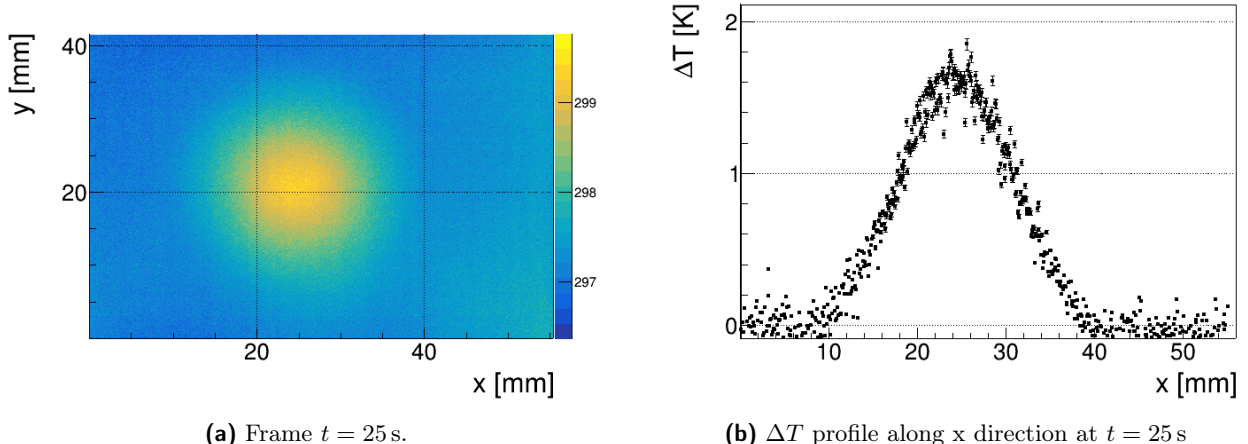


Figure 5.2: Example of measurement during discharge with parameters $f = 5\text{ kHz}$, $V_p = 7.2\text{ kV}$ and $d = 5.5\text{ mm}$.

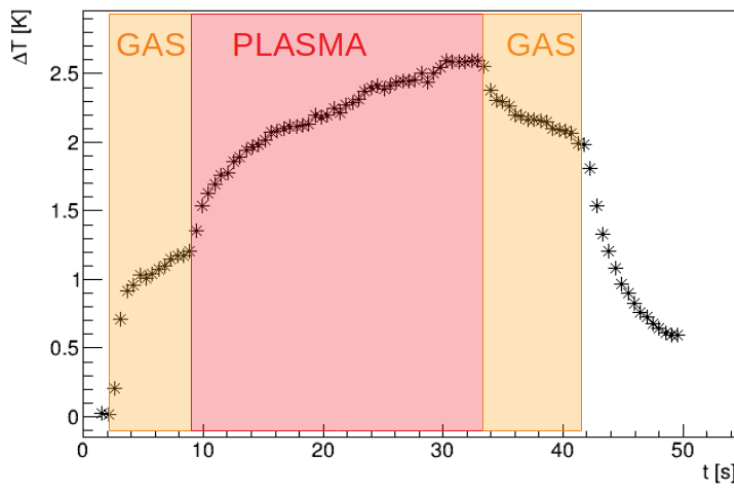


Figure 5.3: Average increase in temperature for every frame at different times, on a square around the target. There are three phases highlighted: gas phase before source activation, plasma phase and gas phase after source power off.

ionization creates a gas layer with a radius larger than the target radius, but if we observe temperature increase only around the target it doesn't give problems in heat power evaluation due to discharge.

From each of those frames we evaluate the average temperature difference and its evolution, as shown in figure 5.3. This graph allows to extrapolate time intervals for gas flow and discharge: where temperature changes rapidly we have gas opening, source activation, discharge end and gas flow stop. In figure 5.4 an example of how temperature profile changes during discharge.

5.3 Power estimation

During the plasma phase, temperature increase in target can be defined as the sum of power deposition plus thermalization contributions (see [77]), as in equation 5.1, where m is the mass of the portion of target considered, c_p is aluminium specific heat capacity, P is power deposited by plasma on target, T_0 is a temperature limit and k a constant parameter dependant from the target.

$$mc_p \frac{dT}{dt} = P - k(T - T_{\lim}) \quad (5.1)$$

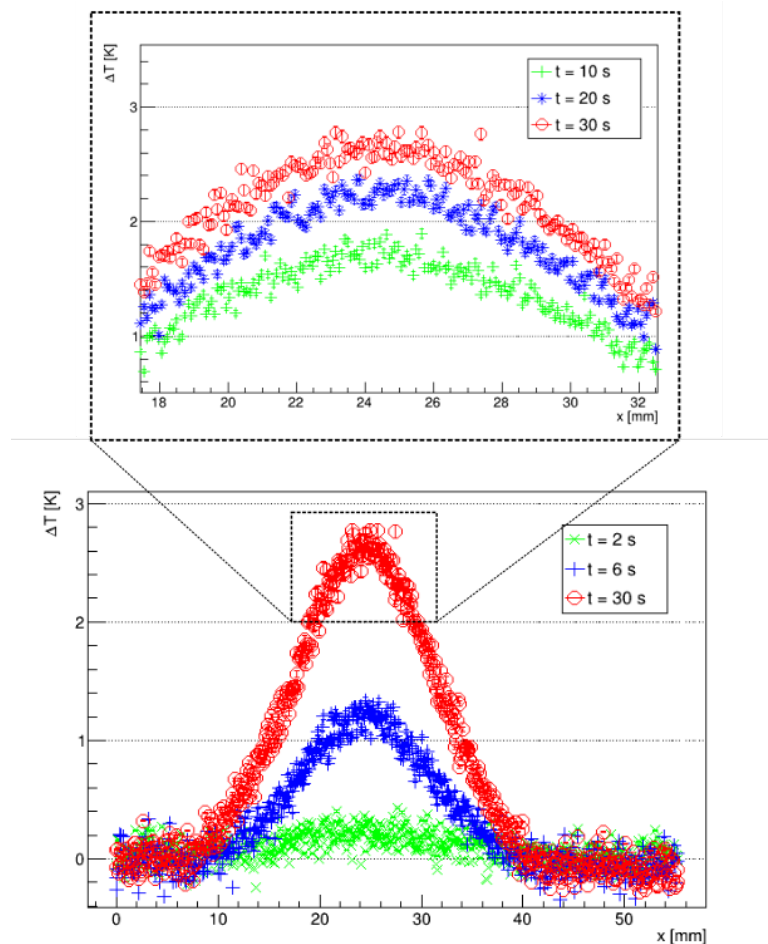


Figure 5.4: Evolution of temperature profile in x direction, with a zoom on the region around the target, for different times and phases: $t = 2$ s before gas opening, $t = 6$ s after gas opening and before discharge, $t = 10, 20, 30$ s during discharge.

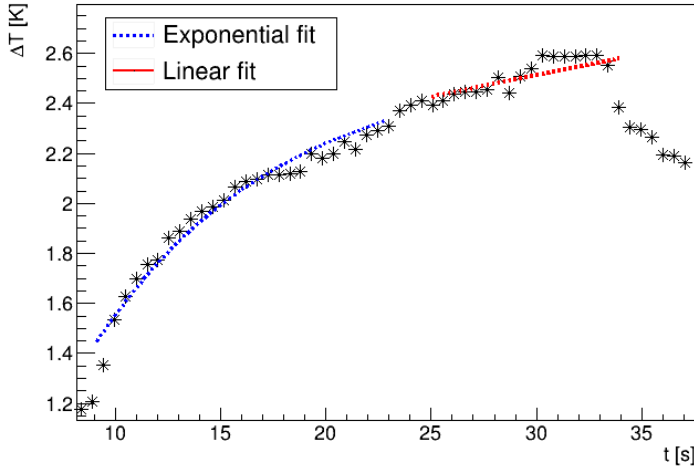


Figure 5.5: Average increase of temperature. The exponential fit shows the analytical solution for equation 5.1, the linear fit is how power is extrapolated.

The analytical result of this equation is an exponential function, as in figure 5.5 for the center pixel in the image. The downside of the exponential fit it's that isn't possible to evaluate the contribution of power deposition from it. If we consider temperature variation only for temperatures close to T_0 , where the thermalization contribute is neglectable, we can extrapolate parameter P with a linear fit. The power parameter that we evaluate this way it's not a precise value because there are also thermalization contributes, but we can use it to study the behavior varying other parameters.

To assure that we are observing temperature variation only inside the target, we consider every pixel in a radius of 7 mm from the center of plasma application. The mean temperature variation in those conditions follows equation 5.2, where ρ is aluminium density, h is target width, A_p is target area, T_{avg} is the average temperature of a pixel, T_p is the temperature of a pixel.

$$mc_p T_{\text{avg}}(t) = \rho h A_p \frac{\sum_{\text{pixels}} T_p}{N_{\text{pixels}}} = Pt + T_0 \quad (5.2)$$

Plasma deposition isn't continuous in time but it happens within time intervals, as we can see in chapter 3. Power evaluated considering the total time interval of plasma application is an effective power P_{eff} that doesn't take into consideration the real time interval of interaction between plasma and target, a fraction of the total one. We can estimate the power associated with a single pulse P_{pulse} , considering the time interval for the interaction of every pulse Δt_{pulse} multiplied by the rate of pulses during the discharge f , as in equation 5.3. An appropriate time pulse duration is $\Delta t_{\text{pulse}} = 1 \mu\text{s}$, as in chapter 3.

$$P_{\text{pulse}} = \frac{P_{\text{eff}}}{\Delta t_{\text{pulse}} f} \quad (5.3)$$

Pulse rate dependency We extrapolate power parameter with different pulse repetition rate, voltage peak value set at $V_p = 7.2 \text{ kV}$ and distance between source and target $d = 5.5 \text{ mm}$. In figure 5.6 there are effective power during the discharge and the pulse power relative to a single pulse. As expected the effective power is proportional to frequency of pulses: greater frequency means more pulses in a given time. It's instead interesting to note that power for a single pulse decreases with increasing pulse rate. An explanation could be that for different pulse repetition rate the time interval relative to the single pulse, i.e. the time interval during which we see plasma bullets, decreases from $\Delta t_{\text{pulse}} = 1 \mu\text{s}$ for $f = 5 \text{ kHz}$ to values around $\Delta t_{\text{pulse}} = 500 \text{ ns}$ for $f = 25 \text{ kHz}$. This result could imply that for higher frequencies we have bullets more rapid.

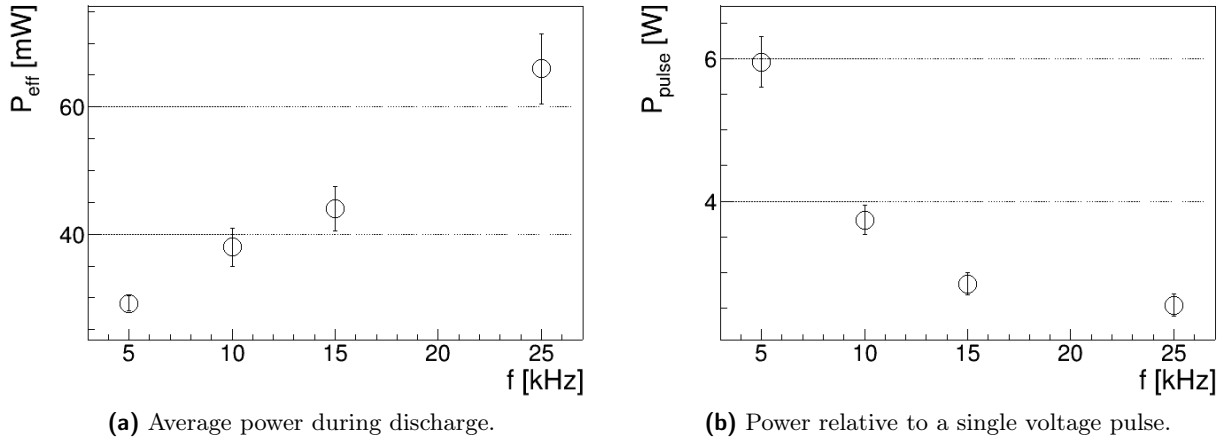


Figure 5.6: Plasma power deposition on target for different pulse repetition rates.

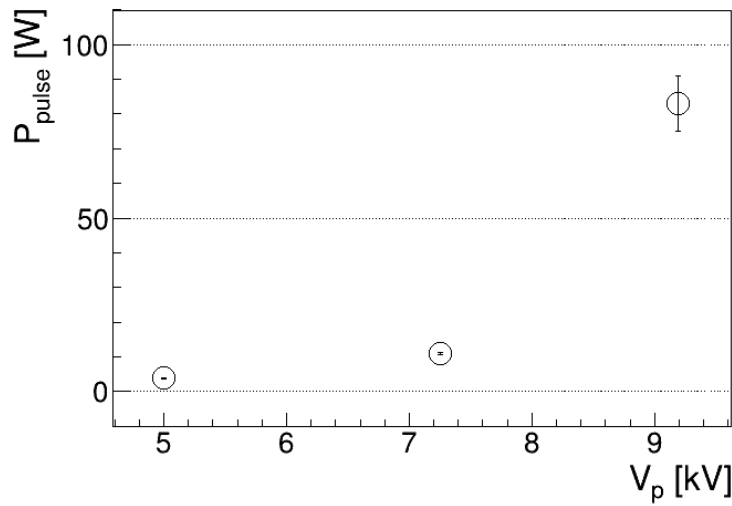


Figure 5.7: Plasma power of a single pulse for different voltage peak values.

Voltage peak value dependency We measure how temperature increases with distance between source and target $d = 5.5$ mm and pulse repetition rate $f = 5$ kHz, for different voltage values. In figure 5.7 we can see that power for the single pulse is correlated with the voltage peak value and increases rapidly when voltage increases. This behavior is expected because with an higher peak voltage value there is more electrical power transferred from the source and we have higher bullet velocity, as seen in chapter 3.

Distance dependency We measure influence of the distance between target and source, setting voltage peak at $V_p = 7.2$ kV and $f = 5$ kHz. In figure 5.8 we can see how power decreases with increasing distance, as expected because for higher distances between source and target, bullets lose more energy before the impact and will transfer less energy to the target. For distance going from 5.5 mm to 7.5 mm we can find a pulse power loss rate of 0.28 ± 0.05 W/mm.

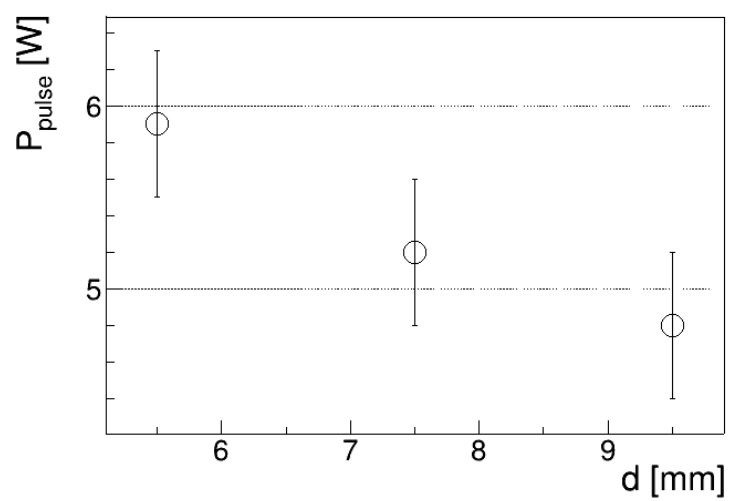


Figure 5.8: Plasma power of a single pulse for different target distances.

Bibliography

- [1] M G. Kong et al. “Plasma medicine: An introductory review”. In: *New Journal of Physics* 11 (Nov. 2009). DOI: 10.1088/1367-2630/11/11/115012.
- [2] Gianluca De Masi et al. “Plasma Coagulation Controller: A Low- Power Atmospheric Plasma Source for Accelerated Blood Coagulation”. In: *Plasma Medicine* 8.3 (2018), pp. 245–254. ISSN: 1947-5764.
- [3] Victor J. Thannickal and Barry L. Fanburg. “Reactive oxygen species in cell signaling”. In: *American Journal of Physiology-Lung Cellular and Molecular Physiology* 279.6 (2000), pp. L1005–L1028. DOI: 10.1152/ajplung.2000.279.6.L1005.
- [4] Ursula Rauen et al. “Nitric oxide increases toxicity of hydrogen peroxide against rat liver endothelial cells and hepatocytes by inhibition of hydrogen peroxide degradation”. In: *American Journal of Physiology-Cell Physiology* 292.4 (2007), pp. C1440–C1449. DOI: 10.1152/ajpcell.00366.2006.
- [5] E Martines et al. “A novel plasma source for sterilization of living tissues”. In: *New Journal of Physics* 11.11 (2009). DOI: 10.1088/1367-2630/11/11/115014.
- [6] E Stoffels et al. “Mass spectrometric detection of short-living radicals produced by a plasma needle”. In: *Plasma Sources Science and Technology* 16.3 (2007). DOI: 10.1088/0963-0252/16/3/014.
- [7] Gregory Fridman et al. “Blood Coagulation and Living Tissue Sterilization by Floating-Electrode Dielectric Barrier Discharge in Air”. In: *Plasma Chemistry and Plasma Processing* 26.4 (2006), pp. 425–442. DOI: 10.1007/s11090-006-9024-4.
- [8] Beate Haertel et al. “Non-Thermal Atmospheric-Pressure Plasma Possible Application in Wound Healing”. In: *Biomolecules & Therapeutics* 22.6 (2014). DOI: 10.4062/biomolther.2014.105.
- [9] Dayun Yan, Jonathan H. Sherman, and Michael Keidar. “Cold atmospheric plasma, a novel promising anti-cancer treatment modality”. In: *Oncotarget* 8.9 (2016). DOI: 10.18632/oncotarget.13304.
- [10] M. Laroussi. “Nonthermal decontamination of biological media by atmospheric-pressure plasmas: review, analysis, and prospects”. In: *IEEE Transactions on Plasma Science* 30.4 (2002), pp. 1409–1415. DOI: 10.1109/TPS.2002.804220.
- [11] X. Deng, J. Shi, and M. G. Kong. “Physical Mechanisms of Inactivation of *Bacillus subtilis* Spores Using Cold Atmospheric Plasmas”. In: *IEEE Transactions on Plasma Science* 34.4 (2006), pp. 1310–1316. DOI: 10.1109/TPS.2006.877739.
- [12] S. U. Kalghatgi et al. “Mechanism of Blood Coagulation by Nonthermal Atmospheric Pressure Dielectric Barrier Discharge Plasma”. In: *IEEE Transactions on Plasma Science* 35.5 (2007), pp. 1559–1566. DOI: 10.1109/TPS.2007.905953.
- [13] A. Von Engel and J.R. Cozens. “Flame Plasmas”. In: ed. by L. Marton. Vol. 20. Advances in Electronics and Electron Physics. Academic Press, 1965, pp. 99 –146. DOI: [https://doi.org/10.1016/S0065-2539\(08\)60495-3](https://doi.org/10.1016/S0065-2539(08)60495-3).
- [14] M. Goossens. *An Introduction to Plasma Astrophysics and Magnetohydrodynamics*. Astrophysics and Space Science Library. Springer Netherlands, 2012. ISBN: 9789400710764.

- [15] X M Zhu et al. "Measurement of the electron density in atmospheric-pressure low-temperature argon discharges by line-ratio method of optical emission spectroscopy". In: *Journal of Physics D: Applied Physics* 42.14 (2009). DOI: 10.1088/0022-3727/42/14/142003.
- [16] R Ohyama, M Sakamoto, and A Nagai. "Axial plasma density propagation of barrier discharge non-thermal plasma bullets in an atmospheric pressure argon gas stream". In: *Journal of Physics D: Applied Physics* 42.10 (2009), p. 105203. DOI: 10.1088/0022-3727/42/10/105203.
- [17] J Amorim, M A Ridenti, and V Guerra. "Experimental and theoretical study of atmospheric-pressure argon microplasma jets". In: *Plasma Physics and Controlled Fusion* 57.7 (2015), p. 074001. DOI: 10.1088/0741-3335/57/7/074001.
- [18] Thomas J. Bruno W. M. Haynes David R. Lide. *CRC handbook of chemistry and physics: a ready-reference book of chemical and physical data*. 99th edition. CRC Press. ISBN: 978-1-4987-5429-3, 1498754295.
- [19] L. Bárdos and H. Baránková. "Cold atmospheric plasma: Sources, processes, and applications". In: *Thin Solid Films* 518.23 (2010). ISSN: 0040-6090. DOI: <https://doi.org/10.1016/j.tsf.2010.07.044>.
- [20] Gregory Fridman et al. "Applied Plasma Medicine". In: *Plasma Processes and Polymers* 5.6 (). DOI: 10.1002/ppap.200700154.
- [21] Ulrich Kogelschatz. "Dielectric-Barrier Discharges: Their History, Discharge Physics, and Industrial Applications". In: *Plasma Chemistry and Plasma Processing* 23.1 (2003). DOI: 10.1023/A:1022470901385.
- [22] By E. V. Shun'ko. URL: <https://commons.wikimedia.org/w/index.php?curid=27512503>.
- [23] Ya. Z. Slutsker et al. "Electrical model of cold atmospheric plasma gun". In: *Physics of Plasmas* 24.10 (2017), p. 103510. DOI: 10.1063/1.4986023.
- [24] Tao Shao et al. "Electrical characterization of dielectric barrier discharge driven by repetitive nanosecond pulses in atmospheric air". In: *Journal of Electrostatics* 67.2 (2009), pp. 215 –221.
- [25] E Stoffels et al. "Plasma needle for medical treatment: recent developments and perspectives". In: *Plasma Sources Science and Technology* 15.4 (2006), S169–S180. DOI: 10.1088/0963-0252/15/4/s03.
- [26] M. Laroussi and X. Lu. "Room-temperature atmospheric pressure plasma plume for biomedical applications". In: *Applied Physics Letters* 87.11 (2005), p. 113902. DOI: 10.1063/1.2045549.
- [27] XinPei Lu and Mounir Laroussi. "Dynamics of an Atmospheric Pressure Plasma Plume Generated by Submicrosecond Voltage Pulses". In: 2016.
- [28] Cecilia Piferi. "Caratterizzazione di sorgenti di plasma per applicazioni mediche". 2016/17.
- [29] *Coils core datasheet*. URL: https://www.mouser.it/datasheet/2/400/e_32_16_9-1527777.pdf.
- [30] J. Upadhyay et al. "Development of high-voltage pulse generator with variable amplitude and duration". In: *Review of Scientific Instruments* 85.6 (2014), p. 064704. DOI: 10.1063/1.4884883.
- [31] Julien Jarrige, Mounir Laroussi, and Erdinc Karakas. "Formation and dynamics of plasma bullets in a non-thermal plasma jet: influence of the high-voltage parameters on the plume characteristics". In: *Plasma Sources Science and Technology* 19.6 (2010), p. 065005. DOI: 10.1088/0963-0252/19/6/065005. URL: <https://doi.org/10.1088%2F0963-0252%2F19%2F6%2F065005>.
- [32] T Darny et al. "Analysis of conductive target influence in plasma jet experiments through helium metastable and electric field measurements". In: *Plasma Sources Science and Technology* 26.4 (2017), p. 045008. DOI: 10.1088/1361-6595/aa5b15. URL: <https://doi.org/10.1088%2F1361-6595%2Faa5b15>.
- [33] *ROOT documentation for TVirtualFFT class*. URL: <https://root.cern.ch/doc/master/classTVirtualFFT.html>.

- [34] R. Brun. *ROOT documentation for Landau() function*. 1995. URL: <https://root.cern.ch/doc/master/namespacETMath.html#a656690875991a17d35e8a514f37f35d9>.
- [35] U. Kogelschatz, B. Eliasson, and W. Egli. “Dielectric-Barrier Discharges. Principle and Applications”. In: *Journal de Physique IV Colloque 07.C4* (1997), pp. C4–47–C4–66. DOI: 10.1051/jp4:1997405. URL: <https://hal.archives-ouvertes.fr/jpa-00255561>.
- [36] Takaaki Tomai, Tsuyohito Ito, and Kazuo Terashima. “Generation of dielectric barrier discharge in high-pressure N₂ and CO₂ environments up to supercritical conditions”. In: *Thin Solid Films* 506–507 (2006), pp. 409–413. ISSN: 0040-6090. DOI: <https://doi.org/10.1016/j.tsf.2005.08.101>.
- [37] Lewi Tonks and Irving Langmuir. “A General Theory of the Plasma of an Arc”. In: *Phys. Rev.* 34 (6 1929), pp. 876–922. DOI: 10.1103/PhysRev.34.876. URL: <https://link.aps.org/doi/10.1103/PhysRev.34.876>.
- [38] M.A. Lieberman and A.J. Lichtenberg. *Principles of Plasma Discharges and Materials Processing*. Wiley, 1994. ISBN: 9780471005773. URL: <https://books.google.it/books?id=-cloQgAACAAJ>.
- [39] Stephanie Tümmel et al. “Low Temperature Plasma Treatment of Living Human Cells”. In: *Plasma Processes and Polymers* 4.S1 (2007), S465–S469. DOI: 10.1002/ppap.200731208. eprint: <https://onlinelibrary.wiley.com/doi/pdf/10.1002/ppap.200731208>. URL: <https://onlinelibrary.wiley.com/doi/abs/10.1002/ppap.200731208>.
- [40] N Mericam-Bourdet et al. “Experimental investigations of plasma bullets”. In: *Journal of Physics D: Applied Physics* 42.5 (2009), p. 055207. DOI: 10.1088/0022-3727/42/5/055207. URL: <https://doi.org/10.1088%2F0022-3727%2F42%2F5%2F055207>.
- [41] Eric Robert et al. “Experimental Study of a Compact Nanosecond Plasma Gun”. In: *Plasma Processes and Polymers* 6.12 (2009), pp. 795–802. DOI: 10.1002/ppap.200900078.
- [42] Wen Yan and Demetre J. Economou. “Simulation of a non-equilibrium helium plasma bullet emerging into oxygen at high pressure (250–760Torr) and interacting with a substrate”. In: *Journal of Applied Physics* 120.12 (2016), p. 123304. DOI: 10.1063/1.4963115.
- [43] D Breden, K Miki, and L L Raja. “Self-consistent two-dimensional modeling of cold atmospheric-pressure plasma jets/bullets”. In: *Plasma Sources Science and Technology* 21.3 (2012), p. 034011. DOI: 10.1088/0963-0252/21/3/034011. URL: <https://doi.org/10.1088%2F0963-0252%2F21%2F3%2F034011>.
- [44] Seth A. Norberg, Eric Johnsen, and Mark J. Kushner. “Helium atmospheric pressure plasma jets touching dielectric and metal surfaces”. In: *Journal of Applied Physics* 118.1 (2015), p. 013301. DOI: 10.1063/1.4923345.
- [45] URL: <https://www.ptgrey.com/Content/Images/uploaded/Flea.pdf>.
- [46] URL: <http://netpbm.sourceforge.net/doc/pgm.html>.
- [47] Julien Jarrige, Mounir Laroussi, and Erdinc Karakas. “Formation and dynamics of plasma bullets in a non-thermal plasma jet: influence of the high-voltage parameters on the plume characteristics”. In: *Plasma Sources Science and Technology* 19.6 (2010), p. 065005. DOI: 10.1088/0963-0252/19/6/065005. URL: <https://doi.org/10.1088%2F0963-0252%2F19%2F6%2F065005>.
- [48] R. Brun. *ROOT documentation for TH2 class*. URL: <https://root.cern.ch/doc/master/classTH2.html>.
- [49] ashok kumar Singh and Beer Bhaduria. “Finite Difference Formulae for Unequal Sub-Intervals Using Lagrange’s Interpolation Formula”. In: *Journal of Math. Analysis* 3 (Jan. 2009), pp. 815–827.
- [50] Dong Jun Jin, Han S. Uhm, and Guangsup Cho. “Influence of the gas-flow Reynolds number on a plasma column in a glass tube”. In: *Physics of Plasmas* 20.8 (2013), p. 083513. DOI: 10.1063/1.4819246. URL: <https://doi.org/10.1063/1.4819246>.

- [51] G J M Hagelaar and L C Pitchford. “Solving the Boltzmann equation to obtain electron transport coefficients and rate coefficients for fluid models”. In: *Plasma Sources Science and Technology* 14.4 (2005), pp. 722–733. DOI: 10.1088/0963-0252/14/4/011.
- [52] Various databases, retrieved on March 14, 2019. URL: <https://www.lxcat.net>.
- [53] Francis F. Chen. *Introduction to Plasma Physics and Controlled Fusion*. 2nd. 1984.
- [54] Yuri P. Raizer. *Gas Discharge Physics*. 1991. DOI: 10.1007/978-3-642-61247-3.
- [55] A S Dickinson, Malsoon Seo Lee, and L A Viehland. “The mobility of He ions in helium gas”. In: *Journal of Physics B: Atomic, Molecular and Optical Physics* 32.20 (1999), pp. 4919–4930. DOI: 10.1088/0953-4075/32/20/309.
- [56] H R Skullerud and P H Larsen. “Mobility and diffusion of atomic helium and neon ions in their parent gases”. In: 23.6 (1990), pp. 1017–1041. DOI: 10.1088/0953-4075/23/6/010.
- [57] Nisha Chandwani et al. “Determination of Rotational, Vibrational and Electron Temperatures in Dielectric Barrier Discharge in air at atmospheric pressure”. In: (June 2014). DOI: 10.13140/RG.2.1.2078.6725.
- [58] Ioana Gerber et al. “Air Dielectric Barrier Discharge Plasma Source For In Vitro Cancer Studies”. In: *Clinical Plasma Medicine* 9 (Feb. 2018), p. 4. DOI: 10.1016/j.cpme.2017.12.006.
- [59] S. P. Kuo et al. “Applications of Air Plasma for Wound Bleeding Control and Healing”. In: *IEEE Transactions on Plasma Science* 40.4 (2012), pp. 1117–1123. ISSN: 0093-3813. DOI: 10.1109/TPS.2012.2184142.
- [60] Hans-Joachim Kunze (auth.) *Introduction to Plasma Spectroscopy*. 1st ed. Springer Series on Atomic, Optical, and Plasma Physics 56. Springer-Verlag Berlin Heidelberg, 2009. ISBN: 9783642022326,3642022326.
- [61] Gerhard Herzberg. *Molecular Spectra and Molecular Structure I: Spectra of Diatomic Molecules*. 2nd. D. Van Nostrand, 1950. ISBN: 9780442033859,0442033850.
- [62] Wikipedia contributors. *Vibronic spectroscopy*. 2018. URL: https://en.wikipedia.org/w/index.php?title=Vibronic_spectroscopy&oldid=823782704.
- [63] I A Kossyi et al. “Kinetic scheme of the non-equilibrium discharge in nitrogen-oxygen mixtures”. In: *Plasma Sources Science and Technology* 1.3 (1992), pp. 207–220. DOI: 10.1088/0963-0252/1/3/011. URL: <https://doi.org/10.1088/0963-0252/2F1%2F3%2F011>.
- [64] LIAM E. GUMLEY. *Practical IDL Programming*. San Francisco: Morgan Kaufmann, 2002. ISBN: 978-1-55860-700-2. DOI: <https://doi.org/10.1016/B978-155860700-2.50003-3>.
- [65] M. Miroslav. *ROOT documentation for TSpectrum class*. URL: <https://root.cern.ch/doc/v614/classTSpectrum.html>.
- [66] Andre Knie. “Photon induced inner-shell excitation processes of nitrous oxide probed by angle resolved fluorescence and Auger-Electron spectrometry”. Dr. Kassel: Univ. Kassel, 2013. ISBN: 978-3862194582.
- [67] H.A. Van Sprang, H.H. Brongersma, and F.J. De Heer. “Absolute emission cross sections for the calibration of optical detection systems in the 120–250 nm range”. In: *Chemical Physics Letters* 65.1 (1979), pp. 55–60. ISSN: 0009-2614. DOI: [https://doi.org/10.1016/0009-2614\(79\)80124-4](https://doi.org/10.1016/0009-2614(79)80124-4). URL: <http://www.sciencedirect.com/science/article/pii/0009261479801244>.
- [68] C. de IZARRA. “COMPUTER SIMULATION OF THE UV OH BAND SPECTRUM”. In: *International Journal of Modern Physics C* 11.05 (2000), pp. 987–998. DOI: 10.1142/S0129183100000857. eprint: <https://doi.org/10.1142/S0129183100000857>. URL: <https://doi.org/10.1142/S0129183100000857>.
- [69] S. B. Bayram and M. V. Freamat. “Vibrational spectra of N₂: An advanced undergraduate laboratory in atomic and molecular spectroscopy”. In: *American Journal of Physics* 80.8 (2012), pp. 664–669. DOI: 10.1119/1.4722793. eprint: <https://doi.org/10.1119/1.4722793>. URL: <https://doi.org/10.1119/1.4722793>.

- [70] N Britun et al. “Determination of the vibrational, rotational and electron temperatures in N₂and Ar–N₂rf discharge”. In: *Journal of Physics D: Applied Physics* 40.4 (2007), pp. 1022–1029. DOI: 10.1088/0022-3727/40/4/016. URL: <https://doi.org/10.1088%2F0022-3727%2F40%2F4%2F016>.
- [71] A. Kramida et al. 2018.
- [72] Se Youn Moon and W. Choe. “A comparative study of rotational temperatures using diatomic OH, O₂ and N₂+ molecular spectra emitted from atmospheric plasmas”. In: *Spectrochimica Acta Part B: Atomic Spectroscopy* 58.2 (2003). INTERSIBGEOCHEM 01, pp. 249 –257. ISSN: 0584-8547. DOI: [https://doi.org/10.1016/S0584-8547\(02\)00259-8](https://doi.org/10.1016/S0584-8547(02)00259-8). URL: <http://www.sciencedirect.com/science/article/pii/S0584854702002598>.
- [73] Charles de Izarra. “UV OH spectrum used as a molecular pyrometer”. In: *Journal of Physics D: Applied Physics* 33.14 (2000), pp. 1697–1704. DOI: 10.1088/0022-3727/33/14/309. URL: <https://doi.org/10.1088%2F0022-3727%2F33%2F14%2F309>.
- [74] Kerstin Giering et al. “Review of Thermal Properties of Biological Tissues”. In: *SPIE-The International Society For Optical Engineering* (1995), pp. 45–65.
- [75] Rikke Gade and Thomas B. Moeslund. “Thermal cameras and applications: a survey”. In: *Machine Vision and Applications* 25.1 (2014), pp. 245–262. ISSN: 1432-1769. DOI: 10.1007/s00138-013-0570-5.
- [76] URL: https://www.flir.com/globalassets/imported-assets/document/rnd_011_us.pdf.
- [77] Antonio Pimazzoni. “Investigation of the parameters of a particle beam by numerical models and diagnostic calorimetry”. 2018.